TWO COMPUTATIONAL NEURAL MODELS: RODENT PERIRHINAL CORTEX AND CRAB CARDIAC GANGLION

A Dissertation

presented to

the Faculty of the Graduate School

University of Missouri – Columbia

In Partial Fulfillment

of the Requirement for the Degree

Doctor of Philosophy

---

by

PRANIT SAMARTH

Dr. Satish S. Nair, Dissertation Supervisor

May 2021

The undersigned, appointed by the dean of the Graduate School, have examined the dissertation entitled

TWO COMPUTATIONAL NEURAL MODELS: RODENT PERIRHINAL CORTEX AND CRAB CARDIAC GANGLION

presented by Pranit Samarth,

a candidate for the degree of doctor of philosophy,

and hereby certify that, in their opinion, it is worthy of acceptance.

Professor Satish S. Nair

Professor Dominic Ho

Professor Michela Becchi

Professor David Schulz

ACKNOWLEDGEMENTS

I want to appreciate my advisor Dr. Satish Nair for his guidance and support. Without him this work would not have been accomplished. I also thank Dr. David Schulz, Dr. Dominic Ho and Dr. Michela Becchi for being a part of my Ph.D. program committee.

I am also grateful to all my current and previous lab members who were always ready to help me in every possible way.

Lastly, I would like to thank my parents for their blessings that have made me the person that I am today as well as my wife Richa for her constant support and encouragement.

TABLE OF CONTENTS

CHAPTER 1

CHAPTER 2

CHAPTER 3

CHAPTER 4

LIST OF FIGURES

Figure **Page**

Chapter 2

Chapter 3

Chapter 4

LIST OF TABLES

Table **Page**

Chapter 2

Chapter 3

Chapter 4

ABSTRACT

Neural engineering research has been rapidly growing in prominence in the past two decades, with ‘reverse engineer the brain’ listed as one of the 14 grand challenges outlined by the National Academy of Engineering. The computational aspect of reverse engineering includes a study of how both single neurons and networks of neurons integrate diverse signals from both the environment and from within the animal and make complex decisions. Since there are many limitations on the experiments that can be performed in alive or isolated biological systems, there is a need of standalone computational models which can help perform ‘in silico’ experiments. This dissertation focuses on such ‘in silico’ neuronal models to predict underlying mechanisms of governing interactions and robustness.

The first model investigated is that of a rodent perirhinal cortex area 36 (PRC), and its role in associative memory formation. A large-scale 520 cell biophysical model of the PRC was developed using biological data from the literature. We then used the model to shed light on the mechanisms that support associative memory in the perirhinal network. These analyses revealed that perirhinal associative plasticity is critically dependent on a specific subset of neurons, termed conjunctive cells. When the model network was trained with spatially distributed but coincident neocortical inputs, these conjunctive cells acquired excitatory responses to the paired neocortical inputs and conveyed them to widely distributed perirhinal sites via longitudinal projections. Ablation of conjunctive cells during recall abolished expression of the associative memory.

The second model focuses on a model for crab cardiac system consisting of five Large Cells (LC) developed using firsthand biological data. The model is then used to study the features of its underlying oscillation in its membrane potential during a rhythm and to reverse engineer the experimentally discovered phenomenon related to network synchrony. The model predicted

multiple mechanisms of compensation to restore network synchrony based on compensatory intrinsic conductances.

Finally, a third model, related to the second one, was of an improved three-compartmental biophysical model of an LC that is morphologically realistic and includes provision for inputs from the SCs. To determine viable LC models, maximal conductances in three compartments of an LC are determined by random sampling from a biologically characterized 9D-parameter space, followed by a three-stage rejection protocol that checks for conformity with features in experimental single cell traces. Random LC models that pass the single cell rejection protocol are then incorporated into a network model followed by a final rejection protocol stage. Using disparate experimental data, the study provides hitherto unknown structure-function insights related to the crustacean cardiac ganglion large cell, including the differential roles of active conductances in the three compartments. The novel morphological architecture for the large cell was validated using biological data and used to make predictions about function. A testable prediction related to function was that active conductances, specifically, the persistent sodium current, is required in the neurite to transmit the spike waveforms from the spike initiation zone to the soma. Another pertains to the co-variation of maximal conductances of the persistent sodium current with that of the leak current.

CHAPTER 1

INTRODUCTION AND OBJECTIVES

1.1. BACKGROUND AND MOTIVATION

As a kid, I had always wondered why babies start crying at birth. Why do they not smile or laugh. As I grew older, I realized that after birth, their brain starts acquiring data from the senses, and from interaction with people and objects. But still I did not get a clear answer to why they cry. When I started my undergraduate studies, I researched this further and found that some tiny area in their tiny brain makes them afraid or fearful of the sudden change in surrounding and probably the discomfort during birth, i.e., automatically they start to fear. After I started my Master's degree, I was introduced to the world of computational neuroscience which has the power to provide answers to formerly difficult questions about the functioning of our brains.

Brain, a complex network of 100 billion neurons in humans, make us who we are. All our perceptions, experiences and senses are controlled by brain. Imagining what will happen if brain did not exist also requires the brain. Neuroscience, a study of the brain, is one of the fastest growing fields in the 21st century. Neuroscientists have been trying to study the brain since early 20th century but have able to understand only a minuscule part of its mysterious workings. One of the main reasons for this slow pace in unraveling brain functions is lack of appropriate advanced technology. A host of new technological tools and techniques [1] are being introduced for finer level probing (e.g., multichannel microrecording arrays [2], brainbow [3], optogenetics [4], DREADD technology [5]) and this has resulted in large amounts of neurophysiological data being generated. With such advanced tools being introduced regularly, the study of the brains is being recognized as an important challenge even for engineers. Indeed, the National Academy of

Engineering has listed ‘reverse engineering the brain’ as one of the 14 grand challenges in engineering (NAS 2008). The time is thus ripe for further involvement by engineers in this area via the development of computational models as yet another ‘tool’ to probe brain functioning.

Computational neuroscience is the study of neurons and how they communicate with each other and control small robust systems as well as big mammalian brains with complex functionality. Neurons are typically individual ‘agents’ that interact with each other in well-defined local and global networks. The functioning of individual neurons as well as their interactions are poorly understood presently. We reverse engineer these nonlinear circuits to understand neuro-computational and system level issues such as bifurcation, adaptation and learning (e.g., long term potentiation/depression), robustness, and control. The biophysical models used incorporate neurophysiological data, including current channels and synapses. We model neuron as a capacitance (cell membrane) and nonlinear resistors (voltage-gated channels). The software package NEURON is used to develop the models. Computational models allow neuroscientists to perform ‘model experiments’ which are presently not possible in in vitro or in vivo settings in the laboratory. For instance, we lack resolution in technology to measure changes at the synaptic levels in vivo, and the measurement problem becomes intractable as the numbers of neurons increases. Reliable computational models also have the potential to save costs, time and animal use.

The process used in a computational neuroscience typically follows three steps: (i) Model development: Creating the model using existing biological data; (ii) Validation of the model: Here the model has to reproduce some biological observations and phenomenon which it was not specifically designed to reproduce; (iii) Predictions from the model: this is the most important part where the model can predict phenomena not yet observed in biology.

1.2 OVERVIEW OF DISSERTATION AND OBJECTIVES

This dissertation deals with three studies investigating neuronal function at both single cell and circuit levels, using biophysical computational models at both levels. All three projects are part of on-going collaborations with neuroscientists who provide both data as well as expertise from the biology side. The core chapters (2-4) are written in the form of journal papers.

Chapter 2. *Mechanisms of memory storage in the perirhinal network: a biophysical modeling study*. The perirhinal cortex supports recognition and associative memory. Prior unit recording studies revealed that recognition memory involves a reduced responsiveness of perirhinal cells to familiar stimuli whereas associative memory formation is linked to increasing perirhinal responses to paired stimuli. Both effects are thought to depend on perirhinal plasticity but it is unclear how the same network could support these two opposite forms of plasticity. However, the Pare Lab (our collaborator) recently showed that when neocortical inputs are repeatedly activated, depression or potentiation could develop, depending on the extent to which the stimulated neocortical activity pattern recruited intrinsic longitudinal perirhinal connections. We developed a biophysically realistic model of perirhinal area 36 that could reproduce the different responses to neocortical stimuli as shown by that study. We then used the model to shed light on the mechanisms that support associative memory in the perirhinal network. These analyses revealed that perirhinal associative plasticity is critically dependent on a specific subset of neurons, termed conjunctive cells. When the model network was trained with spatially distributed but coincident neocortical inputs, these conjunctive cells acquired excitatory responses to the paired neocortical inputs and conveyed them to widely distributed perirhinal sites via longitudinal projections. Ablation of conjunctive cells during recall abolished expression of the associative memory. However, ablation of conjunctive cells during training did not prevent associative memory formation because a new set of conjunctive cells emerged, revealing that competitive synaptic interactions within the perirhinal network governs the formation of conjunctive cell assemblies.

Chapter 3. *Intrinsic and gap junction compensation to preserve single cell and network properties: a computational model study of LC of crab.* The crustacean cardiac ganglion (CG) network coordinates the rhythmic contractions of the heart muscle to control the circulation of blood. The network consists of nine cells, five large motor cells (LCs) and four small endogenous pacemaker cells (SCs). Previous studies have considered homeostatic compensation at either cellular or network levels, but not at both levels for the same preparation. Even with considerable variability in the intrinsic conductance between the five LCs in a cardiac network, they have synchronous output in the intact network. To study why this might be so, we first developed a single cell model for an LC of the crab cancer borealis and then developed a 5-cell network model of its ganglion to study the potential role of co-regulation of intrinsic, and gap junction electrical conductances in restoring LC output as well as the synchronous LC network output. We used the model to predict roles the various intrinsic currents in shaping the output. The model also provides intrinsic correlations that might exist which can be tested in the biological systems. At a network level, the model suggests how intrinsic vs gap junction coupling compensation can help maintain the synchrony in the network. Compensation by increase in the potassium current A was not enough to fully restore the synchrony of the network, but additional compensation by gap junction coupling helped achieve full synchrony.

Chapter 4. *Morphological crustacean cardiac ganglion cell model reveals differential roles of conductances in compartments.* We developed an improved three-compartmental biophysical model of an LC that is morphologically realistic and includes provision for inputs from the SCs. We investigate how the distribution as well as potential covariations of conductances affect membrane potential response. A key prediction from this work was demonstrating the role of active conductances in neurite and predicting their specific functions.

1.3 REFERENCES

1. National Research Council (2008) *From Molecules to Minds: Challenges for the 21st Century: Workshop Summary*. Washington, DC: The National Academies Press.

2. Kelly RC, Smith MA, Samonds JA, Kohn A, Bonds AB, Movshon JA, Lee TS (2007) Comparison of recordings from microelectrode arrays and single electrodes in the visual cortex. J Neurosci 27(2):261–264.

3. Lichtman J, Livet J, Sanes J (2008) A technicolour approach to the connectome. Nat Rev Neurosci 9(6):417-422.

4. Boyden ES, Zhang F, Bamberg E, Nagel G, Deisseroth K (2005) Millisecond-timescale, genetically-targeted optical control of neural activity. Nat Neurosci 8(9):1263–1268.

5. Rogan SC, Roth BL (2011) Remote control of neuronal signaling. Pharmacological Rev 63(2): 291-315

6. NAE (2008) Grand Challenges for Engineering, National Academy of Sciences. Also accessible at http://www.engineeringchallenges.org/8996.aspx

CHAPTER 2

MECHANISMS OF MEMORY STORAGE IN THE PERIRHINAL NETWORK: A BIOPHYSICAL MODELING STUDY

2.1 BACKGROUND

How do we recognize new things and how we associate things?

Consider example of a beautiful flower which has a nice pleasant smell (e.g. Rose) and another flower which is beautiful but has no smell. Our brain associates the pleasant smell with the beautiful flower which makes us remember rose much better. What part of our brain does this?

In mammals, Perirhinal cortex (PRC), a region with 40,000 neurons; is supposed to encode recognition and associative memories.

Our collaborator has done experiments on rodent PRC to show how these memories are stored.

Here we use this data to reverse engineer PRC to understand its working.

Engineering relevance: a) Adaptive learning with potentiation and depression.
b) Architecture for memory storage.
c) Non-linear electrical systems.

2.2 ABSTRACT

The perirhinal cortex supports recognition and associative memory. Prior unit recording studies revealed that recognition memory involves a *reduced* responsiveness of perirhinal cells to familiar stimuli whereas associative memory formation is linked to *increasing* perirhinal responses to paired stimuli. Both effects are thought to depend on perirhinal plasticity but it is unclear how the same network could support these two opposite forms of plasticity. However, a recent study (Unal et al., 2012) showed that when neocortical inputs are repeatedly activated, depression or potentiation could develop, depending on the extent to which the stimulated neocortical activity pattern recruited intrinsic longitudinal perirhinal connections. Here, we

developed a biophysically realistic model of perirhinal area 36 that could reproduce these phenomena. We then used the model to shed light on the mechanisms that support associative memory in the perirhinal network. These analyses revealed that perirhinal associative plasticity is critically dependent on a specific subset of neurons, termed conjunctive cells. When the model network was trained with spatially distributed but coincident neocortical inputs, these conjunctive cells acquired excitatory responses to the paired neocortical inputs and conveyed them to widely distributed perirhinal sites via longitudinal projections. Ablation of conjunctive cells during recall abolished expression of the associative memory. However, ablation of conjunctive cells during training did not prevent associative memory formation because a new set of conjunctive cells emerged, revealing that competitive synaptic interactions within the perirhinal network governs the formation of conjunctive cell assemblies.

2.3 INTRODUCTION

The perirhinal cortex occupies a strategic position among temporal lobe structures involved in declarative memory as it relays a large portion of neocortical sensory inputs to the entorhino-hippocampal system and constitutes the main return path for hippocampo-entorhinal efferents to the neocortex (Deacon et al. 1983; Room and Groenewegen 1986; Witter et al. 1986; Insausti et al. 1987; Suzuki and Amaral 1994ab; Burwell and Amaral 1998ab). In keeping with this, the perirhinal cortex plays a critical role in high-order perceptual and mnemonic functions. Indeed, perirhinal lesions lead to recognition memory impairments (Gaffan and Murray 1992; Meunier et al. 1993, 1996; Zola-Morgan et al. 1989; Suzuki et al. 1993) that compare to, or are more important than, those caused by hippocampal and entorhinal lesions (Aggleton et al.1986; Murray and Mishkin 1986; Meunier et al. 1993; Leonard et al. 1995; Murray et al. 2005). Moreover, perirhinal lesions cause a pronounced associative memory deficit within and across sensory modalities (Murray et al. 1993; Higuchi and Miyashita 1996; Buckley and Gaffan 1998; Parker and Gaffan 1998; Goulet and Murray 2001).

What are the perirhinal correlates of memory formation? With respect to recognition memory, perirhinal neurons display reduced responses to visual stimuli that have been presented previously (Brown et al. 1987; Fahy et al. 1993; Li et al. 1993; Miller et al. 1993; Sobotka and Ringo 1993). These response attenuations develop rapidly (within a single training session), last a long time (>one day), and are far more common among perirhinal than hippocampal neurons (Rolls et al. 1993; Riches et al. 1991; Eichenbaum et al. 1996; Xiang and Brown 1998). In contrast, when monkeys are trained to form associations between two arbitrary visual stimuli, a different behavior emerges. As a result of training, many neurons that were only responsive to one of the stimuli acquire responses the paired stimulus (Messinger et al. 2001; Naya et al. 2003a). Critically, the incidence of such pair coding neurons is much higher in area 36 than in neighboring neocortical regions (Naya et al. 2003a).

On the surface, the familiarity-induced response depressions and the emergence of pair coding behavior seem contradictory because both result from repeated presentations of the same stimuli. However, a recent study in the whole brain in vitro (Unal et al. 2012) revealed how synaptic plasticity in the perirhinal network could support these two phenomena, depending on the extent to which the stimulated neocortical activity pattern recruited intrinsic longitudinal perirhinal connections.

Here, we developed a biophysical model of perirhinal area 36 that could reproduce the findings of this in vitro study. We then challenged the model with various spatiotemporally distributed patterns of neocortical inputs to shed light on the mechanisms that support associative memory in the perirhinal network. Our findings suggest that associative memory formation is dependent on the emergence of a specific subset of conjunctive cells that acquire excitatory responses to coincident neocortical inputs and convey their influence to widely distributed perirhinal sites via longitudinal projections.

2.4 METHODS

Overview

We first summarize the approach used to construct the model and then describe each aspect in detail below. Based on experimental data about the anatomical and physiological properties of the perirhinal cortex, we created a realistic biophysical model of perirhinal area 36. When lacking relevant data to constrain a particular aspect of the model, we relied on findings obtained in different cortical areas. We first built multi-compartment models of individual principal and local-circuit neurons based on previously published studies on the electroresponsive properties of perirhinal cells. Next, principal and local-circuit neurons were distributed in a tri-dimensional space that reproduced the laminar organization of perirhinal area 36. Then, we endowed the model with realistic intrinsic connectivity, including intra- and inter-laminar connections, long-range rostro-caudal links as well as local circuit inhibitory connections, and finally, extrinsic inputs from the associative temporal neocortex. As ubiquitously found in the cerebral cortex, the inhibitory connections present in the model include GABA-A and B receptor-mediated components whereas excitatory synapses are dual glutamatergic AMPA/NMDA synapses. In keeping with the extensive literature on perirhinal synaptic plasticity, excitatory synapses were modeled such that they could undergo activity-dependent plasticity under the control of group I mGlu receptors and NMDA receptors. In the following, we consider the experimental data supporting these properties and explain how they were implemented in the model.

Individual Cell Models

Principal cell model. In the perirhinal cortex, three main types of principal neurons have been identified: regular spiking (RS), burst firing, and late spiking cells (Beggs and Kairiss 1994; Faulkner and Brown 1999; D'Antuono et al. 2001; Martina et al. 2001b; Moyer et al. 2002). The RS cell type is by far prevalent, except in layer VI where late spiking neurons are more common (Faulkner and Brown 1999; McGann et al. 2001). However, pilot simulations revealed that random synaptic activity in our model network depolarized late firing cells enough to inactivate the slow A-like current that underlies the late-firing behavior (Storm 1988), effectively transforming them into RS neurons. Consequently, to accelerate the simulations, we only included principal cells of the RS variety.

The RS cell model has 5 compartments respectively representing the soma (includes axon), basal dendrites, apical trunk, from which emerge two apical dendrites. The dimensions of these compartments (**Table 1**) were selected to preserve biological realism and match passive properties (**Table 2, Fig. 1A1**; Bush et al. 1993; Moyer et al. 2002). The ionic currents inserted into each compartment were adapted from existing biophysical models of hippocampal and entorhinal neurons (Migliore et al. 1995, 1999; Dickson et al. 2000; Fransen et al. 2002, 2004, 2006; Migliore 2003; Hemond et al. 2008). The ionic currents included in each compartment and their associated parameters are listed in **Table 1**.

Interneuron models. Based on earlier studies in the cerebral cortex (Gupta et al. 2000; Kawaguchi and Kondo 2002; Klausberger and Somogyi 2008), perirhinal area 36 likely contains a wide variety of inhibitory local-circuit cells. However, since there is limited data about their connectivity and electroresponsive properties (Beggs and Kairiss 1994; Faulkner and Brown 1999; Martina et al. 2001ab), we modeled the two types of interneurons that are prevalent in all cortical regions: the fast-spiking subtype of parvalbumin-expressing (PV) and somatostatin-expressing (SOM) interneurons, that together account for ~70% of cortical interneurons (Rudy et al. 2011). For both types of local-circuit cells, we developed three-compartmental models and endowed them with passive properties and voltage-gated-currents (**Table 1**) so that they could reproduce the electroresponsive properties described in prior experimental studies **(Fig. 1A2,A3;** Faulkner and Brown 1999; D'Antuono et al. 2001; Martina et al. 2001b; Moyer et al. 2002; Ma et al. 2006).

Connectivity of the model

The perirhinal network model consists of 400 RS, 60 PV and 60 SOM cells distributed in a two-dimensional space with dimensions of 10 and 3 mm for the rostrocaudal and transverse axes, respectively. PV and SOM interneurons were placed at regular intervals along the rostrocaudal axis to ensure uniform inhibition throughout the network. RS cells were also distributed uniformly to make their placement symmetrical with respect to interneurons.

Perirhinal area 36 receives around half of its cortical inputs from a laterally adjacent strip of neocortex termed the ‘‘ventral temporal associative neocortex’’ (Burwell et al.1995; Burwell2000; Furtak et al.2007). Most of these neocortical inputs end at perirhinal sites rostrocaudally adjacent to their point of origin; only a minority of neocortical axons reach rostrocaudally distant perirhinal sites (Unal et al.2012). In contrast, the principal perirhinal neurons targeted by neocortical inputs, while also forming local (≤ 1.5 mm; hereafter termed short-range) connections, contribute a prominent system of long-range intrinsic connections that spans the entire rostrocaudal extent of the perirhinal cortex (Witter et al.1986; Burwell and Amaral1998a; Biella et al.2001,2002; Unal et al.2012). Long-range neocortical and perirhinal axons only form glutamatergic synapses, prevalently with principal perirhinal neurons (Unal et al.2013). Also, short vs long-range axons form differential connections with local-circuit cells: the incidence of excitatory synapses onto local-circuit cells is ~ 2–3 times lower in long- than short-range connections (Unal et al.2013). Our perirhinal network model was structured to capture these various properties, as detailed below

Neocortical inputs. Neocortical afferents were modeled with 201 neocortical input cells distributed along the rostrocaudal extent of the perirhinal network. Each neocortical input formed unique connections with perirhinal neurons and could be activated independently. Note that these ‘‘input cells’’ are in fact just spike trains used for synaptic drive. To constrain the distribution of neocortical inputs to the model, we relied on data from previous physiological studies. In particular, patch recordings of perirhinal cells in horizontal slices kept in vitro have revealed that neocortically evoked EPSPs decrease in amplitude as the rostrocaudal distance between the neocortical stimulation site and the recorded cell increases (Martina et al.2001b). Furthermore, this reduction occurs at different distances from the stimulated neocortical site in RS (3 mm) and PV (1 mm) neurons. Thus, model neocortical connections were structured to reproduce these features. To ensure uniform neocortical activation of PV interneurons despite the low cell density compared to real cortex, neocortical connections were made to all PV interneurons within 1.0 mm of the neocortical source in the rostrocaudal axis. Neocortical axons did not contact more distant PV cells, in keeping with prior electrophysiological findings (Martina et al.2001b).

Short- and long-range horizontal connections. As mentioned above, a distinguishing property of the perirhinal cortex is the existence of a prominent system of intrinsic longitudinal connections that spans much of its rostrocaudal extent (Witter et al. 1986; Burwell and Amaral 1998a; Biella et al. 2001, 2002). Although these longitudinal axons arise from and terminate in all layers, cells contributing these intrinsic axons are most concentrated in layers II, V, and VI and they terminate most heavily in superficial layers (Witter et al. 1986; Biella et al. 2001). In the model, these properties were implemented as follows. Long-range connections were made from RS cells to other RS cells located >1.5 mm from the source cell in the rostrocaudal dimension. Long-range connections were not designed to be reciprocal. That is, they were made along the random path of each source cell's single axon. Each source cell formed 21 such connections along the path of its axon and each target RS cell received ≤20 such long-range inputs. This resulted in an RS-RS connection probability of approximately 7%. An RS cell also made long-range connections to SOM cells with a 5% connection probability if the latter was connected to a RS cell that received a long-range connection from the same source RS cell. For short-range connections between RS cells, a connection was made with 8% probability if the rostrocaudal distance between the cells was less than 1 mm.

Local circuit inhibitory connections. Lacking perirhinal data to constrain the connections between RS and PV cells, we adjusted these connections so as to reproduce the dramatic impact of feedforward and feedback inhibition on the responsiveness of perirhinal RS cells, as documented in previous electrophysiological studies (Biella et al. 2001; Martina et al. 2001b). In particular, excitatory connections to PV interneurons and inhibitory connections to RS cells were made with 100% probability within a radius of 0.75 mm, which ensured that all RS cells were within the inhibitory field of at least one interneuron. SOM cells inhibited all the RS cells within a rostrocaudal distance of 0.75 mm, as well as the PV cells within a rostrocaudal distance of 0.25 mm. SOM cells did not receive inputs from nearby cells, RS or PV.

In keeping with prior anatomical and electrophysiological observations (Fino et al. 2012; Adesnik et al. 2012; Pfeffer et al. 2013; Zhang et al. 2014), the two types of interneurons targeted different compartments of RS cells (PV, soma; SOM, dendrites), they formed contrasting connections with each other (SOM cells inhibited PV cells but not the opposite), and they were differentially innervated by long-range cortical inputs (SOM received such inputs; not PV cells).

Synaptic currents, short- and long-term synaptic plasticity

Synaptic currents. As is the case throughout the cerebral cortex, including perirhinal area 36 (Ziakopoulos et al. 2000; Martina et al. 2001a), inhibitory connections present in the model include GABA-A and B receptor-mediated components whereas excitatory synapses are dual glutamatergic AMPA/NMDA synapses. All synapses are assigned maximal and initial conductances (G_{AMPA}, G_{NMDA}, G_{GABAa}, G_{GABAb}). These values were uniform within each synapse type. AMPA currents were further modified by a plastic weight $W_{\mathrm{i,j}}$, as justified below. As is customary in the modeling literature (Dyhrfjeld-Johnsen et al. 2007), we compensated for the reduction in network size by increasing synaptic strengths. Conductance values and related details are in section S.3 of supplementary materials.

Short-term synaptic plasticity. Because short-term synaptic depression is ubiquitous between principal cortical neurons, model RS to RS synapses were designed to reproduce this property, based on prior experimental data (Silberber et al. 2004). We also modeled short-term facilitation at SOM to RS synapses, as seen in the visual cortex (Ma et al. 2012). See section S.4 of supplementary materials for how short-term synaptic plasticity was implemented in the model.

Long-term synaptic plasticity. Glutamatergic synapses to principal perirhinal cells can undergo long-term activity-dependent changes in efficacy (McCaffery et al. 1999; Ziakopoulos et al. 1999; Cho et al. 2000, 2001; Massey et al. 2001; Cho and Bashir 2002; Cho et al. 2002; Massey et al. 2004; Barker et al. 2006ab; Jo et al. 2008; Massey et al. 2008; Bang and Brown 2009). In contrast, to the best of our knowledge, there has been no report of long-term activity dependent plasticity at connections formed by perirhinal inhibitory neurons. Accordingly, model glutamatergic (but not GABAergic) synapses were endowed with mechanisms allowing long-term activity-dependent plasticity.

It was assumed that activity-dependent changes at inputs to RS cells are expressed postsynaptically, by increases or decreases in AMPA receptor-dependent currents. Based on earlier experimental evidence (Bilkey 1996; Ziakopoulos et al. 1999; Cho et al. 2000, 2001; Jo et al. 2008), these changes in AMPA currents were determined by the competing influence group I metabotropic glutamate receptors (mGluRs) and NMDA receptors. In particular, activation of mGluRs induced long-term depression (LTD) whereas moderate vs. strong activation of NMDA receptors induced LTD or long-term potentiation (LTP), respectively. This was implemented as follows. At each excitatory synapse, the AMPA current amplitude was modified by $W_{i,j}$, the plastic weight of the synapse between cell *i* to cell *j*. The initial weights of all the synapses are listed in table S.3 of supplementary materials. An increase or decrease in $W_{i,j}$ from the initial value represented potentiation or depression of the synapse. Two Ca^{2+}-dependent mechanisms determined the fate of synaptic weights. Accordingly, two separate Ca^{2+} sources were modeled for each synapse: one pool was supplied by NMDA receptors, and a second by Ca^{2+} release from intracellular stores, under the control of mGluRs. See section S.3 of supplementary materials for details.

Model experiments

To test the validity of the model, we examined whether it could reproduce the findings of Unal et al. (2012). Thus, we used the same stimulation paradigms as in this prior study. In all model experiments, the training protocol consisted of a testing phase (“pre-test”), a training phase (“training”), and a second testing phase after training (“post-test”). During both testing phases, the neocortex was stimulated in the same manner: once at a series of rostrocaudal locations, from 0–10 mm, activating 17 neighboring neocortical input neurons at each location (one ‘site’). Three seconds was allowed between the activation of different neocortical sites. Each simulation was repeated five times from different random seeds and the results averaged. During training, various stimulating paradigms were tested. They will be described in detail in the corresponding results sub-sections. However, one of these stimulation patterns is used in several simulations and provided here. To induce activity-dependent plasticity, neocortical inputs from one or more rostrocaudal levels were activated in the following manner: thirty 1-s trains repeated at 8 Hz, each followed by a 0.5-s gap. Below, this stimulation pattern will be termed “theta-frequency stimulation” (TFS). For each modeling experiment, we ran the model five or six times from different random seeds and the data was averaged. Data are expressed as averages ± SEM. All results are expressed as average ± SEM. Unless otherwise stated, we used paired *t* tests for statistical comparisons. However, before using this test, we verified that the data to be compared were normally distributed using a Kolmogorov–Smirnov test.

2.5 RESULTS

This study investigates the mechanisms of distributed synaptic plasticity underlying associative memory formation in the perirhinal cortex. To this end, guided by previous experimental studies, we developed a model of the perirhinal network that captures salient properties of this cortical region. We first provide a general description of the model’s features. Then, to test the model’s validity, we examine whether it can reproduce the findings of a prior study on activity-dependent plasticity in the perirhinal cortex (Unal et al. 2012). Finally, we use the model probe mechanisms of associative memory formation in the perirhinal network.

Model overview

The following summarizes the general properties of the model. The reader is referred to the Methods section and appendices for details regarding the implementation of these properties and for references to the experimental reports used to constrain the model. To minimize computation times while capturing the essence of the perirhinal network (**Fig. 1**), the number of perirhinal cells was reduced to 400 principal (glutamatergic, RS) and 120 local-circuit GABAergic neurons (60 PV and 60 SOM; **Fig. 1B**). Their passive properties as well as the density and distribution of voltage-dependent ionic conductances were adjusted to reproduce the electroresponsive properties of these cells (**Fig. 1A1-3**), as described experimentally. In keeping with prior experimental reports, model PV and SOM cells target different compartments of RS cells (soma and dendrites, respectively), they form contrasting connections with each other (SOM cells inhibit PV cells but not the opposite), and they are differentially innervated by long-range cortical inputs (SOM but not PV cells receive such inputs **Fig. 1B-C**). The model features topographically organized glutamatergic inputs from associative temporal cortical areas, modeled with 201 input cells distributed along the rostrocaudal extent of the perirhinal network (**Fig.1B**). Note that these ‘‘input cells’’ are in fact just spike trains used for synaptic drive. The model also featured a prominent system of intrinsic longitudinal connections with realistic conduction delays. These long-range connections arise exclusively from principal neurons, they span the entire rostrocaudal extent of the network, and they end on other principal and SOM cells, but not PV neurons. The model also features short-term synaptic dynamics (e.g. synapses between RS cells exhibit short-term depression) and activity-dependent synaptic plasticity (activation of group 1 mGluRs induces LTD; activation of NMDA receptors induces LTD or LTP depending on the level of postsynaptic depolarization). Last, LTD and LTP are expressed postsynaptically, by changes in the AMPA conductance of individual synapses.

Response of model neurons to neocortical inputs

Figure 2 shows the response of the model neurons to single neocortical stimuli delivered at the same rostrocaudal level as the recorded cells vs a longitudinally distant site. Responses are shown in two ways: at rest with the full complement of voltage-gated currents (left) or at three different membrane potentials (right). For the latter, the fast Na+ conductance of the target cells was set to zero, so the responses could be examined without contamination from spikes and afterhyperpolarizations.

Single stimuli applied at a nearby neocortical site elicited EPSPs that triggered spikes in 45 ± 8% of RS cells (**Fig. 2A**, RS). Whether or not a spike was elicited, these EPSPs were rapidly curtailed by a biphasic IPSP (**Fig. 2C**, RS) that was comprised of an early phase reversing at around –70 mV (GABA-A) and a longer-lasting component with a more negative reversal potential (GABA-B). These inhibitory potentials are due to the supra-threshold activation of many (50 ± 14%) nearby PV cells (**Fig. 2A**, PV) by excitatory inputs from RS cells and neocortical input neurons. In contrast, SOM interneurons were never fired by nearby neocortical stimuli (**Fig. 2A**, SOM). Instead, they exhibited long-latency EPSPs (**Fig. 2C**, SOM) due to the activation of rostrocaudally-distant RS cells that contributed horizontal axons back to them.

The responses elicited by rostrocaudally distant neocortical stimuli (**Fig. 2B**) differed drastically from those elicited by nearby stimuli (**Fig. 2A**). First, RS cells rarely fired in response to distant neocortical stimuli. Second, because the long-range horizontal axons of RS cells do not contact PV neurons, rostrocaudally distant RS cells displayed little or no inhibition (**Fig. 2B,D**, RS).

Yet, PV cells displayed long-latency IPSPs due to the activation of SOM cells by longitudinal inputs (**Fig. 2B,D**, PV). An additional difference between the impact of nearby vs. distant neocortical stimuli resided in the response of SOM cells. Whereas these cells exhibited sub-threshold EPSPs in response to nearby stimuli (**Fig. 2A,C**, SOM), they were strongly activated by distant stimuli (**Fig. 2B,D**, SOM), 47 ± 17% of them generating orthodromic action potentials. This phenomenon resulted from their innervation by the long-range horizontal axons of RS cells.

Dependence of perirhinal plasticity on the spatial distribution of neocortical inputs

To test the model's validity, we next examined whether it could reproduce the findings of a study on activity-dependent plasticity in perirhinal area 36 of the whole guinea pig brain kept *in vitro* (Unal et al. 2012). This study examined the activity evoked by temporal neocortical inputs using optical measurements with voltage sensitive dyes and multiple simultaneous field potential recordings along the rostrocaudal extent of the perirhinal cortex. After obtaining control response amplitudes from each neocortical stimulation site, TFS was applied at one or two distant neocortical sites. Unal et al. (2012) reported that TFS at one neocortical site produced a LTD of optical and field potential responses evoked from the induction site but not from control (unstimulated) sites. In contrast, they observed that TFS simultaneously applied at two distant neocortical stimulation sites produced a LTP of perirhinal responses evoked from the induction, but not the control (unstimulated) sites. Although the changes in perirhinal responsiveness induced by TFS at one or two neocortical stimulation sites were selective to the induction sites, the changes could be seen throughout the rostrocaudal axis of the perirhinal cortex.

We first simulated TFS application at a single neocortical stimulation site using the perirhinal network model. Such a simulation is shown in **Fig.3A** where TFS was applied at neocortical site

5 (red). Before reporting the results of this simulation, we explain the approach used to construct **Fig.3** as the same procedure will be used to illustrate the results of other simulations. The three histograms in **Fig.3A1** plot the number of RS cells firing in response to single neocortical stimuli applied at site 1(left), site 5 (middle), or site 9 (right). A different color(red) is used for the site 5 histogram because this site will receive TFS in subsequent panels. The x-axis of the three histograms shown in **Fig.3A1** corresponds to the rostro-caudal or antero-posterior (AP) axis of the model. By comparing the distribution of activated cells in the three graphs, one can see that the AP level with the most activated cells is always at proximity of the neocortical stimulation site; as the neocortical stimulation site shifts caudally (from the left-most to the right-most histogram), the AP level with the most RS cells firing also shifts caudally. Note that these three histograms depict the control responsiveness of the model prior to single-site TFS at site 5. The same three histograms are shown with a compressed x-axis below in **Fig.3A2** (oblique lines), along with histograms illustrating the model's responses to other neocortical stimulation sites. **Figure3A2** thus shows the control responsiveness of the model prior to single-site TFS at site 5. **Figure3A3** is organized exactly as **Fig.3A2** but it shows the responsiveness of the model after single-site TFS at site 5. **Figure3A4** simply shows the difference between panels 3a3 and 3a4. Here, negative values mean that fewer RS cells respond after than before single-site TFS at site 5 and thus, that TFS caused a response depression

As seen experimentally (Unal et al. 2012), when we simulated TFS application at a single neocortical stimulation site, we observed that single-site TFS at site 5 caused a marked depression of RS responses evoked from the induction site (**Fig.3A4**; -39±4 % RS cells spiking; paired *t* test, $p<0.0011$; below, unless otherwise noted, we used paired t tests for all statistical comparisons). Further paralleling experimental observations, this depression was restricted to RS cells located at proximity of the stimulation site. Responses to the other stimulation sites remained unchanged (2±1 %; p=0.31).

In contrast with single-site TFS, simultaneous delivery of TFS at two distant neocortical sites (**Fig.3B**) produced a potentiation of responses evoked from those sites (32±3 % RS cells spiking; p=0.0002), as reported in Unal et al. (2012). Further paralleling experimental findings, the potentiation was seen at all rostrocaudal levels of the model network and was most pronounced for responses elicited from the paired sites; other sites showed only marginal changes (6±1%; p=0.23). In the Unal et al. (2012) study, it was further observed that delaying the stimulation of one of the two paired sites by half a theta cycle during TFS (or 65 ms) abolished the potentiation of responses elicited by the paired neocortical inputs. We simulated this experiment and obtained the same result (**Suppl. Figure 2**).

The Unal et al. (2012) study also reported on the impact of several other manipulations such as inactivating long-range connections during two-site TFS as well as the effect of NMDA or group I mGluR antagonists on the activity-dependent plasticity induced by one- or two-site TFS. The model could reproduce the consequences of these various manipulations, as described in **Supplementary Fig. 3–4.**

Unal et al. (2012) offered the following interpretation for their findings. It is entirely consistent with the phenomena observed in our model. With respect to perirhinal cells in transverse register with the stimulation site, neo-cortical inputs activate perirhinal PV interneurons, thus limiting the depolarization of principal cells by neocortical afferents. In these conditions, activation of group I mGluRs causes a response depression. In contrast, when these inputs coincide with the activation of a longitudinally distant group of neocortical neurons, responses are shifted toward excitation because long-range longitudinal pathways do not engage PV interneurons. By removing the Mg^{2+} block of NMDA receptors, this stronger depolarization leads to the induction of NMDA-dependent LTP.

Aspects of the model that are critical to reproduce the findings of Unal et al. (2012)

When we developed the current model, we started with single compartment cell models using the Hodgkin-Huxley formulation for currents and matched their passive properties to prior experimental reports. When using these single compartment cell models in a network, the restriction of locating excitatory and inhibitory inputs on the same compartment turned out to be problematic. When trying to match the model's behavior to the single- and paired-site TBS cases of Unal et al. (2012) with the same synaptic parameters, network interactions led to runaway excitation. It became apparent that this problem could be alleviated by spatially segregating excitatory and inhibitory inputs, as occurs in the real network. We reasoned that locating inhibitory synapses on somata and excitatory ones on dendrites would result in a relatively more potent inhibition and help control excitation. Implementing these features required the use of multi-compartmental RS cell models. With such multi-compartmental cell models and spatially segregated excitatory and inhibitory synapses, we were able to match the single-site and paired-site results from Unal et al. (2012), but still could not guarantee stability in all cases. Also, reproducing the effects of group I receptor antagonists seen in Unal et al. (2012) remained impossible as it caused runaway excitation. We explored various ways to solve this problem and ultimately found that the most parsimonious approach was to add another type of inhibitory interneuron, this one dendrite-targeting (SOM cells), as present in the real network. This solved the problem of runaway excitation and ensured good qualitative, but not quantitative, matches to all the results in Unal et al. (2012). Adding inhibition from SOM to PV cells, as occurs in the real network (Pfeffer et al.2013), helped overcome this problem, and provided both qualitative and quantitative matches with all the observations in Unal et al. (2012).

Specific perirhinal cells are critical for associative learning: conjunctive cells

By comparing the responses of RS cells to different neocortical inputs before vs. after TFS, we noticed that two-site TFS led to the emergence of RS cells that fired in response to independent stimulation of the two paired neocortical inputs. Because no RS cells exhibited this property prior to two-site TFS, we reasoned that these neurons might be more critical than others for the induction and expression of the associative plasticity induced by two-site TFS. These cells, hereafter termed conjunctive cells were of two types. Roughly half were located at the perirhinal levels adjacent to the paired neocortical stimulation sites (range: 14 to 20 per site; **Fig. 4A**, red circles) and therefore received direct inputs from one of the two paired sites. The rest (off-site conjunctive cells; range 30 to 44) were not located at perirhinal levels adjacent to the stimulated sites and thus did not receive direct inputs from the paired neocortical sites (**Fig. 4A**, black circles).

Impact of ablating conjunctive cells

To test whether conjunctive cells are more critical than others RS neurons for the associative plasticity induced by two-site TFS, we compared the effect of ablating conjunctive cells or an equal number of randomly selected RS cells during two-site TFS only (training phase), or after conditioning (testing phase). These tests were performed separately for at-site vs. off-site conjunctive cells.

Figure 4B-D contrasts the effects of ablating control RS cells (top, black) or conjunctive cells (bottom, red) during testing (**Fig. 4B,C**) or training (**Fig. 4D,E**) on the number of RS cells firing in response to stimulation of neocortical stimulation sites 2 and 8 after conditioning. Ablation of off-site or at-site conjunctive cells during testing (**Fig. 4B,C**) produced a significant reduction in the potentiation of responses elicited from the paired sites compared to that seen after removal of control cells at corresponding locations (paired t-tests: at-site $p < 0.0001$; off-site, $p = 0.0008$). Similarly, ablating at-site conjunctive cells during training (**Fig. 4D**) produced a significant reduction in the potentiation of responses produced by pairing relative to that seen after removal of at-site control cells (paired t-test, $p = 0.0009$). In contrast, ablating off-site conjunctive cells during training had little effect (paired t-test, $p = 0.17$; **Fig. 4D**). Further analyses revealed that this negative finding resulted from the fact that following ablation of off-site conjunctive cells, a new set of conjunctive cells emerged. For instance, in the particular simulation shown in **Fig. 4E2**, 33 cells that were not conjunctive in the control case developed responses to both of the paired sites when training occurred after ablation of the original 40 off-site conjunctive cells. This phenomenon suggests that a form of synaptic competition (Kim et al. 2013) takes place between off-site RS cells.

Connectivity of conjunctive cells

To shed light on the properties that determined the emergence of conjunctive cells, we compared their inputs and outputs. Overall, relative to other RS cells, there were no significant differences in the number of neocortical inputs they received, in the number of short- or long range input or output connections they formed with other RS cells or in their connections with PV or SOM interneurons. This was true for both at-site and off-site conjunctive cells. When we restricted the comparisons to neocortical inputs recruited by the pairing paradigm, we found that at-site conjunctive cells and control RS cells received a similar number of these inputs. Together, these negative findings indicate that there were no *a priori* differences in the connectivity of conjunctive cells. Rather, these results suggest that conjunctive cells emerge out of the specific network interactions that unfold when two groups of neocortical inputs neurons are repeatedly activated during paired-site TFS.

In support of this contention, dramatic differences in the connectivity of conjunctive cells emerged when we examined their intrinsic connections with other RS cells that fired during pairing (**Table 3**). Indeed, relative to control cells, at-site and of-site conjunctive cells received significantly more short- and long-range inputs from RS cells that fired during two-site TFS (for both: $p<0.0001$; unpaired t-tests). Moreover, they contributed significantly more short- and long-range projections to RS cells that fired during two-site TFS (long range: $p<0.0001$; short range: $p=0.0004$; unpaired t-tests).

Reactivation of conjunctive cells

Overall, the above analyses suggest that conjunctive cells play a critical role in the acquisition and expression of associative plasticity. Conceiving associative plasticity as a proxy for associative memory, we next asked: are conjunctive cells also involved in the recall of associative memories? In the real network, cells at different rostrocaudal levels of the perirhinal cortex receive different types of sensory information (Room and Groenewegen 1986). Thus, when two sensory inputs are associated in the perirhinal cortex, an optimal storage strategy would be to selectively enhance the responsiveness of RS cells receiving the paired inputs and/or the connections between them. However, this is not the behavior Unal et al. (2012) observed experimentally or seen in our simulations: the increase in perirhinal responsiveness produced by paired-site TFS is not limited to cells receiving the paired inputs. It is observed throughout the perirhinal cortex (see **Fig. 3B**, red).

Thus, when assessing how well (that is, with how much specificity) a ‘‘memory’’ is reactivated, it is important to take into consideration the type of RS cells responding to the reactivating stimulus. Accordingly, below we distinguish between RS cells that acquired new spiking responses to one ‘‘plastic cells’’ or both ‘‘conjunctive cells’’ of the paired neocortical inputs. Also, we will refer to cells that did not acquire new spiking responses as ‘‘non-plastic’’ cells. Finally, the qualifiers ‘‘at-site’’ or ‘‘off-site’’ will be used for the three terms to indicate whether the cells had access to neocortical inputs from one of the two paired sites during training.

Table4 lists the relative incidence of at-site and off-site CCs, plastic cells, and non-plastic cells as seen across ten separate runs. Examination of this data reveals that there are nearly as many at-site and off-site cells whose responsive-ness to the paired stimuli increases after two-site TFS. On the surface, the diffuse distribution of cells responsive to the paired inputs seems incompatible with selective memory recall: how could an associative memory be retrieved with some measure of selectivity if independent activation of one of the two paired representations recruited so many cells that normally process other inputs. This paradox led us to con-sider the possibility that at-site or off-site CCs might have unique connections that could promote a more selective reactivation of network, or in other words, that they serve as memory retrieval cells. Here, it should be noted that reactivated at-site plastic cells and CCs, embody the ‘‘signal’’, and that off-site non-plastic cells, are considered ‘‘noise’’.

To test this possibility, after two-site TFS, we simultaneously ‘‘reactivated’’ off-site or at site CCs (**Fig.5A1, B1**) and compared the impact of these manipulations to that obtained when stimulating an equal number of randomly picked plastic (**Fig.5A2, B2**) or non-plastic cells

(**Fig.5A3, B3**) at the same location. In these simulations (n=10 foreach of the 6 cases), random uncorrelated synaptic inputs were injected in all RS cells so that they would fire at an average of ~0.6 Hz, as seen in vivo (Collins et al.1999). On this background, two spikes were elicited in all cells of interest by applying a brief intracellular current pulse (50 ms, 0.18 nA; random onset delay of 1–10 ms; **Fig.5C1**) and monitoring the responses elicited in target cells (**Fig.5C2–5**). This stimulus can be conceived of as roughly approximating the impact of extrinsic cortical inputs involved in memory retrieval.

Chi square tests revealed a significant dependence in the number of reactivated plastic and CCs at-site and the identity of the stimulated cells (CCs, plastic cells, or control cells) whether the latter were off-site (**Fig.5A**; X^2=348.4, p<0.0001) or at-site (**Fig.5B**; X^2=115.8, p<0.0001). Expectedly, current-evoked firing in non-plastic cells (**Fig.5A3, B3**) reactivated very few at-site plastic cells or CCs (B9 % of total) relative to other types of input neurons. Therefore, the following will be restricted to comparisons between the impact of current-evoked firing in plastic cells vs CCs, off-site or at-site.

To assess which of these two cell classes was most selective in reactivating the associative memory, we com-pared the incidence of reactivated at-site plastic cells and CCs, embodying the ‘‘signal’’, and that of off-site non-plastic cells, considered as ‘‘noise’’, depending on the identity of the input cells. Although other off-site cells could be construed as noise (e.g., off-site plastic cells), we will not consider them below because they served as input cells for some of the stimulation and therefore were not available for recruitment.

We found that whether the input cells were at-site or off-site CCs, they recruited more of the signal cells and less of the off-site non-plastic cells than when the input cells were plastic cells. In particular, when the input cells were off-site (**Fig.5A**), current-evoked firing in CCs (**Fig.5A1**) recruited 33.4±5.8 % of at-site CCs and 23.1±4.8 % of at-site plastic cells compared to 23.1±6.1 and14.8±2.9 % of the corresponding cells classes when the input cells were plastic cells (**Fig.5A2**). The difference in the combined incidence of at-site plastic cells and CCs as a function of the identity of the input cells was statistically significant (p=0.025). Even though off-site CCs were more effective in recruiting at-site signal cells, they recruited fewer off-site non-plastic cells (13.3±1.6 %) compared to the case when the input cells were off-site plastic cells (21.1±2.3 %; p=0.0009).

Similarly, when the input cells were at-site (site 2 in **Fig.5B**), current-evoked firing in CCs (**Fig.5B1**) recruited35.0±6.2 % of at-site CCs and 10.1±1.4 % of at-site plastic cells compared to 15.8±3.7 and 6.1±0.6 % of the corresponding cells classes when the input cells were plastic cells (**Fig.5B2**). The difference in the combined incidence of at-site plastic cells and CCs as a function of the identity of the input cells was statistically significant(p=0.0013). As seen when the inputs cells were off-site, even though at-site CCs were more effective in recruiting at-site signal cells, they did not recruit more off-site non-plastic cells (11.3±1.3 %) compared to the case when input cells were at-site plastic cells (12.2±1.6 %; p=0.59). Overall, these results suggest that as a result of paired-site TFS and of the associated activity-dependent plasticity, CCs form a pattern of connections that allows them to preferentially recruit signal cells relative to off-site non-plastic cells. Nevertheless, the pattern of reactivation produced by CCs continued to lack specificity as some of the reactivated cells were not signal neurons.

2.6 DISCUSSION

To shed light on the mechanisms that support associative memory in the perirhinal network, we developed a reduced yet biophysically realistic model of perirhinal area 36. We first assessed the model’s validity by testing whether it could reproduce the findings of a recent study that examined changes in perirhinal responses elicited by activation of neocortical inputs (Unal et al. 2012). The model could reproduce the results of this study, including the observation that repeated activation of focal vs. distributed neocortical inputs alters perirhinal responsiveness in opposing directions (depression vs. potentiation, respectively). We then used the model to examine the mechanisms that support associative plasticity. Our findings suggest that associative memory formation is dependent on a specific subset of perirhinal neurons, termed conjunctive cells, that acquire excitatory responses to coincident neocortical inputs and whose reactivation after learning contributes to memory retrieval.

Relation between activity-dependent plasticity and perirhinal contributions to memory

Depending on stimulation parameters, the perirhinal cortex could exhibit activity-dependent LTP or LTD, as in other cortical regions. For instance, repeated high-frequency (100 Hz) bursts of afferent activity elicit a NMDA-dependent potentiation of perirhinal responses *in vitro* (Bilkey 1996; Ziakopoulos et al. 1999) and *in vivo* (Cousens and Otto 1998). Also, low frequency stimulation produces a Ca^{2+}-dependent LTD or LTP depending on the holding potential during induction (LTD at –70 mV; LTP at –10 mV) (Cho et al. 2001).

The idea emerged that this form of LTD might underlie perirhinal contributions to recognition memory. Indeed, many perirhinal neurons exhibit attenuated responses to previously presented visual stimuli (Brown et al. 1987; Fahy et al. 1993; Li et al. 1993; Miller et al. 1993; Sobotka and Ringo 1993). Supporting the notion that LTD, the familiarity-induced response depression, and perirhinal contributions to recognition memory are functionally related, several studies reported a correlation between the effects of various drugs on recognition memory and LTD induction *in vitro* (Warburton et al. 2003; Wan et al. 2004; Seoane et al. 2009). In contrast, associative memory formation depends on a potentiation of perirhinal responses to paired stimuli. Indeed, when monkeys are trained to associate two visual stimuli, perirhinal neurons that were initially responsive to only one of the two stimuli develop excitatory responses to the paired stimulus (Messinger et al. 2001; Naya et al. 2003a). These findings raise the question of how can repeated stimulus presentations lead the same network to express pair-coding behavior or familiarity-induced response depression?

It was proposed that the solution resides in the differential relation between neocortical vs. perirhinal longitudinal axons with fast-spiking interneurons (Martina et al. 2001b; de Curtis and Pare 2004). Indeed, electrophysiological studies have revealed that when a point source is stimulated in the neocortex, the volley propagates via perirhinal longitudinal axons through the entire rostrocaudal expanse of the perirhinal cortex (Biella et al. 2001, 2010; Martina et al. 2001b; Unal et al. 2012). Importantly, principal perirhinal cells respond differently to neocortical inputs depending on their rostrocaudal position relative to the activated neocortical site, as reproduced by the present model. Cells in transverse register with the stimulation site show mixed excitatory-inhibitory responses, whereas cells distant from the stimulation site lack the inhibitory component (Biella et al. 2001; Martina et al. 2001b). This difference arises because neocortical axons form strong connections with fast-spiking inhibitory interneurons whereas perirhinal longitudinal axons do not (Martina et al. 2001b; Unal et al. 2013).

This organization would explain why repeated activation of neocortical inputs induces opposite forms of plasticity depending on their spatial distribution. For perirhinal cells in transverse register with the neocortical stimulation site, activation of perirhinal inhibitory interneurons limits the depolarization of principal cells by neocortical afferents, favoring LTD. By contrast, when these inputs coincide with the stimulation of a rostrocaudally distant group of neocortical cells, the consequent activation of long-range perirhinal axons shifts the balance toward excitation. This increased depolarization, by removing the Mg^{2+} block of NMDA receptors, then promotes the induction of NMDA-dependent LTP. This explanation found strong support in the findings of Unal et al. (2012) who reported that the polarity and pharmacological dependence of perirhinal plasticity varies depending on the spatial distribution of neocortical inputs. The ability of the current model to reproduce their findings further reinforces this hypothesis.

Synaptic mechanisms of activity-dependent potentiation and depression

The main advantage of biophysical models is that they allow manipulations and measurements that would be experimentally impossible or impractical. For example, in the Unal et al. (2012) study, the identity of the synapses supporting the plasticity induced by single- or paired-site TFS remained unclear. In contrast, we could readily examine the impact of these manipulations on the weight of all model synapses. This analysis revealed that the response depression induced by single-site TFS was mainly due to a decrease in the weight of neocortical inputs to RS cells in transverse register with the neocortical stimulation site. Intrinsic perirhinal connections were barely altered. In contrast, for paired site TFS, both neocortical and intrinsic glutamatergic synapses supported the response potentiation. Interestingly, there was much heterogeneity in the impact of two-site TFS on the weight of neocortical synapses with roughly equal proportions being potentiated or depressed. This contrasted with the weights of short- and long-range glutamatergic connections, most of which were increased or did not change.

A second example of experimentally impossible manipulation allowed by the model are simulations where one retroactively manipulates the properties of specific cells, in this case conjunctive cells. Indeed, we noticed that two-site TFS caused some principal cells to acquire supra-threshold responses to independent stimulation of the two paired neocortical inputs. Using the model, we could go back in time to probe the role of these cells by ablating them during training or testing. During testing, ablation of off-site or at-site conjunctive cells largely reduced the potentiation of responses elicited from the paired sites relative to that seen after removal of control cells. In contrast, during training, ablation of conjunctive cells had little or no effect because a new set of conjunctive cells emerged after ablation, suggesting that a form of synaptic competition (Kim et al. 2013) takes place between RS cells.

Significance of memory retrieval

While the perirhinal system of longitudinal connections allows linkage of spatially distributed input patterns, it also poses a challenge for the specificity of stored representations. In the actual network, cells at different rostrocaudal levels of the perirhinal cortex receive different types of sensory information (Room and Groenewegen1986). However, as seen experimentally (Unal et al.2012) and in the present simulations, repeated paired activation of dis-tant neocortical inputs not only increased the responsive-ness of RS cells receiving the paired inputs but also that of other rostrocaudally distant cells. As a result, subsequent activation of a potentiated neocortical input not only recruits cells receiving the paired inputs, but also other cells that normally process different types of information.

In an attempt to address this conundrum, we considered the possibility that specific types of principal cells might, as a result of associative plasticity, develop patterns of connections that allow a more selective reactivation of associative memories. To this end, we compared the identity of cells reactivated by current-evoked firing in conjunctive, plastic, and control cells. Relative to other cell types, CCs tended to recruit more of the cells primarily responsible for storing associative memories and less of the ones inadvertently linked to the stored representation. Yet, the reactivation patterns were far from specific.

Together, these observations suggest that the perirhinal network is dependent on its targets to increase the specificity of stored representations. A prime candidate for this function is the entorhinal cortex, a major recipient of perirhinal axons (Witter et al.1986; Insausti et al.1987; Suzuki and Amaral1994; Burwell and Amaral1998 a,b).Indeed, considerable experimental and computational evidence supports the notion that increases in the specificity of stored representations could be produced by attractor states within populations of entorhinal neurons for instance (see Akrami et al.2009). Clues as to how entorhinal neurons might fulfill this role come from the dependence of TBS-induced changes in perirhinal responsiveness on rostro-caudal distance from the paired neocortical sites: the increase in responsiveness was more pronounced at perirhinal sites receiving the paired inputs and at immediately adjacent rostrocaudal levels than at more distant sites. Thus, it is possible that the entorhinal network enhances the rostrocaudal differentiation in perirhinal activation patterns. Consistent with this suggestion, prior physiological studies have emphasized that perirhinal-entorhinal interactions are regulated by a powerful inhibitory system, allowing for a selection of relevant inputs (deCurtis and Pare2004). Thus, an important question for future investigations will be to analyze how interactions among the rhinal cortices participate in the formation and recall of associative memories.

2.7 CONCLUSIONS

Our modeling experiments predict that the formation and reactivation of associative memories in the perirhinal cortex are critically dependent on a subset of principal neurons, termed CCs. When associative plasticity is induced, these cells acquire supra-threshold response to independent stimulation of the paired inputs. Although CCs are required for the post-learning reactivation of the activity patterns that subtend associative memories, this property is not due to a priori differences in their connectivity. Rather, our results suggest that CCs emerge from competitive synaptic interactions that unfold during the induction protocol. In keeping with this, pre-learning ablation of CCs do not prevent associative plasticity as the original CCs are replaced by new ones. While the retroactive manipulations we used to demonstrate this will never be possible experimentally, post-learning treatments aiming at selectively reducing or enhancing the activity of CCs are theoretically possible. Such manipulations should respectively interfere with vs enhance associative memory recall. Given recent progress in genetic engineering methods for selectively manipulating specific subtypes of neurons, we are confident that our predictions will soon be tested.

2.8 TABLES

Table 1. Model parameters for RS, PV, and SOM cells.

	RS Cells		**PV Cells**		**SOM Cells**	
	Soma	Apical Trunk/ Apical/ Basal Dendrites	Soma	Dendrites	Soma	Dendrites
Length (µm)	20	400/300/400	10	150	10	150
Diameter (µm)	10	5/3.5/5	10	5	10	5
E_{leak} (mV)	-78	-78	-82.6	-82.6	-67	-67
E_{Na}	55	55	55	55	55	55
E_{K}	-90	-90	-90	-90	-90	-90
E_{H}	-20	--	--	--		
C_{m} (µF)	0.9	0.9	1.2	1.2	1.6	1.6
g_{leak} (S/cm^2)	1.585e-5	1.585e-5	5.7e-5	5.7e-5	5e-5	5e-5
g_{Kd} (S/cm^2)	0.0001	0.00129 0.00131 (for Basal)	0.002	0.002	0.002	0.002
g_{Na} (S/cm^2)	0.8	0.028	0.1	0.05	0.005	0.0042
g_{CaL} (S/cm^2)	0.029	0.0005	--	--	--	--
Additionally, soma had g_{AHP} =0.00028; g_{C}=0.0108; g_{H}=1.1e-5; and g_{A}=0.0001						

Table 2. Summary of intrinsic membrane properties of RS, PV and SOM cell types.

	Biological			**Model**		
	RS cell	PV cell	SOM$^+$ cell	RS cell	PV cell	SOM cell
Resting membrane potential (mV)	-77.8 ± 0.7	-82.6 ± 1.7	-67.1 ± 2.5	-77.62	-82.6	-67
Input resistance (MΩ)	300.5 ± 26.3	339.3 ± 47.3	403 ± 39	311.9	351.5	400.4
Membrane time constant (ms)	52.8 ± 2.6	24.3 ± 5.7	33.9 ± 4.1	53.1	21	32

Table 3 Intrinsic connectivity (mean ± SEM) comparison between CCs and control cells with other RS cells that fired during paired TFS.

Cell type and total #	# short range conn. recd. from spiking RS cells	# long range conn. recd. from spiking RS cells	# short range conn. made to spiking RS cells	# long range conn. made to spiking RS cells
CCs at-site (2 and 8 mm sites) - 40	5.65 ± 0.4	9.95 ± 0.34	5.4 ± 0.35	8.2 ± 0.53
CCs off-site - 44	2.98 ± 0.3	10.84 ± 0.42	2.34 + 0.3	9.86 ± 0.53
Control Cells at-site (2 and 8 mm sites) - 120	3.76 ± 0.17	5.84 ± 0.21	4.74 ± 0.21	6.06 ± 0.3
Control Cells off-site - 196	1.53 ± 0.11	7.3 ± 0.21	1.49 ± 0.1	7.43 ± 0.27

Table 4. Incidence of CCs, plastic cells, and non-plastic cells with respect to the paired neocortical sites.

	CCs	**Plastic**	**Non-plastic**	**Total**
At-Site	34.5 ± 2.12	71.6 ± 2.05	53.09 ± 1.66	159.19 ± 5.83
Off-Site	42.1 ± 3.6	53.4 ± 3.61	144.5 ± 6.56	240 ± 13.77

2.9 FIGURES

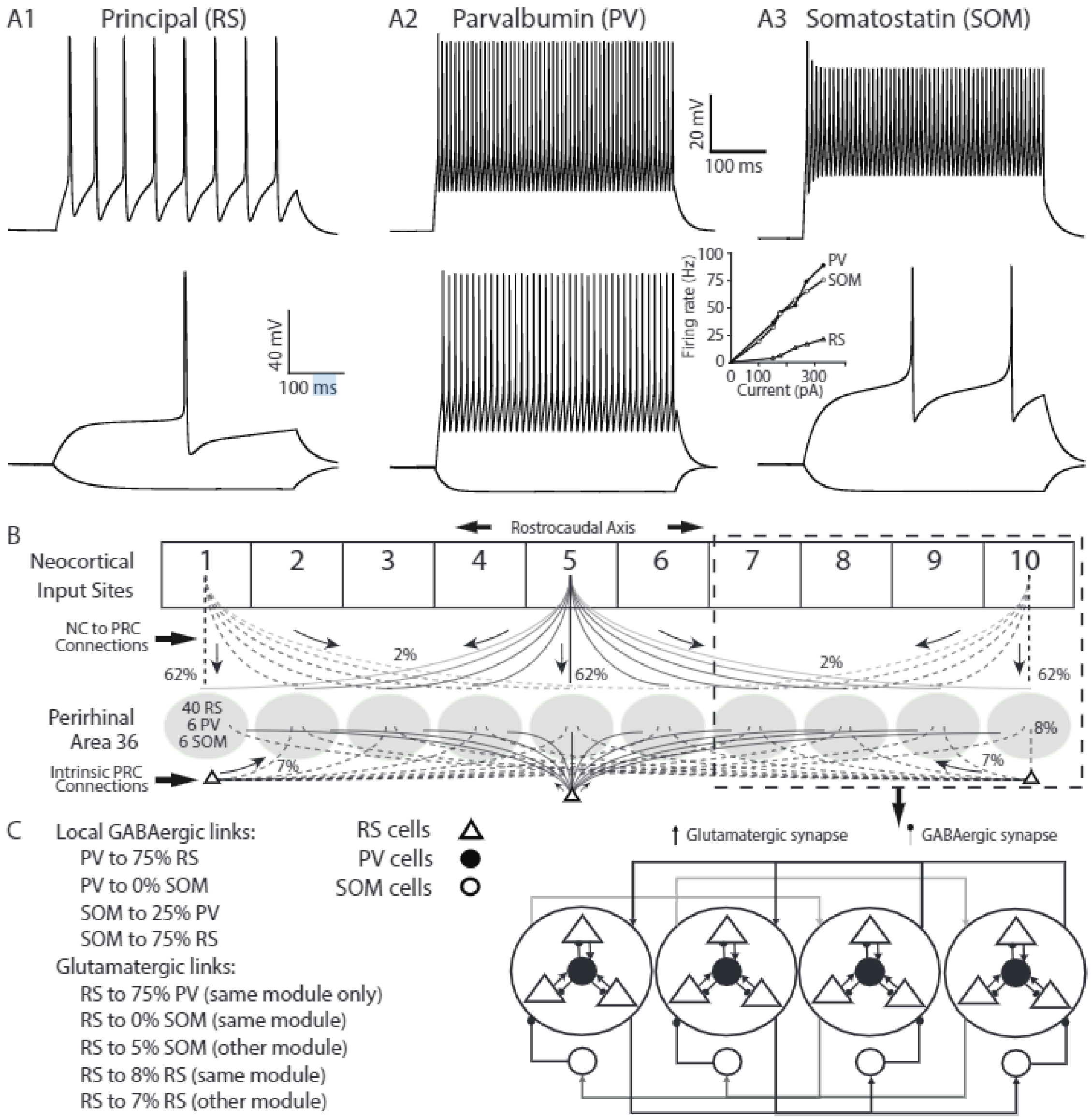

Figure 1. Physiological properties of model neurons and connectivity of the model. (**A**) Voltage responses of regular spiking (RS, **A1**), parvalbumin (PV, **A2**), and somatostatin (SOM, **A3**) cells to hyperpolarizing and depolarizing current pulses. All negative current pulses have the same amplitude (-100 pA). Positive current pulses from top to bottom are (in pA): RS, 230 and 122; FS, 330, 230; SOM. 400, 67. **Inset** between A2 and A3 plots firing rate as a function of injected

current in the three cell types. (**B**) Overall connectivity of perirhinal network model. The model received topographically organized inputs from the neocortex (top). Neocortical connections were strongest to the perirhinal levels in rostrocaudal register (to 62% of RS cells) and decayed exponentially with distance such that beyond 3 mm, only 2% of RS cells were contacted by neocortical inputs. In contrast, RS perirhinal neurons contacted a similar proportion of RS cells irrespective of rostrocaudal distance to their targets. Note that there were no spatial discontinuities (boundaries) in the perirhinal model. The gray ellipses are used for illustration purposes only. (**C**) Local connectivity of the model. RS cells, gray triangles; PV interneurons, black circles; SOM interneurons, white circles.

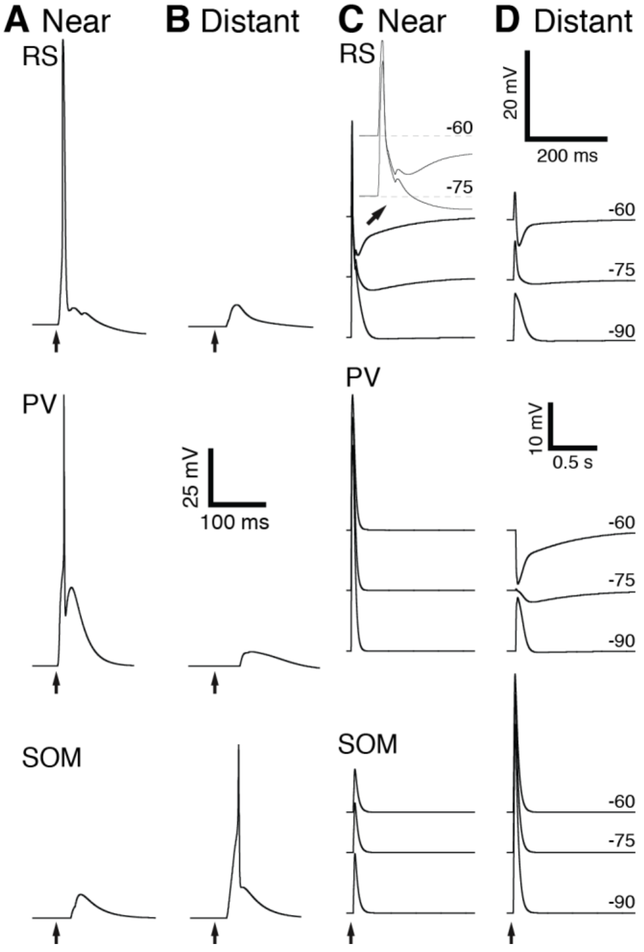

Figure 2. Response of model neurons to neocortical stimuli applied at nearby and distant neocortical sites. (**A,C**) Nearby neocortical stimulus. (**B,D**) Distant neocortical stimulus. **Top to Bottom**: principal regular spiking (RS) neuron, parvalbumin (PV) interneuron, somatostatin (SOM) interneuron. (**A,B**) Neocortical stimulus applied while neurons were at rest. (**C,D**) Neocortical stimulus applied while the membrane potential of the depicted cells was set to -60, -75, or -90 mV by simulated direct current injection. In **C** and **D**, the voltage-dependent Na^+ conductance was set to zero so that synaptic responses could be examined without the

contaminating influence of spikes and afterhyperpolarizations. **Inset** at top of C: expanded depiction of RS response to nearby neocortical stimuli.

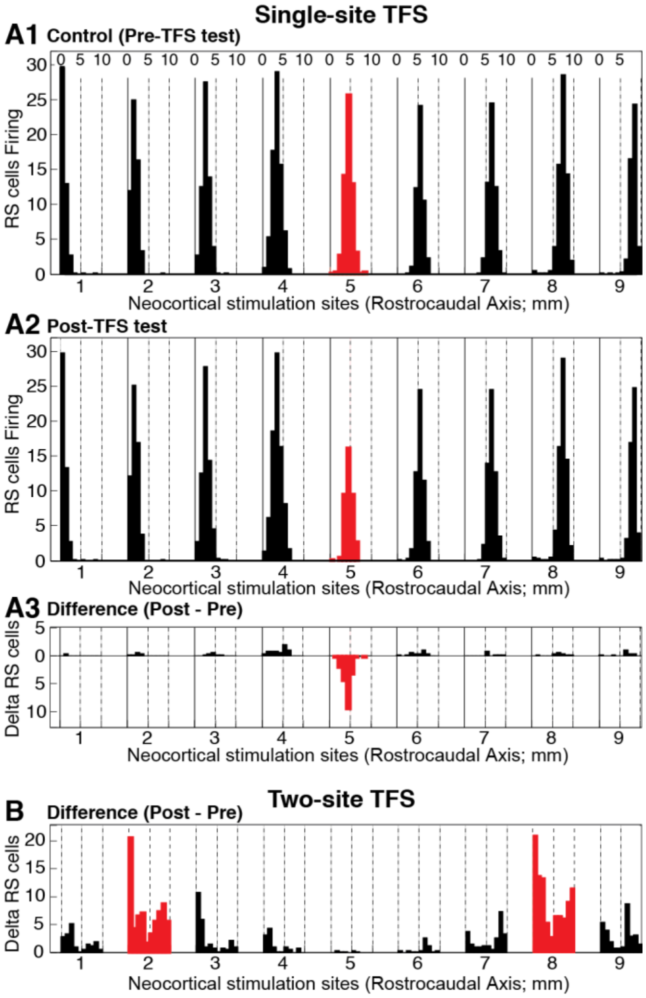

Figure 3. Contrasting effects of one- and two site TFS. (**A**) One-site TFS. (**B**) Two-site TFS. (**A**) Number of RS cells firing (y-axis) in response to different neocortical stimulation sites (x-axis) before (**A1**) and after (**A2**) TFS. (**A3**) Difference between A1 and A2. At each stimulation site, there is a ten-bin histogram, one for each target location in the perirhinal cortex. Each target location contains 80 RS cells. The numbers (0,5,10) at the top of A1 refer to these ten target locations and apply to all graphs below. (**B**) Difference between the number of RS cells firing in response to neocortical stimuli before vs. after TFS. Red indicates responses elicited by neocortical stimuli where TFS was applied.

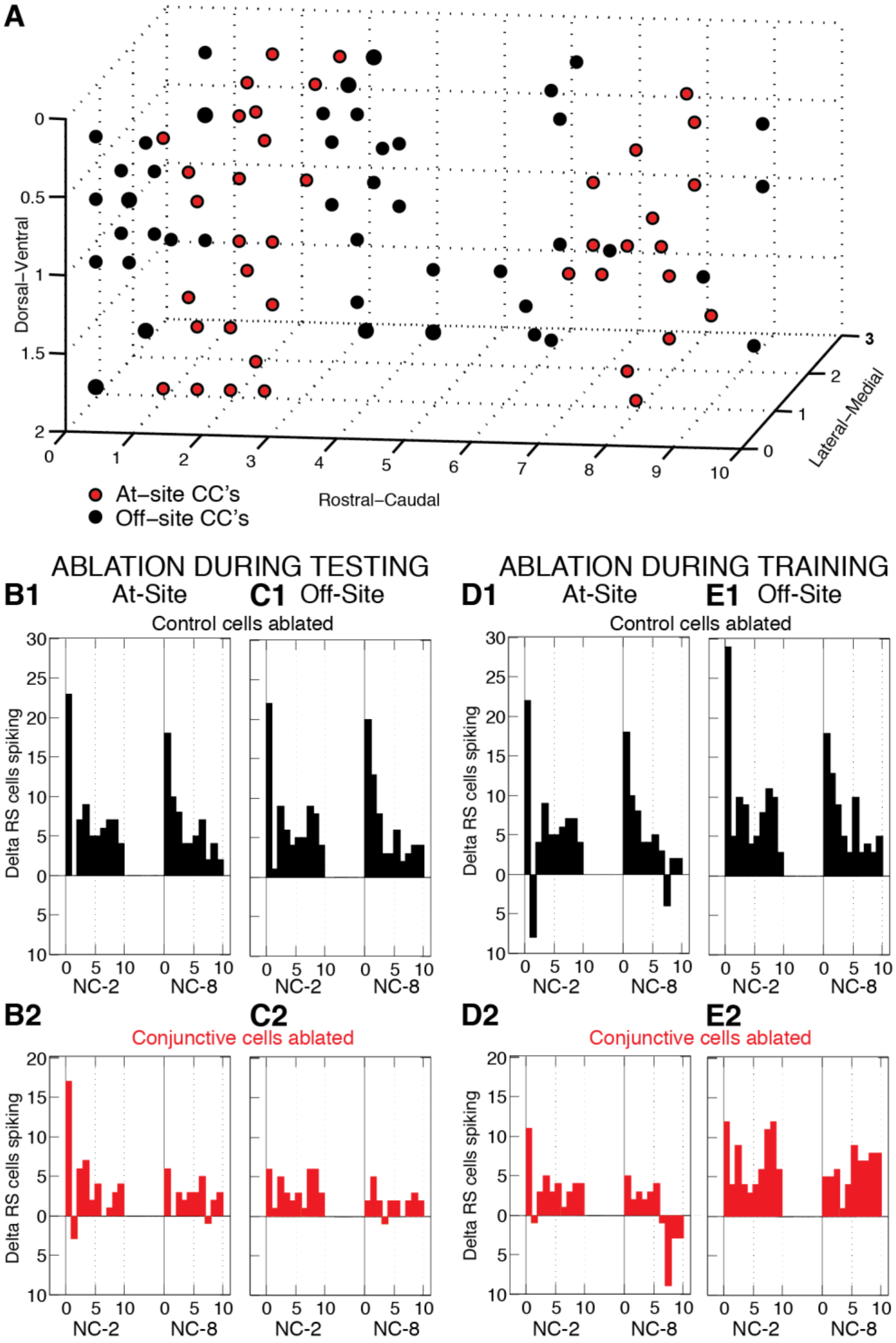

Figure 4. CCs play a critical role in the induction and expression of plasticity induced by two-site TFS. (**A**) Location of at-site (red) and off-site (black) CCs. CCs were defined as RS cells that responded to independent stimulation of both paired sites after two-site TFS. (**B-E**) Histograms showing differences in the number of RS cells spiking (y-axis) after vs. before two-site TFS in

response to stimulation of site 2 (NC-2) or site 8 (NC-8). Randomly selected RS cells (panels 1, black) or an equal number of CCs (panels 2, red) were ablated only during testing (**B,C**) or training (**D,E**). Ablated cells were either located at the same rostrocaudal level as the paired neocortical stimulation sites (**B,D**) or not (**C,E**)

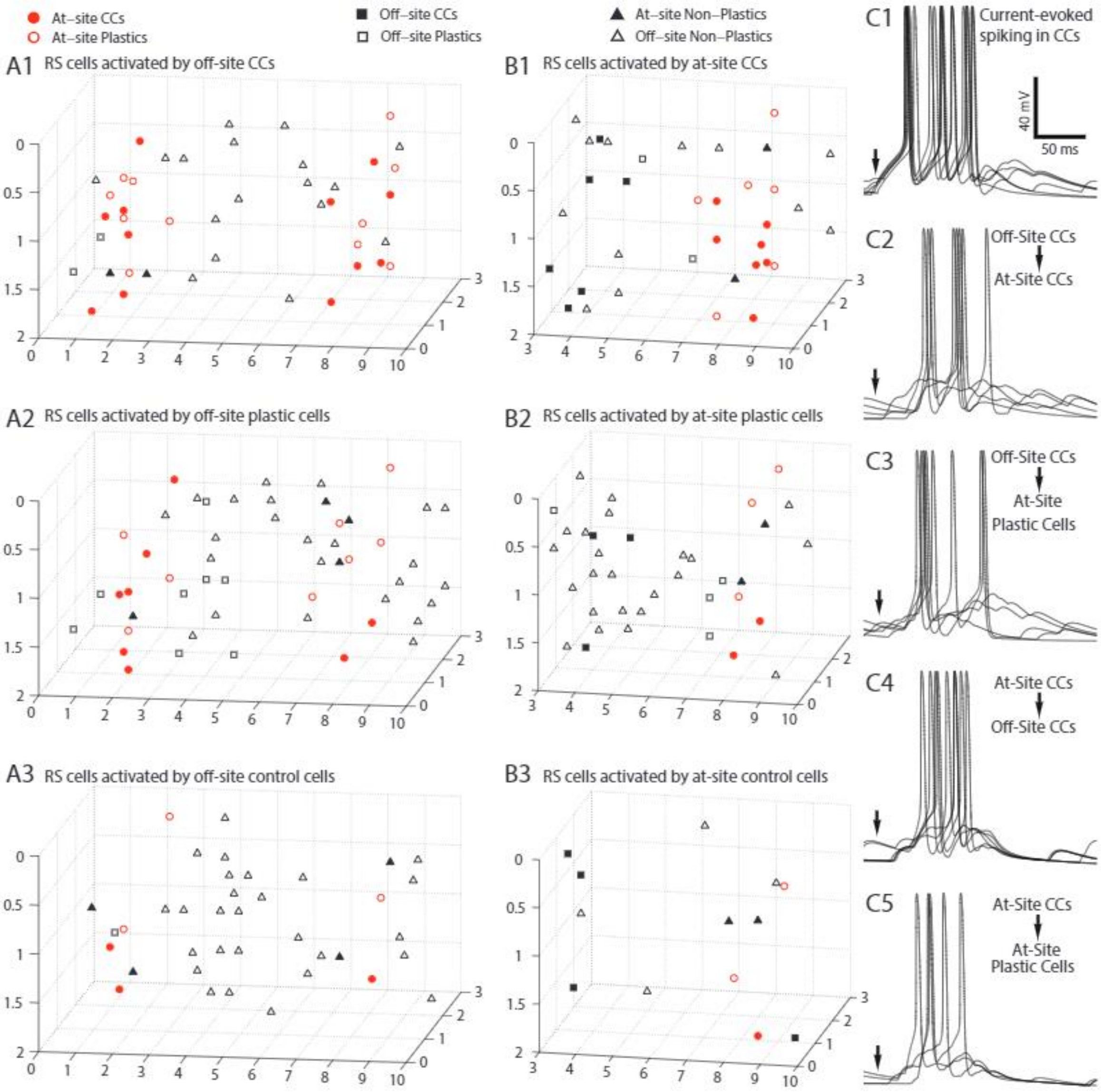

Figure 5. Firing in CCs after training reactivates plastic neurons. (**A**) Location of RS cells activated by current-evoked spiking in off-site CCs (**A1**), in an equal number of off-site plastic cells (**A2**), or off-site control cells (**A3**). The meaning of the symbols is indicated at the top of the figure. (**B**) Location of RS cells activated by current-evoked spiking in CCs at-site 2 (**B1**), in an equal number at-site plastic cells (**B2**), or at-site control cells (**B3**). (**C**) Examples of voltage responses in the various conditions illustrated in A and B. In these simulations, random uncorrelated synaptic inputs were injected in all cells so that they would fire at an average of ~0.6 Hz, as seen in vivo. (**C1**) Current-evoked spiking in CCs. (**C2**) Response of at-

site CCs to current-evoked spiking in off-site CCs. (**C3**) Response of at-site plastic (non-conjunctive) cells to current-evoked spiking in off-site CCs. (**C4**) Response of off-site CCs to current-evoked spiking in at-site CCs. (**E5**) Response of at-site plastic (non-conjunctive) cells to current-evoked spiking in at-site CCs.

2.10 REFERENCES

Aggleton JP, Hunt PR, Rawlins JN. 1986. The effects of hippocampal lesions upon spatial and non-spatial tests of working memory. Behav Brain Res. 1986; 19:133-146.

Adesnik H, Bruns W, Taniguchi H, Huang ZJ, Scanziani M. 2012. A neural circuit for spatial summation in visual cortex. Nature. 490:226-31.

Bang SJ, Brown TH. 2009. Muscarinic receptors in perirhinal cortex control trace conditioning. J Neurosci. 29:4346-4350.

Barker GRI, Bashir ZI, Brown MW, Warburton EC. 2006a. A temporally distinct role for group I and group II metabotropic glutamate receptors in object recognition memory. Learn Mem. 13:178-186.

Barker GRI, Warburton EC, Koder T, Dolman NP, More JCA, Aggleton JP, Bashir ZI, Auberson YP, Jane DE, Brown MW. 2006b. The different effects on recognition memory of perirhinal kainate and NMDA glutamate receptor antagonism: Implications for underlying plasticity mechanisms. J Neurosci. 26:3561-3566.

Beggs JM, Kairiss EW. 1994. Electrophysiology and morphology of neurons in rat perirhinal cortex. Brain Res. 665:18-32.

Biella G, Uva L, de Curtis M. 2001. Network activity evoked by neocortical stimulation in area 36 of the guinea pig perirhinal cortex. J Neurophysiol. 86:164-172.

Biella G, Uva L, de Curtis M. 2002. Propagation of neuronal activity along the neocortical-perirhinal-entorhinal pathway in the guinea pig. J Neurosci. 22:9972-9979.

Bilkey DK. 1996. Long-term potentiation in the in vitro perirhinal cortex displays associative properties. Brain Res. 733:297-300.

Brown MW, Wilson FAW, Riches IP. 1987. Neuronal evidence that inferomedial temporal cortex is more important than hippocampus in certain processes underlying recognition memory. Brain Res. 409:158-167.

Buckley MJ, Gaffan D. 1998. Learning and transfer of object-reward associations and the role of the perirhinal cortex. Behav Neurosci. 112:15-23.

Burwell RD, Witter MP, Amaral DG. 1995. Perirhinal and postrhinal cortices of the rat: a review of the neuroanatomical literature and comparison with findings from the monkey brain. Hippocampus. 5:390-408.

Burwell RD. 2000. The parahippocampal region: Corticocortical connectivity. Ann N Y Acad Sci. 911:25-42.

Burwell RD, Amaral DG. 1998a. Cortical afferents of the perirhinal, postrhinal, and entorhinal cortices of the rat. J Comp Neurol. 398:179-205.

Burwell RD, Amaral DG. 1998b. Perirhinal and postrhinal cortices of the rat: Interconnectivity and connections with the entorhinal cortex. J Comp Neurol. 391:293-321.

Bush PC, Sejnowski TJ .1993. Reduced compartmental models of neocortical pyramidal cells. J Neurosci Methods. 46: 159-166.

Cho K, Aggleton JP, Brown MW, Bashir ZI. 2001. An experimental test of the role of postsynaptic calcium levels in determining synaptic strength using perirhinal cortex of rat. J Physiol. 532:459-466.

Cho K, Bashir ZI. 2002. Cooperation between mglu receptors: A depressing mechanism? Trends Neurosci. 25:405-411.

Cho K, Brown MW, Bashir ZI. 2002. Mechanisms and physiological role of enhancement of mGlu5 receptor function by group II mGlu receptor activation in rat perirhinal cortex. J Physiol. 540:895-906.

Cho K, Kemp N, Noel J, Aggleton JP, Brown MW, Bashir ZI. 2000. A new form of long-term depression in the perirhinal cortex. Nat Neurosci.3:150-156.

Collins DR, Lang EJ, Paré D. 1999. Spontaneous activity of the perirhinal cortex in behaving cats. Neuroscience. 89:1025-1039.

D'Antuono M, Biagini G, Tancredi V, Avoli M. 2001. Electrophysiology of regular firing cells in the rat perirhinal cortex. Hippocampus.11:662-672.

Deacon TW, Eichenbaum H, Rosenberg P, Eckmann KW. 1983. Afferent connections of the perirhinal cortex in the rat. J Comp Neurol. 220:168-190.

De Curtis M, Pare D. 2004. The rhinal cortices: a wall of inhibition between the neocortex and hippocampus. Prog. Neurobiol. 74:101-110.

Dickson CT, Magistretti J, Shalinsky MH, Fransen E, Hasselmo ME, Alonso A. 2000. Properties and role of ih in the pacing of subthreshold oscillations in entorhinal cortex layer II neurons. J Neurophysiol. 83:2562-2579.

Dyhrfjeld-Johnsen J, Santhakumar V, Morgan RJ, Huerta R, Tsimring L, Soltesz I. 2007. Topological determinants of epileptogenesis in large-scale structural and functional models of the dentate gyrus derived from experimental data. J Neurophysiol. 97:1566-87.

Eichenbaum H, Schoenbaum G, Young B, Bunsey M. 1996. Functional organization of the hippocampal memory system. Proc Natl Acad Sci. USA. 93:13500-13507.

Fahy FL, Riches IP, Brown MW. 1993. Neuronal activity related to visual recognition memory: long-term memory and the encoding of recency and familiarity information in the primate anterior and medial inferior temporal cortex and rhinal cortex. Exp Brain Res. 96:457-472.

Faulkner B, Brown TH. 1999. Morphology and physiology of neurons in the rat perirhinal-lateral amygdala area. J Comp Neurol. 411:613-642.

Fino E, Packer AM, Yuste R. 2013. The logic of inhibitory connectivity in the neocortex. Neuroscientist. 19:228-37.

Fransén E, Alonso AA, Dickson CT, Magistretti J, Hasselmo ME. 2004. Ionic mechanisms in the generation of subthreshold oscillations and action potential clustering in entorhinal layer II stellate neurons. Hippocampus. 14:368-384.

Fransen E, Alonso AA, Hasselmo ME. 2002. Simulations of the role of the muscarinic-activated calcium-sensitive nonspecific cation current INCM in entorhinal neuronal activity during delayed matching tasks. J Neurosci. 22:1081-1097.

Fransén E, Tahvildari B, Egorov AV, Hasselmo ME, Alonso AA. 2006. Mechanism of graded persistent cellular activity of entorhinal cortex layer V neurons. Neuron. 49:735-746.

Furtak SC, Wei S-M, Agster KL, Burwell RD. 2007. Functional neuroanatomy of the parahippocampal region in the rat: The perirhinal and postrhinal cortices. Hippocampus. 17:709-722.

Gaffan D, Murray EA. 1992. Monkeys (Macaca fascicularis) with rhinal cortex ablations succeed in object discrimination learning despite 24-hr intertrial intervals and fail at matching to sample despite double sample presentations. Behav Neurosci. 106:30-38.

Goulet S, Murray EA. 2001. Neural substrates of crossmodal association memory in monkeys: the amygdala versus the anterior rhinal cortex. Behav Neurosci. 115:271-284.

Gupta A, Wang Y, Markram H. 2000. Organizing principles for a diversity of GABAergic interneurons and synapses in the neocortex. Science. 287:273-8.

Hemond P, Epstein D, Boley A, Migliore M, Ascoli GA, Jaffe DB. 2008. Distinct classes of pyramidal cells exhibit mutually exclusive firing patterns in hippocampal area CA3b. Hippocampus. 18:411-424.

Higuchi S, Miyashita Y. 1996. Formation of mnemonic neuronal responses to visual paired associates in inferotemporal cortex is impaired by perirhinal and entorhinal lesions. Proc Natl Acad Sci USA. 93:739-743.

Jo J, Heon S, Kim MJ, Son GH, Park Y, Henley JM, Weiss JL, Sheng M, Collingridge GL, Cho K. 2008. Metabotropic glutamate receptor-mediated ltd involves two interacting Ca2+ sensors, NCS-1 and PICK1. Neuron. 60:1095-1111.

Kawaguchi Y, Kondo S. 2002. Parvalbumin, somatostatin and cholecystokinin as chemical markers for specific GABAergic interneuron types in the rat frontal cortex. J Neurocytol. 31:277-87.

Kim D, Pare D, Nair SS. 2013. Assignment of model amygdala neurons to the fear memory trace depends on competitive synaptic interactions. J Neurosci. 33:14354 –14358.

Klausberger T, Somogyi P. 2008. Neuronal diversity and temporal dynamics: the unity of hippocampal circuit operations. Science. 321:53-7.

Leonard BW, Amaral DG, Squire LR, Zola-Morgan S. 1995. Transient memory impairment in monkeys with bilateral lesions of the entorhinal cortex. J Neurosci. 15:5367-5659.

Li L, Miller EK, Desimone R. 1993. The representation of stimulus familiarity in anterior inferior temporal cortex. J Neurophysiol. 69:1918-1929.

Ma Y, Hu H, Berrebi AS, Mathers PH, Agmon A. 2006. Distinct subtypes of somatostatin-containing neocortical interneurons revealed in transgenic mice. J Neurosci. 26(19):5069-5082.

Ma Y, Hu H, Agmon A. 2012. Short-term plasticity of unitary inhibitory-to-inhibitory synapses depends on the presynaptic interneuron subtype. J Neurosci. 32:983-8.

Martina M, Royer S, Pare D. 2001a. Cell-type-specific GABA responses and chloride homeostasis in the cortex and amygdala. J Neurophysiol. 86:2887-2895.

Martina M, Royer S, Pare D. 2001b. Propagation of neocortical inputs in the perirhinal cortex. J Neurosci. 21:2878-2888.

Massey PV, Bhabra G, Cho K, Brown MW, Bashir ZI. 2001. Activation of muscarinic receptors induces protein .synthesis-dependent long-lasting depression in the perirhinal cortex. Eur J Neurosci. 14:145-152.

Massey PV, Johnson BE, Moult PR, Auberson YP, Brown MW, Molnar E, Collingridge GL, Bashir ZI. 2004. Differential roles of NR2A and NR2B-containing NMDA receptors in cortical long-term potentiation and long-term depression. J Neurosci. 24:7821-7828.

Massey PV, Phythian D, Narduzzo K, Warburton EC, Brown MW, Bashir ZI. 2008. Learning-specific changes in long-term depression in adult perirhinal cortex. J Neurosci. 28:7548-7554.

McCaffery B, Cho K, Bortolotto ZA, Aggleton JP, Brown MW, Conquet F, Collingridge GL, Bashir ZI. 1999. Synaptic depression induced by pharmacological activation of metabotropic glutamate receptors in the perirhinal cortex in vitro. Neuroscience. 93:977-984.

Meunier M, Bachevalier J, Mishkin M, Murray EA. 1993. Effects on visual recognition of combined and separate ablations of the entorhinal and perirhinal cortex in rhesus monkeys. J Neurosci. 13:5418-5432.

Meunier M, Hadfield W, Bachevalier J, Murray EA. 1996. Effects of rhinal cortex lesions combined with hippocampectomy on visual recognition memory in rhesus monkeys. J Neurophysiol. 75:1190-1205.

Messinger A, Squire LR, Zola SM, Albright TD. 2001. Neuronal representations of stimulus associations develop in the temporal lobe during learning. Proc Natl Acad Sci USA. 98:12239-12244.

Migliore M. 2003. On the integration of subthreshold inputs from perforant path and schaffer collaterals in hippocampal CA1 pyramidal neurons. J Comput Neurosci. 14:185-192.

Migliore M, Cook EP, Jaffe DB, Turner DA, Johnston D. 1995. Computer simulations of morphologically reconstructed CA3 hippocampal neurons. J Neurophysiol. 73:1157-1168.

Migliore M, Hoffman DA, Magee JC, Johnston D. 1999. Role of an a-type K+ conductance in the back-propagation of action potentials in the dendrites of hippocampal pyramidal neurons. J Comput Neurosci. 7:5-15.

Miller EK, Li L, Desimone R. 1993. Activity of neurons in anterior inferior temporal cortex during a short-term memory task. J Neurosci. 13:1460-1478.

Moyer JR, McNay EC, Brown TH. 2002. Three classes of pyramidal neurons in layer V of rat perirhinal cortex. Hippocampus. 12:218-234.

Murray EA, Mishkin M. 1986. Visual recognition in monkeys following rhinal cortical ablations combined with either amygdalectomy or hippocampectomy. J Neurosci. 6:1991-2003.

Murray EA, Gaffan EA, Mishkin M. 1993. Neural substrate of visual stimulus-stimulus association in rhesus monkey. J Neurosci. 13:4549-4561.

Murray EA, Graham KS, Gaffan D. 2005. Perirhinal cortex and its neighbours in the medial temporal lobe: contributions to memory and perception. Q J Exp Psychol B. 58:378-396.

Naya Y, Yoshida M, Miyashita Y. 2003a. Forward processing of long-term associative memory in monkey. J Neurosci. 23:2861-2871.

Naya Y, Yoshida M, Takeda M, Fujimichi R, Miyashita Y. 2003b. Delay-period activities in two subdivisions of monkey inferotemporal cortex during pair association memory task. Eur J Neurosci.18:2915-2918.

Park Y, Jo J, Isaac JTR, Cho K. 2006. Long-term depression of kainate receptor-mediated synaptic transmission. Neuron. 49:95-106.

Parker A, Gaffan D. 1998. Lesions of the primate rhinal cortex cause deficits in flavour-visual associative memory. Behav Brain Res. 93:99-105.

Pelletier JG, Pare D. 2002. Uniform range of conduction times from the lateral amygdala to distributed perirhinal sites. J Neurophysiol. 87:1213-1221.

Pfeffer CK, Xue M, He M, Huang ZJ, Scanziani M. 2013. Inhibition of inhibition in visual cortex: the logic of connections between molecularly distinct interneurons. Nat Neurosci. 16:1068-76.

Riches IP, Wilson FA, Brown MW. 1991. The effects of visual stimulation and memory on neurons of the hippocampal formation and the neighboring parahippocampal gyrus and inferior temporal cortex of the primate. J Neurosci. 11:1763-1779.

Rolls ET, Cahusac P, Feigenbaum JD, Miyashita Y. 1993. Responses of single neurons in the hippocampus of the macaque related to recognition memory. Exp Brain Res. 93:299-306.

Room P, Groenewegen HJ. 1986. Connections of the parahippocampal cortex. I. Cortical afferents. J Comp Neurol. 251:415-450.

Rudy B, Fishell G, Lee S, Hjerling-Leffler J. 2011. Three groups of interneurons account for nearly 100% of neocortical GABAergic neurons. Dev Neurobiol. 71:45-61.

Seoane A, Massey PV, Keen H, Bashir ZI, Brown MW. 2009. L-type voltage-dependent calcium channel antagonists impair perirhinal long-term recognition memory and plasticity processes. J Neurosci. 29:9534-9544.

Silberberg G, Wu C, Markram H. 2004. Synaptic dynamics control the timing of neuronal excitation in the activated neocortical microcircuit. J Physiol. 556:19-27.

Sobotka S, Ringo JL. 1993. Investigation of long-term recognition and association memory in unit responses from inferotemporal cortex. Exp Brain Res. 96:28-38.

Storm JF. 1988. Temporal integration by a slowly inactivating K+ current in hippocampal neurons. Nature. 336:379-81.

Suzuki WA, Zola-Morgan S, Squire LR, Amaral DG. 1993. Lesions of the perirhinal and parahippocampal co.rtices in the monkey produce long-lasting memory impairment in the visual and tactual modalities. J Neurosci. 13:2430-2451.

Unal G, Apergis-Schoute J, Pare D. 2012. Associative properties of the perirhinal network. Cereb Cortex. 22:1318-1332.

Unal G, Pare JF, Smith Y, Pare D. 2013. Differential connectivity of short- vs. long-range extrinsic and intrinsic cortical inputs to perirhinal neurons. J Comp Neurol. 521:2538-50.

Uva L, Grüschke S, Biella G, Curtis Md, Witter MP. 2004. Cytoarchitectonic characterization of the parahippocampal region of the guinea pig. J Comp Neurol. 474:289-303.

Witter MP, Room P, Groenewegen HJ, Lohman AHM. 1986. Connections of the parahippocampal cortex in the cat. V. Intrinsic connections; comments on input/output connections with the hippocampus. J Comp Neurol. 252:78-94.

Witter MP, Wouterlood FG, Naber PA, Van Haeften T. 2000. Anatomical organization of the parahippocampal-hippocampal network. Ann Ny Acad Sci. 911:1-24.

Xiang JZ, Brown MW. 1998. Differential neuronal encoding of novelty, familiarity and recency in regions of the anterior temporal lobe. Neuropharmacology. 37:657-676.

Zhang S, Xu M, Kamigaki T, Hoang Do JP, Chang WC, Jenvay S, Miyamichi K, Luo L, Dan Y. 2014. Selective attention. Long-range and local circuits for top-down modulation of visual cortex processing. Science. 345:660-5.

Ziakopoulos Z, Tillett CW, Brown MW, Bashir ZI. 1999. Input- and layer-dependent synaptic plasticity in the rat perirhinal cortex in vitro. Neuroscience. 92:459-472.

Ziakopoulos Z, Brown MW, Bashir ZI. 2000. GABAB receptors mediate frequency-dependent depression of excitatory potentials in rat perirhinal cortex in vitro. Eur J Neurosci. 12:803-9.

Zola-Morgan S, Squire LR, Amaral DG, Suzuki WA. 1989. Lesions of perirhinal and parahippocampal cortex that spare the amygdala and hippocampal formation produce severe memory impairment. J Neurosci. 9:4355-4370.

2.11 SUPPLEMENTARY MATERIALS

Here we list additional information related to methods, including mathematical equations, and parameter values. All model runs were performed using parallel NEURON (Carnevale and Hines, 2006) running on a Beowulf supercluster with a time step of 10 µs. Simulation output was analyzed using MATLAB.

S.1. Mathematical equations for voltage-dependent ionic currents

The equation for each compartment (soma or dendrite) followed the Hodgkin-Huxley formulation (Byrne and Roberts, 2004; Li et al. 2009; Kim et al. 2013) in eqn. S1,

$$C_m dV_s/dt = -g_L(V_s - E_L) - g_c(V_s - V_d) - \sum I_{cur,s}^{int} - \sum I_{cur,s}^{syn} + I_{inj} \qquad \text{(S1)}$$

where V_s/V_d are the somatic/dendritic membrane potential (mV), $I_{cur,s}^{int}$ and $I_{cur,s}^{syn}$ are the intrinsic and synaptic currents in the soma, I_{inj} is the electrode current applied to the soma, C_m is the membrane capacitance, g_L is the is the conductance of leak channel, g_c is the coupling conductance between the soma and the dendrite (similar term added for other dendrites connected to the soma), and E_L is the leak reversal potential. Eqn. S1 represents a current balance, with the sum of all currents being equal to the injected current. The term on the left represents the capacitance current. The intrinsic current $I_{cur,s}^{int}$, was modeled as $I_{cur,s}^{int} = g_{cur} m^p h^q (V_s - E_{cur})$, where g_{cur} is its maximal conductance, *m* its activation variable (with exponent *p*), *h* its inactivation variable (with exponent *q*), and E_{cur} its reversal potential (a similar equation is used for the synaptic current $I_{cur,s}^{syn}$ but without *m* and *h*). The kinetic equation for each of the gating variables *x* (*m* or *h*) takes the form

$$\frac{dx}{dt} = \frac{x_\infty\left(V,[Ca^{2+}]_i\right) - x}{\tau_x(V,[Ca^{2+}]_i)} \qquad \text{(S2)}$$

where x_∞ is the steady state gating voltage- and/or Ca^{2+}- dependent gating variable and τ_x is the voltage- and/or Ca^{2+}- dependent time constant. The equation for the dendrite follows the same format with 's' and 'd' switching positions in eqn. S1. Details related to the individual currents are listed tables S1.

S.2. Mathematical equations for synaptic currents

Excitatory transmission was mediated by AMPA/NMDA receptors, and inhibitory transmission by GABA$_A$ and GABA$_B$ receptors. The corresponding synaptic currents were modeled by dual exponential functions (Durstewitz et al. 2000), as shown in eqns. S3-5,

$$I_{AMPA} = w(t) * G_{AMPA} * (V - E_{AMPA})$$

$$G_{AMPA} = g_{AMPA,max} * STP_{AMPA} * r_{AMPA}$$

$$r_{AMPA}{}' = \alpha Tmax_{AMPA} * ON_{AMPA} * (1 - r_{AMPA}) - \beta_{AMPA} * r_{AMPA} \tag{S3}$$

$$I_{NMDA} = w * G_{NMDA} * (V - E_{NMDA})$$

$$G_{NMDA} = g_{NMDA,max} * STP_{NMDA} * s(V) * r_{NMDA}$$

$$r_{NMDA}{}' = \alpha Tmax_{NMDA} * ON_{NMDA} * (1 - r_{NMDA}) - \beta_{NMDA} * r_{NMDA} \tag{S4}$$

$$I_{GABAa} = -W_{base} G_{GABAa} (B_{Ga} - A_{Ga})(V - E_{GABAa})$$

$$I_{GABAb} = -W_{base} G_{GABAb} (B_{Gb} - A_{Gb})(V - E_{GABAb})$$

$$\tau_{Ga1} \frac{dA_{Ga}}{dt} = -A_{Ga};\ \tau_{Ga2} \frac{dB_{Ga}}{dt} = -B_{Ga}$$

$$\tau_{Gb1} \frac{dA_{Gb}}{dt} = -A_{Gb}; \tau_{Gb2} \frac{dB_{Gb}}{dt} = -B_{Gb} \tag{S5}$$

where V is the membrane potential (mV) of the compartment (dendrite or soma) where the synapse is located and w is the adjustable synaptic weight for the synapse (w was variable for AMPA synapses, but fixed for NMDA and GABA synapses). The synaptic reversal potentials were $E_{\mathrm{AMPA}} = E_{\mathrm{NMDA}} = 0$ mV, $E_{\mathrm{GABAa}} = -75$ mV and $E_{\mathrm{GABAb}} = -92$ mV (Durstewitz et al. 2000;

Martina et al. 2001a). The terms ON_{NMDA} and ON_{AMPA} are set to 1 if the corresponding receptor is open, else to 0. The receptor opening duration is determined by Cdur_NMDA for NMDA receptors and Cdur_AMPA for AMPA receptors. The kinetics for the synaptic receptors were determined from Mahanty and Sah (1998) and Weisskopf and LeDoux (1999). Values for the specific parameters are listed in table S3.

S.3. Long-term synaptic plasticity

Long term synaptic plasticity in AMPA synapses was implemented using the model in Eq. S6.

$$
\begin{aligned}
&W_{i,j\,AMPA} = Wn_{i,j} + Wm_{i,j} \quad ,where \\
&\frac{dWn_{i,j}}{dt} = \eta([Ca^{2+}]_{NMDA})\left(\lambda_1\Omega_1([Ca^{2+}]_{NMDA}) - \lambda_3\left(W_{i,j} - W_{init}\right)\right) \\
&\frac{dWm_{i,j}}{dt} = \eta([Ca^{2+}]_{mGluR})\left(\lambda_2\Omega_2([Ca^{2+}]_{mGluR}) - \lambda_3\left(W_{i,j} - W_{init}\right)\right) \\
&\eta([Ca^{2+}]) = 0.001(0.1(1 \times 10^{-5} + [Ca^{2+}]^3)^{-1} + 1)^{-1} \\
&\Omega_1([Ca^{2+}]_{NMDA}) = \begin{cases} 0, & [Ca^{2+}]_{NMDA} < \theta_d \\ -\sqrt{\left(\frac{\theta_p - \theta_d}{2}\right)^2 + \left(\frac{[Ca^{2+}]_{NMDA} - (\theta_p + \theta_d)}{2}\right)^2}, & \theta_d < [Ca^{2+}]_{NMDA} < \theta_p \\ \left(1 + \exp\left(-50([Ca^{2+}]_{NMDA} - \theta_p)\right)\right), & \theta_p < [Ca^{2+}]_{NMDA} \end{cases} \\
&\Omega_2([Ca^{2+}]_{mGluR}) = \begin{cases} 0, & [Ca^{2+}]_{mGluR} < \theta_m \\ -(1 + \exp(-50([Ca^{2+}]_{mGluR} - \theta_m))), & \theta_m < [Ca^{2+}]_{mGluR} \end{cases}
\end{aligned}
\tag{S6}
$$

The first term of the right side of the first equation controlled NMDAR-dependent plasticity (Shouval et al. 2002b, Castellani et al. 2005), and the second term controlled Group I mGluR-dependent plasticity. The η function controls the rate of synaptic plasticity; i.e., higher Ca^{2+} concentration results in faster weight changes. The functions Ω_1 and Ω_2 determine the Ca^{2+}-dependent amplitude and sign of change in weight. While Ω_1 is taken directly from previous studies (Shouval et al. 2002b), Ω_2 was designed to simulate Group I mGluR-LTD, and was based on the assumption that increasing Ca^{2+} release from the endoplasmic reticulum (ER) will result in increasing LTD. The term ($W_{i,j}$–W_{init}) ensured that over time and in the absence of significant inputs, the weights would eventually return to their initial values. However, this process was exceptionally slow compared to the length of the simulation protocol, and could thus model the decay of memory in these connections over the course of a few days. The factors λ_1 and λ_2 controlled the relative strengths of NMDAR- and Group I mGluR-dependent plasticity, respectively.

The action of NMDA receptors in activity-dependent LTP and LTD was captured by a model of plasticity that represents the phosphorylation and dephosphorylation of AMPA receptors by Ca^{2+} and Ca^{2+}-calmodulin dependent protein kinase and phosphatase cascades (Castellani et al. 2001; Shouval et al. 2002a; Shouval et al. 2002b; Yeung et al. 2004; Castellani et al. 2005; Aslam et al. 2009; Castellani et al. 2009; Shouval et al. 2010). In short, Ca^{2+} influx through synaptic NMDA receptor channels controls plasticity; a moderate Ca^{2+} influx triggers LTD, while a large Ca^{2+} influx instead triggers LTP. The equation governing Ca^{2+}influx through NMDA receptors are shown in Eq. S7. In this set of equations, the Ca^{2+} concentration is governed by Ca^{2+} influx through NMDA receptors (J_{NMDA}, which was determined by the reversal potential of Ca^{2+} rather than that of total NMDA current) as well as by three pumps: an equilibration pump that ensured that the resting $[Ca^{2+}]_{\mathrm{NMDA}}$ stayed near 50 nM (J_{eq}), a low-affinity pump that extruded Ca^{2+} outside of the plasma membrane ($J_{\mathrm{PMCA,N}}$), and a high-affinity Na^+- Ca^{2+} exchanger ($J_{\mathrm{NCX,N}}$) (De Young and Keizer, 1992; Li and Rinzel, 1994; Li et al. 1997; Blackwell, 2005; Fletcher and Li, 2009).

$$\frac{d[Ca^{2+}]_{NMDA}}{dt} = J_{NMDA} + J_{eq} - J_{PMCA,N} - J_{NCX,N} \tag{S7}$$

Following the example of this Ca^{2+}-dependent plasticity model, a model of Group I mGluR-dependent LTD was developed based on the G_q protein-dependent release of Ca^{2+} from the ER via IP_3 activation (De Young and Keizer, 1992; Li and Rinzel, 1994; Li et al. 1994; Li et al. 1997; Fletcher and Li, 2009). In this model, the accumulation of Ca^{2+} from ER release due to Group I mGluR activation causes LTD of AMPA receptor currents through a PKC-dependent process (Jo et al. 2008). Equation S8 shows the model used to control $[Ca^{2+}]_{\mathrm{mGluR}}$ (flux equations are listed in table S2). According to this equation, $[Ca^{2+}]_{\mathrm{mGluR}}$ flowed to and from both the extracellular region and the ER. J_{in} was the sum of Ca^{2+} entering through L-type voltage-gated Ca^{2+} channels (J_{VGCC}) and through a store-operated Ca^{2+} pump (J_{SOC}), which ensured that $[Ca^{2+}]_{\mathrm{mGluR}}$ was not depleted entirely. J_{out} was the sum of Ca^{2+} extruded through two pumps ($J_{\mathrm{PMCA,M}}$ and $J_{\mathrm{NCX,M}}$) as was the case with $[Ca^{2+}]_{\mathrm{NMDA}}$. Ca^{2+} flow to and from the ER was controlled by the action of IP_3R-dependent channels (J_{IP3R}) on the ER membrane and by a pump (J_{SERCA}) that refilled the ER from $[Ca^{2+}]_{\mathrm{mGluR}}$ (Fletcher and Li, 2009).

$$\frac{d[Ca^{2+}]_{mGluR}}{dt} = F_{\beta}(J_{in} - J_{out}) + F_{cyt}(J_{IP3R} - J_{SERCA}) \tag{S8}$$

The kinetics of the IP_3 receptor-dependent Ca^{2+} release from the ER were modeled in a manner similar to both active and passive Hodgkin-Huxley dynamics, where the activation and inactivation of the IP3R channels is dependent upon $[IP_3]$, $[Ca^{2+}]_{\mathrm{mGluR}}$, and $[Ca^{2+}]_{\mathrm{ER}}$ rather than membrane voltage, as shown in Eq. S9. The equations for *m* and *h* are provided in table S2 (Koch and Segev, 1989, Li and Rinzel, 1994, Fletcher and Li, 2009).

$$J_{IP3R} = (V_R m^3 h^3 + V_L)([Ca^{2+}]_{ER} - [Ca^{2+}]_{mGluR}) \tag{S9}$$

The dynamics of $[Ca^{2+}]_{ER}$ were controlled as in Eq. S10, where the IP_3R-dependent flow is removed from the ER, and it is refilled by the SERCA pump (Fletcher and Li, 2009).

$$\frac{d[Ca^{2+}]_{ER}}{dt} = F_{ER}(J_{SERCA} - J_{IP3R}) \qquad \text{(S10)}$$

IP_3 accumulation was assumed to be triggered by Group I mGluR activation in response to presynaptic spikes in a manner similar to that of the binding and unbinding dynamics of synaptic receptor channels. Accordingly, the concentration of IP_3 was calculated as $[IP_3] = \upsilon_{IP3}(B_{IP3} - A_{IP3})$, where B_{IP3} and A_{IP3} were calculated as for synaptic currents. The parameter values used in the equations controlling synaptic plasticity are provided in the table S3.

S.4. Short-term presynaptic plasticity

Short term plasticity was implemented as follows (Varela et. al 1997; Li et al. 2011; Hummos et al. 2014): For facilitation, the factor F was calculated using eqn. S11.

$$\tau_F * \frac{dF}{dt} = 1 - F;\ F(0) = 1, \text{ and it was constrained to be} \geq 1 \qquad \text{(S11)}$$

After each stimulus, F was multiplied by a constant f (≥ 1) representing the amount of facilitation per pre-synaptic action potential, and updated as $F \rightarrow F * f$. Between stimuli, F recovered exponentially back to 1. A similar scheme was used to calculate the factor D for depression,

$$\tau_{Di} * \frac{dDi}{dt} = 1 - D_i;\ D_i(0) = 1, \text{ and it was constrained to be} \leq 1 \qquad \text{(S12)}$$

Where i varied from 1 to the number of depression factors, permitting use of different time constants. After each stimulus, D_i was multiplied by a constant d_i (≤ 1) representing the amount of depression per pre-synaptic action potential, and updated as $D_i \rightarrow D_i * d_i$. Between stimuli, D_i recovered exponentially back toward 1. We modeled depression using two factors d_1 and d_2 with d_1 being fast and d_2 being slow subtypes. The parameters for the short-term plasticity models used were: RS-RS connections: d_1 = 0.5, d_2 = 0.5, τ_{d1}= 25 ms and τ_{d2}= 25 ms; SOM to RS connections: f = 1.2, τ_f= 20 ms and $F_{\max}$ = 3.

S.5. Interaction between NMDAR and Group I mGluR mechanisms

It has been reported that Group I mGluR activation results in increase in the NMDA current through G-protein mediated mechanisms and this interaction is blocked by Group I mGluR antagonists (Krieger et al. 2000). To incorporate this, the increase in NMDA current was modeled as an increase in maximal conductance of NMDA (G_{NMDA}) as shown in equation S13,

$$G_{NMDA} = \frac{1.2}{1+1.4*\exp\left(-0.4*[Ca^{2+}]_{mGluR}\right)} \text{ nS} \tag{S13}$$

For the Group I mGluR blocking case this equation was further modified as follows, to incorporate the change in NMDA conductance,

$$G_{NMDA} = \frac{1.05}{1+1.4*\exp\left(-0.4*[Ca^{2+}]_{mGluR}\right)} \text{ nS} \tag{S14}$$

We also assumed an interaction in the reverse direction with NMDAR activation resulting in increases in the level of Group I mGluR calcium pool concentration $[Ca^{2+}]_{\mathrm{mGluR}}$, by adding 0.6% of $[Ca^{2+}]_{\mathrm{NMDA}}$ to the mGluR pool.

S.6. Neocortical connectivity

The probability of neocortical connections to RS cells was computed as

$$P_{RS}(dx) = 100\% \times (0.02 + 0.62\exp(-dx^2/2)) \tag{S15}$$

The latency of neocortically-evoked responses is known to depend on the rostrocaudal distance between the neocortical stimulation site and the recorded cell (Martina et al. 2001b). When the two are in rostrocaudal register, the latency is shortest (around 3-4 ms). Thus, in the model, synaptic delays (*Δt*) were determined according to the absolute distance *R* between the neocortical source and the target perirhinal cell as

$$\Delta t(R) = \left(9.5 - 5.5\cos\left(\frac{\pi R}{R_{max}}\right)\right) \times rand \quad \text{(msec)} \qquad \text{(S16)}$$

where $R_{\max}$ = 10.63 mm is the maximum possible distance between source and target (measured diagonally), and *rand* is a random number selected uniformly between 0.5 and 1.5 to produce appropriate variability in response latencies.

Thus, in the model, neocortical connections were made with perirhinal cells based on a Gaussian distribution with peak probability at dx = 0, where dx is the rostrocaudal distance between the target perirhinal cell and the neocortical source. The parameters chosen result in peak and minimum probabilities of 62% and 2% for connections to RS cells

S.7. Synaptic delays

Previous electrophysiological analyses (Pelletier et al. 2002) indicate that in the perirhinal cortex, conduction delays increase linearly with rostrocaudal distance between the source and target neurons. Accordingly, all synaptic delays in the model were calculated according to absolute distance *R* between the source and target cells using the formula $\Delta t(R) = 1.0 + 2.5R + rand \times (1 - \exp\ (-R^2/3))$ (in ms). A random value $rand \times (1 - \exp\ (-R^2/3))$ was chosen with *rand* between -0.1 and 0.1 to produce appropriate variability in intrinsic synaptic delays. The delay from SOM to PV cell was a constant 2 ms.

S.8. Model Setup

Our group has worked with different types of firing rate models (Ball et al. 2012). Initially, we used the firing rate formulation for the present model but encountered various problems, including the following: (i) developing different types of single cell firing rate models that matched experimentally observed passive and active properties was a challenge (Ball et al. 2012); (ii) implementing the NMDAR and mGluR-based plasticity mechanisms was problematic since they depend on the membrane potential of the cell rather than its firing rate; and (iii) the spatially segregated inhibition, via different types of interneurons could not be implemented in this framework. Also, we planned on adding the effects of neuromodulators into the next version of the model and since neuromodulators are known to affect single channel properties, firing rate models would have been inadequate. Although some of these issues can be solved, for instance, by integrating firing rate to get membrane potential (as we did in Ball et al. 2012), these steps increase the complexity of the single cell model. We have also developed Izhikevich-type cells, another class of simplified models, to analyze pattern separation/completion dynamics in hippocampal networks (Hummos et al. 2014). We had difficulty incorporating NMDAR-based plasticity mechanisms, neuromodulator effects and spatially segregated inhibition into that model. For all these reasons, we chose the Hodgkin-Huxley formulation for modeling single cells in the present research. With the availability of fast computing platforms, adding compartments to the single cell model was not an issue at all, compared to the realism it provided.

S.9. Model Validation

S.9.1. Network mechanisms underlying the contrasting effects of TFS at one vs. two distant neocortical sites

Unal et al. (2012) proposed that the contrasting effects of TFS at one vs. two neocortical sites depend on the extent to which the stimulated neocortical activity pattern recruited longitudinal perirhinal connections. This idea is based on earlier observations indicating that the long-range horizontal pathways that convey neocortical influences to rostrocaudally distant perirhinal levels do not engage presumed PV interneurons, whereas short-range connections do (Martina et al. 2001b). As a result, RS cells would respond differently depending on their position relative to the neocortical stimulation site. For RS cells in transverse register with the stimulation site, neocortical inputs would recruit PV neurons, thus limiting the depolarization elicited by neocortical afferents. When these inputs are paired with the activation of a rostrocaudally distant group of neocortical neurons, this would shift the balance toward excitation because long-range longitudinal pathways do not engage PV interneurons. By removing the Mg^{2+} block of NMDA receptors, this increased depolarization would lead to the induction of NMDA-dependent LTP. To test these ideas, we ran simulations where longitudinal perirhinal pathways were transiently "inactivated" during two-site TFS but were functional in the control and post-TFS test phases (**Suppl. figure 3**). This was achieved by setting transmitter release probability to zero for all longitudinal connections to distant sites, but only during two-site TFS. These connections were functional during the pre- and post-tests. Consistent with the interpretation put forward by Unal et al. (2012), inactivating long-range connections during two-site TFS eliminated the response potentiation normally elicited from the paired sites (Control, 32 ± 3% increase), and instead caused a response depression (-31 ± 4% decrease, paired t-test, $p < 0.001$). Responses elicited from the other neocortical stimulation sites did not change significantly (-0.2 ± 0.4 %, $p = 0.72$). Thus, inactivating long-range connections effectively made paired application of two-site TFS equivalent to single-site training (**Supplementary figure 3).**

S.9.2. Involvement of NMDA and group I mGluRs in activity-dependent plasticity

Next, we analyzed the dependence of the plasticity induced by TFS on NMDA and group I mGluR receptors (**Suppl. Figs. 4-5**). Unal et al. (2012) suggested that competition between NMDA receptor-mediated LTP and group I mGluR-dependent LTD had a determining influence on the outcomes of TFS. Indeed, they observed that while NMDA receptor blockade with AP5 during one-site TFS did not prevent the response depression, group I mGluR blockade with AIDA transformed the response depression into a potentiation. Conversely, while group I mGluR blockade during two-site TFS did not prevent the response potentiation, NMDA receptor blockade transformed the potentiation of responses into a depression.

The model could reproduce these experimental observations. When the action of group I mGluRs was blocked (**Suppl. Fig. 4A**; by setting v_{IP3}, a model parameter proportional to the degree of mGluR activation. to 0), TFS of neocortical inputs from site 5 mm, instead of causing a response depression, increased RS spiking to test stimuli applied at the induction site (increase of 23 ± 3%; p=0.0009), with little change in the response of RS cells to stimuli applied at the control sites (0.2 ± 0.2%, p = 0.82). In contrast, blocking NMDA receptors (**Suppl. Fig. 4A**) during one-site TFS (by setting $G_{NMDA} = 0$), increased the amount of depression induced by TFS application at one site (Control -39±4%; AP5, -62 ± 3%, p=0.001). Minimal changes were seen in the responses elicited by the control sites (-3 ± 1%; p =0.27).

The impact of NMDA or group I mGluR blockade on the potentiation seen following paired TFS at two neocortical sites (**Suppl. Fig. 4B**) was also consistent with the findings of Unal et al. (2012). When NMDA receptors were blocked during two-site TFS, this manipulation, instead of causing a response potentiation, decreased orthodromic spiking to test stimuli applied at the induction sites (-62 ± 2%; p = 0.0001), with much smaller changes in the responses elicited from the control neocortical sites (–3 ± 1%; **Suppl. Fig. 4B**). In contrast, blockade of group I mGluRs (by setting $v_{IP3} = 0$) produced an insignificant increase in the potentiation seen for the paired sites (37 ± 2%; **Suppl. Fig. 4B**) relative to the control case (32 ± 3%; p =0.057) with negligible changes in the responses elicited from the other neocortical sites (1 ± 1%; p =0.78).

S.10. Details related to evolution of the model

Single site training (performed only at the 5 mm site, as in Unal et al. 2012)

- Stimulation of a particular NC site causes the adjoining RS cells to spike once per NC spike. Inhibition in the system ensured that the PRC responses were transient and not sustained beyond 30-40 ms after NC stimulation. With just one spike/stimulation continued for 2-3 stimulations (the exact number depends on the # of NC connections to the RS cell), the calcium influx is sufficient to cause LTD of the NC-RS synapses. This is because activation of IP3 receptors requires a minimum amount of calcium via I_{CaL}. With just one spike over a period of say 400 ms, there is not enough calcium influx to cause LTD. In contrast, every RS cell spike does cause LTP in the NC-RS synapses, but the level is miniscule. However, with the second spike of the second stimulation of the theta burst, the LTD level is much higher than the resultant LTP, causing LTD to dominate. With successive trials, LTD causes some cells to stop spiking. Note that since long range connections are not active, an RS cell does not spike twice with one NC stimulation.
- Short-range RS-RS activity does not seem to play a major role, but it has not yet been investigated fully.

- During pre-tests we find that spikes at rostro-caudal locations other than the stimulated site are very rare. This means that the baseline long-range connection weights and connectivity cannot pesently cause a spike at locations beyond 1.5 mm of the cell.

<u>Paired site training (at 2 and 8 mm sites as in Unal et al. 2012)</u>

- Compared to the single site case, paired site stimulation results in considerably more activity at both the stimulated sites, and throughout the rostro-caudal axis. This is primarily due to long-range connections. Note that the growth in this activity occurs continuously through the training process. What causes this increase in activity?
- RS cells that receive sufficient NC connections (e.g., at the 2 mm site) fire once, typically 10-15 ms after NC stimulation. The membrane potential depolarization resulting from this spike lasts about 70-80 ms.
- If these RS cells also receive sufficient active long-range RS connections from the other site (e.g., 8 mm) they fire again after about 30 – 40 ms.
- The second RS cell spike coming about 30-40 ms after NC stimulation effectively doubles the duration of depolarization in these RS cells, resulting in increased influx of NMDAR calcium causing significantly larger LTP. In contrast, LTD is at the same level as in the single site case, for the second spike also. This differential expression of the growth mechanisms results in a net potentiation of the NC-RS connections.
- In parallel, due to the mechanisms discussed, RS-RS connections also potentiate. For these connections, the learning factors for LTP and LTD were adjusted so that it favored LTP (note that this is same as in single site case, i.e., the overall model has this consistently for all cases).

- With continued potentiation of both NC-RS and RS-RS connections at the two stimulated sites during the trials, several additional RS cells begin responding to NC stimulation.
- After paired site training, during tests at single sites, some cells near the stimulation site spike twice, if they receive enough NC and long-range connections. The first spike is due to input from NC and the second due to return of the signal after traveling to distant site via strong long range two-way connections. However, such spikes are few in number, compared to spikes of potentiated cells. Just an observation.

SOM+ cells which receive long-range connections cause termination of activity at all locations, typically 40 ms after NC stimulation."

S.11. SOM$^+$ cells are critical for containing activity

SOM$^+$ cells receive excitatory connections from long-range RS cells, and play a major role in terminating activity after paired site TFS by inhibiting RS cells in their vicinity. During paired site TFS, RS cells spike once due to NC input. If the same RS cells receives enough long-range connections, it will spike a second time after a delay of 10 to 15 ms. Since SOM$^+$ cells connected to this particular RS cell will also receive long-range inputs, the SOM$^+$ cells will also spike. Coming about 2 ms after arrival of long-range activity at the RS cell, this SOM$^+$ inhibition is unable to stop the second RS cell spike. However, this inhibition effectively counters any residual short- or long-range PSPs at the site after the second RS spike. Activity at the stimulated sites during paired site TFS lasts only for about 30 to 40 ms from NC stimulation due to inhibition by SOM. This SOM inhibition also ensures that the activity does not spread to other areas in the network, ensuring that the network does not have a tendency to 'run away'.

S.12. Model limitations

Our model is an approximation, admittedly imperfect, of area 36. First, it includes a much lower number of neurons than present in area 36. This reduction, needed to keep computation times practical, likely makes the model's behavior less graded and alters its dynamic range along many dimensions. Second, our model only includes PV and SOM interneurons, when others types are known to exist (Witter et al. 2000; Uva et al. 2004). Third, in the absence of relevant data in the perirhinal literature, short-term synaptic dynamics and interneuronal connectivity were based on findings obtained in different cortical areas. Fourth, for the same reason, connectivity estimates were based on the model's ability to reproduce synaptic responses described in prior perirhinal recordings, not on actual quantifications of axonal convergence and divergence. Fifth, model neurons do not exhibit the oscillatory activity known to be present in the perirhinal cortex (Collins et al. 1999). Nevertheless, the model could reproduce the findings of Unal et al. (2012). These include (1) the opposite polarity and contrasting pharmacological dependence of the plasticity induced by repeated activation of focal vs. distributed neocortical inputs, (2) the fact that no response potentiation develops when distant neocortical inputs are activated asynchronously, as well as (3) the observation that interrupting long-range connections during paired-site TFS transforms the response potentiation into a response depression. The model's ability to reproduce these findings suggests that despite its shortcomings, it captures critical aspects of the perirhinal network.

S.13. Supplementary Tables

Table S1. Kinetics of Hodgkin-Huxley type currents. V is specified in mV, [Ca2+] is specified in µm. ICa,L was calculated as $I_{Ca,L} = G_{Ca,L} \times Dif \times m^2 h$, where Dif accounts for the reversal potential of calcium.

I_{ion}	x^p	α (msec^{-1})	β (msec^{-1})	x_∞	τ_x (msec)
I_{Kd}	m^3	$\frac{-0.00612(V+2)}{\exp(-(V+2)/20)-1}$	$\frac{0.00184(V-8)}{\exp((V-8)/12)-1}$	$\alpha/(\alpha+\beta)$	$1/(\alpha+\beta)$
I_{A}	m^3	—	—	$\frac{1}{1+\exp(-(V+46.9)/14.1)}$	$0.3+0.2\exp(-V/27)$
	h	—	—	$\frac{1}{1+\exp((V+79.1)/9.3)}$	$14+\exp(V/30)$
I_{C}	m^2	$\frac{-0.00642V_m-0.1152}{\exp(-(V_m+18)/12)-1}$	$1.7\exp(-(V_m+152)/30)$ $V_m = V+40\log_{10}([Ca^{2+}])$	$\alpha/(\alpha+\beta)$	$1/(\alpha+\beta)$
I_{AHP}	m^2	$13\times[Ca]^4$	0.005	$\alpha/(\alpha+\beta)$	$1/(\alpha+\beta)$
$I_{\text{H,s}}$	m	—	—	$\frac{1}{1+\exp((V+72.83)/15.9)^{58.5}}$	$\frac{5.6}{\exp((V-17)/14)+\exp(-(V+260)/43)}$
$I_{\text{H,f}}$	m	—	—	$\frac{1}{1+\exp((V+74.2)/9.78)^{1.36}}$	$\frac{0.51}{\exp((V-1.7)/10)+\exp(-(V+340)/52)}$
$I_{\text{Ca,L}}$	m^2	$\frac{-15.69(V-81.5)}{\exp(-(V-81.5)/10)-1}$	$0.29\exp(-V/10.86)$	$\alpha/(\alpha+\beta)$	$\tau_{Ca,L}$
	h	—	—	$1/(1+[Ca^{2+}])$	*instantaneous*
I_{Na}	m^3	$\frac{-0.2816\times(V+25)}{\exp((V+25)/9.3)-1}$	$\frac{0.2464\times(V-2)}{\exp((V-2)/6)-1}$	$\alpha/(\alpha+\beta)$	$1/(\alpha+\beta)$
	h	$0.098\exp(-(V+40.1)/20)$	$\frac{1.4}{\exp(-(V+10.1)/10)+1}$	$\alpha/(\alpha+\beta)$	$1/(\alpha+\beta)$
Dif		$-13.012\times\left(1-\frac{[\text{Ca}^{2+}]}{[\text{Ca}^{2+}]_{\text{ext}}}\exp(-\text{V}/13.012)\right)\times\frac{-\text{V}/13.012}{\exp(-\text{V}/13.012)-1}$			
$\tau_{Ca,L}$		$\max\left(\frac{\exp(0.0756(\text{V}+25))}{0.385\times(1+\exp(0.00756(\text{V}+25)))},\ 0.065\right)$			

Table S2. Mathematical details of parameters used to implement synaptic plasticity.

Primary Variable	**Equations**
$[Ca^{2+}]_{\text{NMDAR}}$	$J_{NMDA} = -F_{NMDA} G_{NMDA} S(V)(B_N - A_N)(V - E_{Ca})$ $J_{eq} = \frac{\upsilon_{eq}[Ca^{2+}]^4_{rest}}{[Ca^{2+}]^4_{rest} + K^4_{eq}}$ $J_{PMCA,N} = \frac{\upsilon_P[Ca^{2+}]^4_{NMDA}}{[Ca^{2+}]^4_{NMDA} + K^4_P}$ $J_{NCX,N} = \frac{\upsilon_N[Ca^{2+}]^2_{NMDA}}{[Ca^{2+}]^2_{NMDA} + K^2_N}$
$[Ca^{2+}]_{\text{mGluR}}$	$J_{in} = a(J_{VGCC} + J_{SOC})$ $J_{out} = b(J_{PMCA,M} + J_{NCX,M})$ $J_{VGCC} = -F_{mGluR} I_{Ca,L}$ $J_{SERCA} = \frac{\upsilon_{SERCA}[Ca^{2+}]^2_{mGluR}}{[Ca^{2+}]^2_{mGlUR} + K^2_{SERCA}}$ $J_{PMCA,M} = \frac{\upsilon_P[Ca^{2+}]^4_{mGluR}}{[Ca^{2+}]^4_{mGluR} + K^4_P}$ $J_{NCX,M} = \frac{\upsilon_N[Ca^{2+}]^2_{mGluR}}{[Ca^{2+}]^2_{mGlUR} + K^2_N}$ $J_{SOC} = -\frac{\upsilon_{SOC} K^4_{SOC}}{[Ca^{2+}]^4_{ER} + K^4_{SOC}}(V - E_{Ca})$
J_{IP3R}	$\tau_m([Ca^{2+}]_{mGluR})\frac{dm}{dt} = -m + m_\infty([IP_3],[Ca^{2+}]_{mGluR})$ $\tau_h([IP_3],[Ca^{2+}]_{mGluR})\frac{dh}{dt} = -h + h_\infty([IP_3],[Ca^{2+}]_{mGluR})$ $m_\infty([IP_3],[Ca^{2+}]_{mGluR}) = \left(\frac{[IP_3]}{[IP_3] + d_{IP3}}\right)\left(\frac{[Ca^{2+}]_{mGluR}}{[Ca^{2+}]_{mGluR} + d_{act}}\right)$ $h_\infty([IP_3],[Ca^{2+}]_{mGluR}) = \frac{Q([IP_3])}{Q([IP_3]) + [Ca^{2+}]_{mGluR}}$ $\tau_m([Ca^{2+}]_{mGluR}) = (b_{IP3} + a_{IP3}[Ca^{2+}]_{mGluR})^{-1}$ $\tau_h([IP_3],[Ca^{2+}]_{mGluR}) = \left(a_{inh}(Q([IP_3]) + [Ca^{2+}]_{mGluR})\right)^{-1}$ $Q([IP_3]) = d_{inh}\frac{[IP_3] + d_{IP3}}{[IP_3] + d_{dis}}$

Table S3. Parameters valued used in the synaptic plasticity equations.

Eq. Family	Parameters			
I_{AMPA}	G_{AMPA} = 1 nS	Cdur_ampa = 1.421 ms	β_ampa = 0.1429 ms^{-1}	
	E_{AMPA} = 0 mV	αTmax_ampa = 3.8142 ms^{-1}		
I_{NMDA}	G_{NMDA} = Eq. S13,S14	Cdur_nmda= 16.765 ms	β_ampa = 0.008 ms^{-1}	
	E_{NMDA} = 0 mV	αTmax_nmda = 0.2659 ms^{-1}		
I_{GABAa}	G_{GABAa} = 100 nS	τ_1 = 2 msec		
	E_{GABAa} = -75 mV,	τ_2 = 25 msec	τ_D = 250 msec	
I_{GABAb}	G_{GABAb} = 2 nS	τ_1 = 50 msec		
	E_{GABAb} = -92 mV	τ_2 = 500 msec	τ_D = 250 msec	
$dW_{i,j}/dt$	NC→RS:	λ_1 = 2 μM	λ_2 = 0.1 μM	λ_3 = 0.5 μM
	RS→RS:	λ_1 = 9 μM	λ_2 = 0.005 μM	λ_3 = 0.25 μM
	θ_d = 0.7 μM	θ_p = 0.5 μM	θ_m = 1.5 μM	
$[Ca^{2+}]_{\mathrm{NMDAR}}$	F_{NMDA} = 0.14 μM/nA-msec	$[Ca^{2+}]_{\mathrm{rest}}$ = 0.05 μM		
	v_{eq} = 0.1 μM/msec	v_n = 0.04 μM/msec	v_p = 0.04 μM/msec,	
	K_{eq} = 0.1 μM	K_n = 1.0 μM	K_p = 0.1 μM	
$[Ca^{2+}]_{\mathrm{mGluR}}$	F_β = 0.0095 mM/nA-msec	F_{cyt} = 0.002809 pL^{-1}		
	a = 0.00412*	b = 1*	F_{mGluR} = 6 x 10^5 mM-cm^2/nA-msec	
	v_{soc} = 0.03 mM/msec	v_p = 0.04 mM/msec	v_n = 0.04 mM/msec	v_S = 13 mM/msec
	K_{soc} = 100 mM	K_p = 0.1 mM	K_n = 1.0 mM	K_S = 0.2 mM
$IP_3 \rightarrow [Ca^{2+}]_{ER} \leftrightarrow [Ca^{2+}]_{\mathrm{mGluR}}$	v_R = 15 pL/msec	v_L = 0.0021 pL/msec	F_{ER} = 0.015873 pL^{-1}	
	a_{inh} = 0.005 $(\mu\mathrm{M\text{-}msec})^{-1}$	a_{IP3} = 0.42 $(\mu\mathrm{M\text{-}msec})^{-1}$	d_{inh} = 0.525 μM,	
	d_{IP3} = 0.13 μM	b_{IP3} = 0.0001msec^{-1}	d_{act} = 0.6 μM	d_{dis} = 0.47 μM
	v_{IP3} = 0.25 μM/msec	τ_1 = 100 msec	τ_2 = 400 msec	
Initial Weights*	NC → RS = 1.15; NC → PV= 0.35; RS → RS (Short) = 1;RS → RS (Long) = 1.2 RS → PV = 0.08;RS → SOM^+ = 0.75;PV → RS = 0.05;SOM^+ → RS = 0.025;SOM^+ → PV = 0.15			

*Parameter is unitless.

S.14 Supplementary Figures

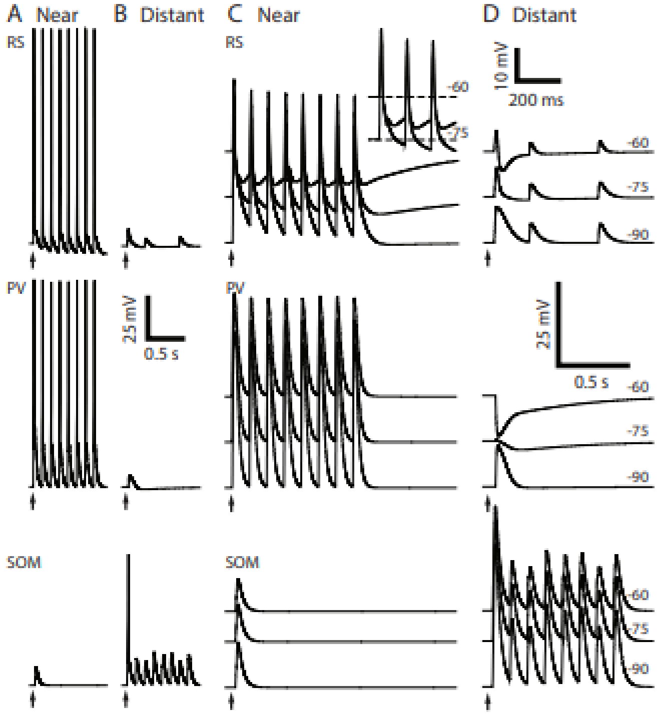

Suppl. Figure 1. Response of model neurons to train of neocortical stimuli applied at nearby and distant neocortical sites. (A,C) Nearby neocortical stimuli. (B,D) Distant neocortical stimuli. Top to Bottom: principal regular spiking (RS) neuron, parvalbumin (PV) interneuron, somatostatin (SOM) interneuron. (A,B) Train of neocortical stimuli applied while neurons were at rest. (C,D) Train of neocortical stimuli applied while the membrane potential of the cells was set to -60, -75, or -90 mV by simulated direct current injection. In C and D, the voltage-dependent Na+ conductance was set to zero so that synaptic responses could be examined without the contaminating influence of spikes and afterhyperpolarizations. Inset at top of C: expanded depiction of RS responses to nearby neocortical stimuli (first three stimuli).

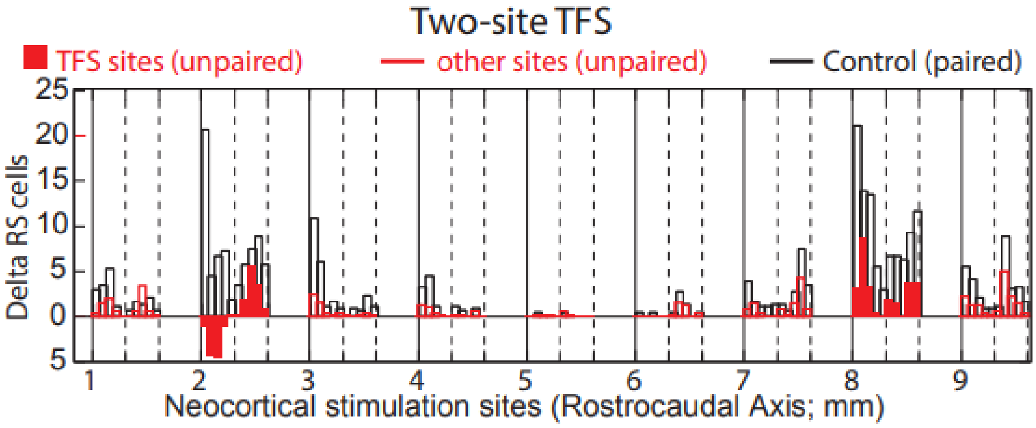

Suppl. Figure 2. Potentiation induced by two-site TFS depends on input synchrony. (A) Difference in the number of RS cells spiking (y-axis) in response to neocortical stimuli (x-axis) applied before vs. after two-site TFS. During TFS, neocortical stimuli were either applied simultaneously (black lines) or separated by half a theta cycle (65 ms, red) at sites 2 and 8.

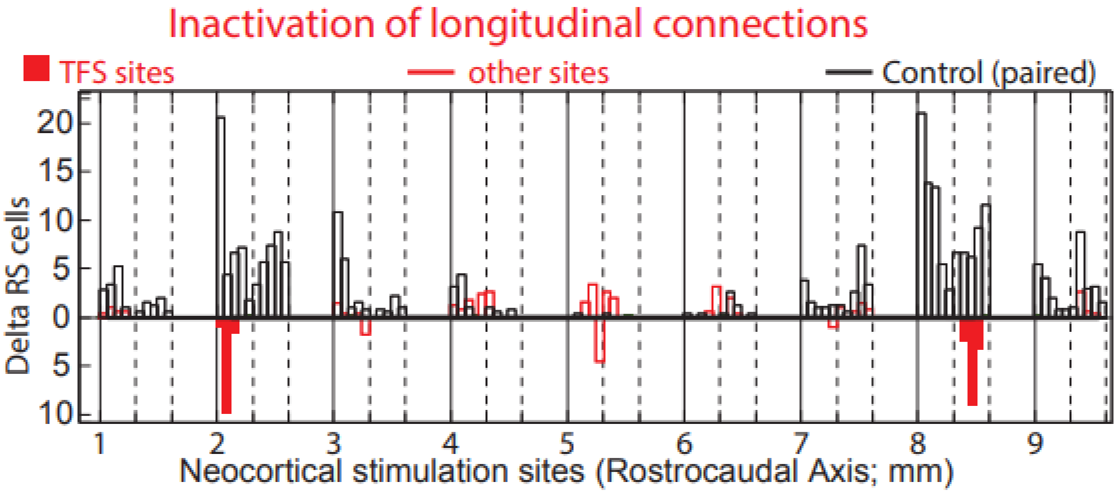

Suppl. Figure 3. Potentiation induced by two-site TFS depends on recruitment of longitudinal connections. Difference in the number of RS cells spiking (y-axis) in response to neocortical stimuli (x-axis) applied before vs. after two-site TFS. Two-site TFS was either applied with all connections functional (black) or with the weight of long-range connections set to zero (red; only during TFS).

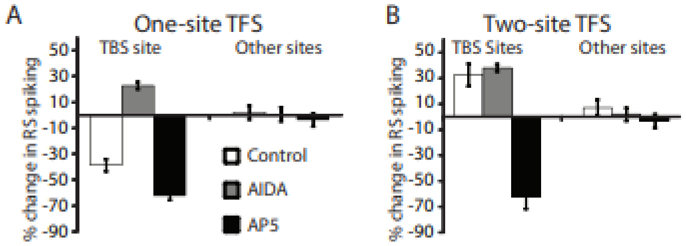

Suppl. Figure 4. Dependence of activity-dependent plasticity on the activation of NMDA and group I mGluRs. Percent change in the number of RS cells spiking in response to neocortical stimuli applied before vs. after TFS at one (**A**) vs. two (**B**) neocortical sites in control conditions (empty bars), and after simulating pharmacological block of group I mGluRs (gray bars) or NMDA receptors (black bars). The left and right bar clusters show data elicited from the TFS or control sites, respectively.

S.15. References

Aslam N, Kubota Y, Wells D, Shouval HZ (2009) Translational switch for long-term maintenance of synaptic plasticity. Mol Syst Biol 5.

Blackwell KT (2005) Modeling calcium concentration and biochemical reactions. Brains, Minds and Media 1:bmm224.

Byrne JH, Roberts JL (2004) From Molecules to Networks – An introduction to cellular and molecular neuroscience. Elsevier Academic Press.

Carnevale NT, Hines ML (2006) The NEURON book. Cambridge, UK: Cambridge University Press.

Castellani GC, Bazzani A, Cooper LN (2009) Toward a microscopic model of bidirectional synaptic plasticity. Proceedings of the National Academy of Sciences.

Castellani GC, Quinlan EM, Cooper LN, Shouval HZ (2001) A biophysical model of bidirectional synaptic plasticity: Dependence on AMPA and NMDA receptors. Proc Natl Acad Sci USA 98:12772-12777.

Castellani GC, Quinlan EM, Bersani F, Cooper LN, Shouval HZ (2005) A model of bidirectional synaptic plasticity: From signaling network to channel conductance. Learn Mem 12:423-432.

De Young GW, Keizer J (1992) A single-pool inositol 1,4,5-trisphosphate-receptor-based model for agonist-stimulated oscillations in Ca2+ concentration. Proceedings of the National Academy of Sciences 89:9895-9899.

Durstewitz D, Seamans JK, Sejnowski TJ (2000) Dopamine-mediated stabilization of delay-period activity in a network model of prefrontal cortex. J Neurophysiol 83:1733-1750.

Fletcher PA, Li Y-X (2009) An integrated model of electrical spiking, bursting, and calcium oscillations in GnRH neurons. Biophys J 96:4514-4524.

Hummos A, Franklin CC, Nair SS (2014) Intrinsic mechanisms stabilize encoding and retrieval circuits differentially in a hippocampal network model. Hippocampus 24:1430–1448.

Kim D, Pare D, Nair SS (2013) Mechanisms contributing to the induction and storage of Pavlovian fear memories in the lateral amygdala. Learn Mem 20:421-430.

Koch C, Segev I (eds.) (1989) Methods in neuronal modeling: From synapses to networks: MIT Press.

Krieger P, Hellgren-Kotaleski J, Kettunen P, El Manira AJ (2000) Interaction between metabrotopic and ionotropic glutamate receptors regulates neuronal network activity. J Neurosci 20:5382-5391.

Li G, Nair S, and Quirk GJ (2009) A biologically realistic network model of acquisition and extinction of conditioned fear associations in lateral amygdala neurons. J Neurophysiol 101:1629-1646.

Li G, Amano T, Pare D, Nair SS (2011) Impact of infralimbic inputs on intercalated amygdala neurons: a biophysical modeling study. Learning & Memory 18:226-240

Li Y-X, Rinzel J (1994) Equations for InsP3 receptor-mediated [Ca2+]i oscillations derived from a detailed kinetic model: A hodgkin-huxley like formalism. J Theor Biol 166:461-473.

Li YX, Rinzel J, Keizer J, Stojilković SS (1994) Calcium oscillations in pituitary gonadotrophs: Comparison of experiment and theory. Proceedings of the National Academy of Sciences 91:58-62.

Li YX, Stojilković SS, Keizer J, Rinzel J (1997) Sensing and refilling calcium stores in an excitable cell. Biophys J 72:1080-1091.

Martina M, Royer S, Pare D (2001a) Cell-type-specific GABA responses and chloride homeostasis in the cortex and amygdala. J Neurophysiol 86:2887-2895

Martina M, Royer S, Pare D (2001b) Propagation of neocortical inputs in the perirhinal cortex. J Neurosci 21:2878-2888.

Shouval HZ, Bear MF, Cooper LN (2002a) A unified model of NMDA receptor-dependent bidirectional synaptic plasticity. Proc Natl Acad Sci U S A 99:10831-10836.

Shouval HZ, Castellani GC, Blais BS, Yeung LC, Cooper LN (2002b) Converging evidence for a simplified biophysical model of synaptic plasticity. Biol Cybern 87:383-391.

Shouval HZ, Wang SS-H, Wittenberg GM (2010) Spike timing dependent plasticity: A consequence of more fundamental learning rules. Frontiers in Computational Neuroscience 4.

Varela J, Sen K, Gibson J, Fost J, Abbott L, Nelson S (1997) A quantitative description of short-term plasticity at excitatory synapses in layer 2/3 of rat primary visual cortex. J Neurosci 17:7926–7940.

Yeung LC, Castellani GC, Shouval HZ (2004) Analysis of the intraspinal calcium dynamics and its implications for the plasticity of spiking neurons. Physical Review E 69:011907.

CHAPTER 3

INTRINSIC AND GAP JUNCTION COMPENSATION TO PRESERVE SINGLE CELL AND NETWORK PROPERTIES: A COMPUTATIONAL MODEL STUDY OF LC OF CRAB

3.1 BACKGROUND

What computer controls heartbeat of single muscle crab heart?

How do groups of neurons maintain synchrony to drive the muscle?

If this rhythm is disturbed due to injury, these group of neurons automatically regain the synchronous rhythm after time.

How does this compensation occur to restore electrical activity in neurons?

Engineering relevance: a) Robustness of system.

b) Non-linear electrical system.

c) Compensation mechanisms.

3.2 ABSTRACT

The crustacean cardiac ganglion (CG) network coordinates the rhythmic contractions of the heart muscle to control the circulation of blood. The network consists of 9 cells, 5 large motor cells (LCs) and 4 small endogenous pacemaker cells (SCs). Previous studies have looked into homeostatic compensation at either cellular or network levels, but not at both levels for the same preparation. There is variability in the intrinsic conductance for the five LCs in the cardiac network. In spite of this variability, they have synchronous output in the intact network. Our main objective is to understand how cells with different intrinsic make up work together to maintain the cardiac rhythm of cancer borealis. Here we first develop a single cell model using first-hand recordings of intrinsic currents from LC of crab and then develop the complete five

LC model to study the network dynamics. On a network level, model shows how intrinsic vs gap junction coupling compensation can help maintain the synchrony in the network**.**

3.3 INTRODUCTION

Neurons are endowed with a rich and complex set of intrinsic and synaptic conductances that control its electrical activity (Marder 2011; Prinz et al. 2004). Although the role of such a varied set of conductances is not fully understood, it is natural to expect that neurons of the same cell type would possess similar membrane properties, especially within the same animal. However, experimental findings are beginning to reveal that maximal conductance levels can vary two- to six-fold among same cell types (Goaillard et al. 2009; McLean et al. 2005; Khorkova and Golowasch 2007; Schulz et al., 2007, 2006) and that different combinations of conductances preserve activity at the single cell level (Swensen and Bean 2005; Marder et al. 2006; Nerbonne et al. 2008). Also, different sets of ionic conductances (Khorkova and Golowasch, 2007) and ion channel mRNA levels (Schulz et al., 2007; Tobin et al., 2009) can be correlated with one another in different classes of identified neurons, suggesting an on-going, rather than developmentally fixed, regulation of specific sets of conductances. These findings were from investigations related to the robustness of cellular output, either via artificial perturbation of a single conductance or injury (McLean et al. 2005; Swensen and Bean 2005; Marder and Goaillard 2006; Nerbonne et al. 2008; McLean et al. 2003). Would such a variation in intrinsic properties also exist in the unperturbed native network? Although computational models have predicted this possibility, only recently has it been shown experimentally that intrinsic membrane properties of individual neurons do indeed vary widely among neurons of the same cell type even, within networks in their natural state (Ransdell et al., 2012).

Computational modeling has revealed that exclusive reliance of mean data may be misleading (Golowash et al. 2002), and that populations of model neurons need to be developed to capture the biological variability in underlying properties (Marder et al., 2007). Concurrent with experiments, such computational models have continued to explore potential roles of the different conductances in conserving cellular output such as spike and burst characteristics (Goldman et al. 2001; Prinz et al. 2003, 2004; Tobin and Calabrese 2006; Olypher and Calabrese 2007; Gunay et al. 2008; Marder Taylor et al. 2009; Ball et al. 2010; Franklin et al. 2010; Olypher and Prinz 2010). For instance, Prinz et al. (2003) explored the maximal conductance space of a single-compartment model neuron to quantify the numerous types of spiking and bursting models and showed that similar patterns of activity could be produced by many different parameter sets, both for single neurons (Prinz et al., 2003) and within small networks (Prinz et al., 2004). An interesting study using a multicompartment model of a lateral pyloric neuron recently suggested that correlated levels of multiple conductances are not necessary to maintain output (Taylor et al., 2009).

Ball et. al. (2010) developed a model for the large cell (LC) of the cardiac ganglion of the crab *Portunus sanguinolentus* and used it to predict that coregulation of two currents could preserve key characteristics of motor neuron activity, the duration and peak of the excursion of the synaptically driven regenerative membrane potential above its resting value. Such an underlying oscillation determines the number of spikes per burst for such cells, which in turn affects outputs downstream, such as muscle actuation. Franklin et al. (2010) generalized the finding by showing that the coregulation did hold for underlying oscillations in bursting cells in general by considering the same large cell of portunus, an anterior burster cell of the crab stomato-gastric ganglion (STG) and an aplysia R15 cell. Furthermore, the model helped hypothesize three phases associated with the underlying oscillation: generation, maintenance, and termination, and provided testable predictions about potential current "modules" involved in maintaining the robustness of the underlying oscillation. Due to lack of data, as happens with typical neuronal models, parameters for the Portunus LC currents in the models cited were borrowed from the STG literature (Prinz et al. 2003). In the present study, we study a different crab species *Cancer borealis* and develop a model for its LC from first hand biological data from our Lab. The model is then used to study the features of its underlying oscillation, using for the first time a model of the LC informed completely by measured properties of the same cell. This integrated experimental-computational approach is used to investigate how intrinsic properties might shape the underlying oscillation for the cancer LC, using a multi-dimensional parameter search. The model was then used to reverse engineer the experimentally discovered phenomenon in the Schulz Lab where network synchrony among LCs that is lost after application of TEA, is recovered after passage of time (about 1 hour) by intrinsic compensation among the LC current channels. This compensation is supposed to involve mechanisms at both single cell and network levels, and the model is used investigate their relative contributions in maintaining synchrony.

3.4 METHODS

Detailed Model

A detailed model was created with all 8 active channels and a passive leak channel. A single compartment model with biological dimensions for soma was created in NEURON and its Capacitance (Cm) and Leak Conductance (G_{leak}) were tuned to match the observed biological membrane time constant (τ) and input resistance (R_{in}). After addition of 9 channels, their maximal conductances were tuned to match three biological properties observed i.e. a) Total outward current b) Response to synaptic drive and c) Response to synaptic drive in presence of TEA. All these three results were obtained by performing the experiments on ligatured soma of LC of Cancer Borealis by Schulz Lab. For the network studies another compartment for Spike Initiation Zone (SIZ) was added to the model. This compartment consisted of only 3 channels, sodium, potassium and a passive leak channel.

$$C\,\frac{dV}{dt} = -I_A - I_{Kd2} - I_{Nap} - I_{CaPQ} - I_{Cal} - I_{CAN} - I_{SKKCa} - I_{BKKCa} - I_{Leak} + I_{inj} \quad \text{(Soma)}$$

$$C\,\frac{dV}{dt} = -I_{Na} - I_{Kdr} - I_{Leak} + I_{inj} \quad \text{(SIZ)} \qquad (1)$$

The 8 active channels installed in soma were fitted using biological measurements for these currents in cardiac ganglion of cancer borealis. These currents were fitted in following way: Voltage clamp data obtained with Clampfit were imported into MATLAB and fit using the MATLAB curve-fitting toolbox. Current data was converted to conductance data by dividing by (V_m – E_{rev}), where Erev was assumed to be -60 mV for K+ currents, +55 mV for Na+ currents, and +45 mV for Ca2+ currents. The time data obtained was converted from sec to msec by multiplying it with 1000. Also the time axis was adjusted to start from 0 for the beginning of the clamp .The obtained conductance data was fitted using Eq. 2. In this equation, $\mathbf{A_i} = \mathbf{G_{i,max}} \times \mathbf{m_i}$ was the maximal conductance of the current i multiplied by its voltage-dependent steady-state activation (m_i), h_i was the steady-state inactivation value, and $\tau_{m,i}$ and $\tau_{h,i}$ were the time constants with which activation and inactivation reached steady-state, respectively. This fitting procedure assumed that ion currents were completely deactivated m=0 and deinactivated (h=1) prior to the onset of the voltage clamp.

$$\boldsymbol{g(t) = \sum_{i=1}^{n} A_i \left(1 - \exp\left({}^{-t}/_{\tau_{m,i}}\right)\right)\left(h_i - (h_i - 1)\exp\left({}^{-t}/_{\tau_{h,i}}\right)\right)} \tag{2}$$

Equation 2 was fit to each trace in voltage clamp experiment, giving values of each of the four parameters for each test clamp voltage (V_c). These values were then fit for each current as functions of V_c using the general forms of Eq. 3. This procedure yielded equations for the currents recorded in voltage clamp that could be used in simulations according to the Hodgkin-Huxley mathematical formalism.

$$\boldsymbol{A(V_c) = G_{max} \times m(V_c) = G_{max} \times \left(1 + \exp\left(\left(V_c - V_{m,1/2}\right)/k_m\right)\right)^{-1}}$$
$$\boldsymbol{h(V_c) = \left(1 + \exp\left(\left(V_c - V_{h,1/2}\right)/k_h\right)\right)^{-1}}$$
$$\boldsymbol{\tau_m(V_c) = \tau_{base,m} + \tau_{amp,m}\left(\exp\left(\left(V_c - V_{\tau1,m}\right)/k_{\tau1,m}\right) + \exp\left(\left(V_c - V_{\tau2,m}\right)/k_{\tau2,m}\right)\right)^{-1}}$$
$$\boldsymbol{\tau_h(V_c) = \tau_{base,h} + \tau_{amp,h}\left(\exp\left(\left(V_c - V_{\tau1,h}\right)/k_{\tau1,h}\right) + \exp\left(\left(V_c - V_{\tau2,h}\right)/k_{\tau2,h}\right)\right)^{-1}}$$

All the maximal counductances ($G_{i,max}$) were in µS, Time Constants in ms and Voltages in mV.

Calcium Dynamics

Intracellular calcium modulates the conductance of the calcium-activated potassium currents (BKKCa and SKKCa), calcium-activated nonselective cation current (CAN), and influences the magnitude of the inward calcium current in the LC (Tazaki and Cooke, 1990). A calcium pool was modeled in the LC with its concentration governed by the first-order dynamics (Prinz et al., 2003; Soto-Treviño et al., 2005) below:

$$\tau_{Ca}\frac{d[Ca^{2+}]}{dt} = -F \times I_{Ca} - ([Ca^{2+}] - [Ca^{2+}]_{rest})$$

where F = 0.256 μM/nA is the constant specifying the amount of calcium influx that results per unit (nanoampere) inward calcium current; τCa represents the calcium removal rate from the pool; and [Ca2+]rest = 0.5 μM. Voltage-clamp experiments of the calcium current (Ransdell et al., 2013b) showed the calcium buffering time constant to be around 690 ms (τCa).

Searching for LC Neurons within the Model Parameter Space

After creating a nominal LC model (**Tables 1,2**), we wanted to search the conductance space for other possible conductance combinations that might exhibit appropriate LC output. The properties that had to be maintained were; a) Input Resistance (Rin) and Resting Membrane Potential, b) Pre-TEA and Post TEA response to current injection c) Response to Synaptic drive obtained from biological cell.

The rules used to select the potential parameters were as follows (based on biological recordings): Synaptic Drive response should have an R2 value of at least 0.8 or higher when compared to biological Synaptic Drive response. The duration of the pre-TEA response to a 6 nA, 50 ms current injection should be less than 120 ms. Also the peak should be less than -22 mV. The duration of the post-TEA (GBKKCa and GKd reduced by 90%) response should be between 255-667 ms and its peak should be greater than -15 mV. A 9-D max conductance parameter space (5-fold variation over each conductance except GLeak) was searched randomly for sets that satisfied the constraints above. We searched 20,000 different combinations of parameter sets with these criteria, and most of those which passed did not have a proper termination of activity following current injection (i.e., did not return to Vrest). We concluded this was due to an inappropriate relationship between ICAN and ISKKCa. Subsequent trials revealed that a given ratio range (~1:0.83 respectively) of these two currents was necessary for proper termination of activity. Larger ratios cause Vrest to be higher due to the reversal potential (-30 mV) of CAN current. A higher fraction of ISKKCa (reversal potential -80mV) caused a large AHP after termination and reduced the duration of the post-TEA response. Using the updated selection criteria with a ratio ICAN to ISKKCa, we found 180 parameter sets that passed. Of these 180 potential model sets, we selected only the ones that had Synaptic Drive response R2 value > 0.9 compared to the biological Synaptic Drive response. This resulted in 49 potential parameter sets.

Biological data showed that IA and IBKKCa had a negative correlation in their magnitudes in LCs (Ransdell et al., 2012). We added this to our criteria for screening potential parameter sets for the network studies. We converted biological IA-IBKKCa current data into factor data by dividing IA and IBKKCa by their respective factor average. GA and GBKKCa values of passed parameters were similarly divided by its average to get its factor data. The biological data was fit using a linear polynomial from 95% to 70% confidence intervals, in steps of 10%. For network studies we used a 70% confidence interval, which left us with 14 potential parameter sets that represented LC model neurons for use in modeling studies.

Development and Validation of a Population of Conductance-Based Model Networks for Studying Mechanisms Restoring Network Synchrony

Our results demonstrate that intact cardiac ganglia are able to compensate for the loss of high-threshold K+ currents and restore both excitability and synchrony within one hour of TEA blockade. We next set out to explore the mechanisms by which excitability and synchrony could be restored in this network. To maximize our ability to interrogate multiple parameters that may be responsible for compensation in this system, we constructed a population of conductance-based biophysical models of the CG network. This allowed us to simulate the TEA conductance blockade and then manipulate individual conductances, both voltage-gated and synaptic, to examine their effects on network excitability and synchrony.

Our 14 parameter sets for LCs were used to create 50 random 5-cell networks of LCs, ensuring that the same model LC never appeared twice in the same network. The five cells within a network were then electrically coupled using conductance values tuned to reflect experimental observations of coupling coefficients. Small cell (SC) pacemaker drive was simulated as excitatory synapses via the NetStim function in NEURON. Parameters for the model of the synaptic drive onto LCs were tuned to get 6 to 9 spikes in the nominal LC model. It was observed biologically that frequency of SC firing increases within the slow wave oscillation cycle of LCs. Based on these recordings, the model SC burst initially fired at 18 Hz for first 440 ms and then increased to 25 Hz for 560 ms, with the burst terminating at 1000 ms.

Our experimental TEA block was simulated in these networks by reducing GBKKCa and GKd conductances by 90% in the 3 anterior LCs (Ransdell et al., 2013a). We imposed a final set of selection criteria on the randomly generated model networks, rejecting networks that increased synchrony or decreased the total number of spikes after the simulated TEA block, as this was never observed in biological networks. This left 27 networks that reproduced the biological trends and these were used in subsequent analyses to explore potential conductance changes that could restore network synchrony.

Somatic burst potentials drive action potentials in LC axons, so divergent burst waveforms would be expected to cause desynchronized spiking. Our biological data qualitatively agreed with this, but a precise quantification of synchrony for all spikes within a burst is subject to many ambiguities. Our model networks easily provided precise spike times for each cell in the network, so we chose to examine actual spike synchrony in the model to complement the burst waveform analysis in the biological preparation. Our analysis considered synchrony for paired anterior LCs with a nominal coupling conductance of 0.0182 S using a 25 ms bin width for spike-times (Wang and Buzsáki, 1996). Spikes occurring in both cells during the same bin were considered synchronized, while spikes that did not bin together were tallied as desynchronized. Using this metric, these randomly generated model networks exhibited "control" synchrony scores ranging from 0.642 to 1.000 with a median value of 0.915, where 1.000 represents perfect spike synchrony.

Calculating Synchrony for Network models

In the models, synchrony between two cells was calculated based on spike times (Wang and Buzsáki, 1996). Spike times were recorded from each LC's Spike Initiation Zone (SIZ). The simulation time was divided into 25 ms bins. After initializing all bins to zero, each cell spike was added to the corresponding bin. Synchrony (SY) between two cells A and B was calculated using following equation:

$$SY_{AB} = \frac{\sum_{l=1}^{k} A(l) * B(l)}{\sqrt{\sum_{l=1}^{k} A(l) * \sum_{l=1}^{k} B(l)}}$$

where l is the current bin and k is the maximum number of bins. Spikes occurring in both cells during the same bin were considered synchronized, while spikes that did not bin together were tallied as desynchronized. Using this metric, these randomly generated model networks exhibited “control” synchrony scores ranging from 0.642 to 1.000 with a median value of 0.915, where 1.000 represents perfect spike synchrony.

3.5 RESULTS

Model Predicts Multiple Mechanisms of Compensation based on Intrinsic Conductances

TEA exposure reduces LC synchrony and induces hyperexcitability. Our model development and selection criteria resulted in a population of 27 model CG networks with variable underlying conductances of the constituent neurons that successfully recapitulated the biological data observed in TEA (see Methods, Supplemental Information). Our previous results identified an approximate 2.2 ± 0.8-fold change in IA in LCs as a result of 60 minutes of TEA exposure (Ransdell et al. 2012). Therefore, we used the model networks to explore potential mechanisms of compensation by first increasing and decreasing each individual maximal membrane conductance by a similar factor of 2. We searched for changes that would increase LC spike synchrony while countering the hyperexcitability induced by TEA. To easily visualize the trends, each network was normalized to its initial value for spike synchrony. These data are shown for all conductances in **Figure 1**.

Our initial goal with the model was to determine whether changes in single conductances were sufficient to elicit compensatory changes in output that help restore both excitability and synchrony. While it is not difficult to conceive of a change in multiple aspects of the parameter set that could achieve restoration of output, it is perhaps not as intuitive – but presumably the most parsimonious solution – for a single conductance to have such an impact. True to this expectation, while various manipulations of Gmax values improved either excitability or synchrony, very few conductance changes improved both. The optimal solution of significantly improving spike synchrony and also decreasing the total number of action potentials was achieved in only one case: 2-fold increase in GA resulted in a mean synchrony score that was significantly different from the TEA case ($P < 0.05$, paired t-test) but not significantly different from control ($P = 0.157$). Not every model cell or networked improved uniformly with this conductance change. Therefore, while these results do not rule out a contribution for other conductances, they do suggest that an increase in GA, as seen in previous experimental studies on isolated LCs (Ransdell et al., 2012), may be the most likely candidate for a change in intrinsic conductance promoting synchrony at the network level. These data suggest that while a single conductance change (increased GA) can help restore both excitability and synchrony, variations in a single voltage-dependent conductance may not be sufficient to account for the full compensation response. In addition to perturbing only individual conductances, we also varied current kinetics and activation parameters (half-activation voltage V1/2, +/- 10 mV, and slope factor k, by 0.5 and 2 (Ballo et al., 2012) and time constant by +/10 ms) for all the cell currents individually, and found that no changes in parameters for a single current could simultaneously restore excitability at the single cell level, and synchrony at the network level (data not shown). While the analysis has focused only on the parameters of a single current, simultaneous changes in parameters of multiple currents could also potentially provide similar compensation, and that remains to be explored. However, our analysis does reveal the substantial contribution of changing a single parameter – GA – on multiple aspects of network compensation, to an extent that is beyond simple intuition. Importantly, the model also extends the biological data by demonstrating that waveform synchrony can translate into spike synchrony. Because of the electrotonic distance between the somata and axons of LCs, we cannot measure spike synchrony directly in this preparation. The model allows us to infer that waveform synchrony (and loss of synchrony) can indeed translate to the level of the most proximal cellular output – spiking.

Increased Electrical Synaptic Conductance Helps Restore Synchrony

If intrinsic compensation does not fully restore synchrony, another mechanism must be present to explain the results observed during network compensation. LCs receive common excitatory inputs from the pacemakers and one hypothesis is that changing the strength of these chemical synapses might help to restore LC firing to appropriate levels. LCs in the network are also electrically coupled to one another via gap junctions which presumably promotes synchrony, although clearly the native coupling is not able to maintain LC synchrony in TEA (Hagiwara et al., 1959; Tazaki and Cooke, 1983; Cooke, 2002). A second hypothesis is that increased electrotonic coupling between LCs could buffer against disparate output and help to restore synchrony.

Using our set of model networks, we increased and decreased the strength of chemical synapses in 10% increments to test the effects on excitability and synchrony. We then did the same with model electrical synapses. We found that increasing the strength of either chemical or electrical synapses increased both synchrony and excitability (**Figure 2** left). However, increasing the chemical synaptic conductance in conjunction with TEA blockade also increases spiking of the LCs ~25-30% in contrast with the biological decrease in excitability relative to the acute TEA exposure seen with compensation. Conversely, only a small change in LC spiking occurs with an increase in electrical coupling (~9%, **Figure 2** left). Reducing the strength of either chemical or electrical synapses decreased overall spike synchrony (**Figure 2** right), violating the assumptions of compensation based on the biological data. Reducing chemical synaptic strength eventually ceased LC firing altogether.

Interaction of Intrinsic and Electrical Synaptic Compensation

Our modelling results suggest that although an increase in GA is able to counter the increase in excitability of LCs in TEA in a compensatory fashion, as well as promote restoration of synchrony, such an intrinsic compensation was insufficient to restore synchrony fully. Additionally, our results suggest that an increase in coupling among LCs can greatly promote synchrony with only a modest effect on excitability. Therefore, we next used our model networks to investigate how GA and GC might interact to promote synchrony by calculating synchrony scores as conductances of all 27 model networks were adjusted. First we increased GA alone in 10% increments up to a 100% increase (**Figure 3**). Increasing GA up to +40% promoted greater synchrony after TEA blockade but was unable to fully restore synchrony even with increasing conductance levels. Increasing GA beyond +40% did not further improve synchrony (**Figure 3**), and ultimately caused LCs to cease firing altogether. We also increased model GC incrementally (from +10% to +150%) and found that electrical coupling alone was capable of restoring synchrony fully, but this required a 140% increase in its value (**Figure 3A**). Finally, we increased both GA and GC together in 10% increments, revealing a potentially synergistic relationship: a smaller increase of 70% in each conductance was able to produce spike synchrony that was indistinguishable from control (**Figure 3A, 3B**).

3.6 DISCUSSION

Multi-component Compensation Can Synergistically Restore Network Output

Previous modeling studies found that K+ currents can increase or help restore synchrony between electrically coupled neurons (Pfeuty et al., 2003), so we first hypothesized that a compensatory increase in A-Type K+ membrane conductance could be a mechanism underlying both restored excitability and resynchronization. Over the course of 30-60 minutes, increased IA was associated with decreasing cellular excitability [see also (Golowasch et al., 1999)] and improvement of coordinated motor neuron firing. However, intrinsic compensation alone was insufficient to fully restore synchrony across LCs. A concomitant increase in electrotonic coupling ensured virtually complete resynchronization. Our results suggest that although a sufficient increase in electrical coupling alone could restore full synchrony (140% increase), it could not simultaneously restore the original level of excitability. Only a 70% increase was necessary when accompanied by a concomitant increase in GA. Therefore, we conclude that multi-component mechanisms are not only necessary for full compensation, but also that their synergistic action is potentially more efficient than either mechanism operating in isolation.

Physiological Regulation of Coupling Conductance

The speed (within 30 minutes) and magnitude (up to a doubling of effective coupling) of physiological changes seen in electrical coupling was remarkable. Although electrical coupling has long been known to promote synchrony in many systems, including the CG (Tazaki, 1972; Bennett and Zukin, 2004), the physiological interaction of electrical coupling with intrinsic conductances to affect a compensatory output has not been examined. Previous work in the crustacean STG has demonstrated how synchronized activity of pacemaker cells is dependent on an interaction of intrinsic conductances and electrical coupling (Szücs et al., 2000, 2001; Soto-

Treviño et al., 2005), and that distinct circuits can be brought into synchrony via manipulations of electrical and chemical synapses (Elson et al., 1998; Szücs et al., 2000, 2009). But none of these studies have addressed the interaction of membrane conductance and electrical coupling in a compensatory context. Similarly, plasticity of electrical synapses has drawn considerable attention after being discovered in the mammalian central nervous system, including the thalamic reticular nucleus (Landisman and Connors, 2005; Haas et al., 2011), inferior olive (Lefler et al., 2014; Mathy et al., 2014), and retina (Kothmann et al., 2009; Völgyi et al., 2013). Studies in the thalamic reticular nucleus have suggested that potentially compensatory changes in coupling are important to maintain network stability as large changes in intrinsic excitability occur across development (Parker et al., 2009). These discoveries increased awareness of the complex functional roles and plasticity of coupling (Pereda et al., 2013; O’Brien, 2014; Haas, 2015), and also spurred research to identify molecular mechanisms that underlie plasticity and maintenance of these structures (Flores et al., 2012; Li et al., 2012; Turecek et al., 2014). Our study adds to this growing appreciation for plasticity of electrical synaptic connections in the context of homeostatic plasticity.

3.7 TABLES

Table 1. Nominal model conductance values:

Conductance	Value (S/cm^2)
Leak	2e-4
A	6e-4
BKKCa	7.3e-3
g1_Kd2	3e-4
g2_Kd2	3.5e-5
CaL	1.7e-4
CAN	1.06e-4
SKKCa	8.79e-5
CaPQ	1.5e-4
NaP	3.06 e-4

Table 2. Model current parameters.

I_{ion}	x^p	x_∞	τ_x (msec)
I_A	m^3	$\frac{1}{1+\exp((V+21.46)/-17.96)}$	$3.002+\frac{4.073}{1+\exp((V+24.18)/2.592)}$
	h	$\frac{1}{1+\exp((V+21.14)/25.99)}$	$9.434+\frac{11.7}{1+\exp((V+1)/5.317)}$
I_{CaS}	m^2	$\frac{1}{1+\exp((V+24.75)/-5)}$	$20+\frac{50.2}{\exp((V+20.25)/1)}$
	h	$\frac{45}{40+[Ca^{2+}]}$	$\frac{1}{0.02}$
I_{CaT}	m	$\frac{1}{1+\exp((V+20)/-1.898)}$	$18.51-\frac{3.388}{\exp((V-6.53)/9.736)+\exp((V+12.39/-2.525)}$
	h	$\frac{1}{1+\exp((V+55.27)/6.11)}$	$20.23+\frac{40}{\exp((V+23.48)/-9.976)+\exp((V+5.196)/10.84)}$
I_{Kd}	m_1^4	$\frac{1}{1+\exp((V+24.19)/-10.77)}$	$25.049+\frac{25}{1+\exp((V+25.84)/6.252)}$
	h_1	$0.3+\frac{1-0.3}{1+\exp((V+15.87)/5.916)}$	$550+\frac{954.9}{\exp((V+10.8)/-15)}$
	m_2^4	$\frac{1}{1+\exp((V+23.32)/-10)}$	$100+\frac{550}{\exp((V+15)/12.46)}$
I_{NaP}	m^3	$\frac{1}{1+\exp((V+32.7)/-18.81)}$	$3.15+\frac{0.8464}{\exp((V+0.8703)/-6.106)}$
I_{CAN}	w	$(0.0002*[Ca^{2+}]\text{^}2/(0.0002*[Ca^{2+}]\text{^}2+0.05))$	$(40/(0.0002*[Ca^{2+}]\text{^}2+0.05))$
I_{SKKCa}	w	$(0.0001*[Ca^{2+}]\text{^}2/(0.0001*[Ca^{2+}]\text{^}2+0.1))$	$(4/(0.0001*[Ca^{2+}]\text{^}2+0.1))$
I_{BKKCa}	a	$\frac{[Ca^{2+}]}{(1+\exp((V-15+0.08*[Ca^{2+}])/-15)*(1+\exp((V+5+0.08*[Ca^{2+}])/-9)*(2\,-}$	$\frac{1}{0.4}$
	b	$\frac{7}{5+[Ca^{2+}]}$	$\frac{1}{0.2}$

F = Faradays constant
R = Gas constant
V = Membrane voltage
$[Ca^{2+}]$ = intracellular Calcium concentration

3.8 FIGURES

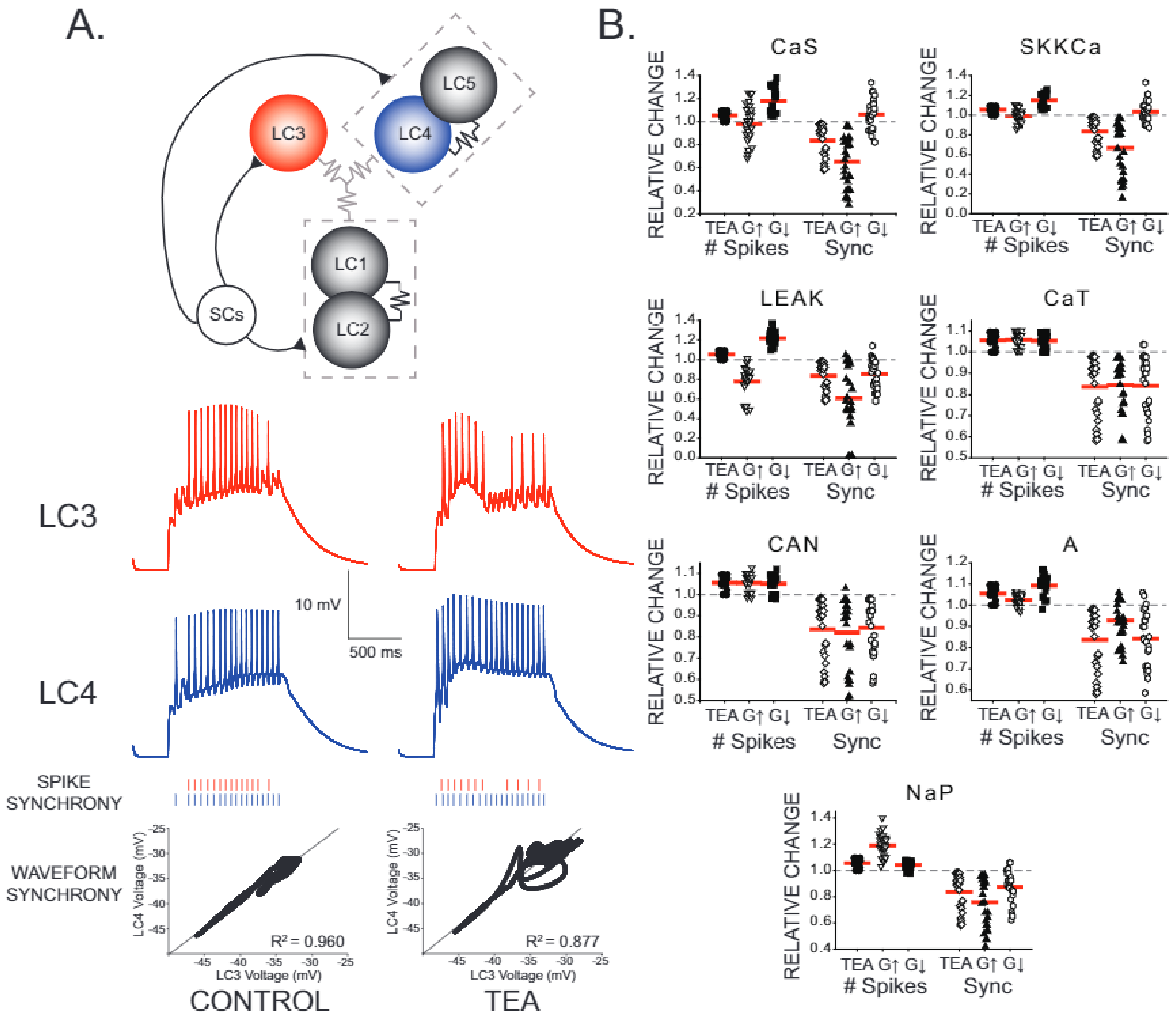

Figure 1. Effects of increasing and decreasing individual ionic conductances on excitability and synchrony in model CG networks. (A) Schematic representation of model network organization and connectivity. Five large cell (LC) motor neurons are innervated via excitatory synapses from a common small cell pacemaker input (SCs). LC model neurons consist of two compartments - soma and axon - of which only the somata are pictured. Somata contain 9 conductances: GCaS, GCaT, GLEAK, GCAN, GA, GBKKCa, GSKKCa, GKd, and GNaP. Paired LCs (1+2, 4+5) have stronger local coupling (black resistor symbols), and all 5 LCs are reciprocally electrically coupled via weaker gap junctions (gray resistor symbols). An example of LC3 and LC4 model output within a network burst activity is shown in the red and blue traces under both control and TEA (90% reduction in both GKdand GBKKCa) conditions. Graphical representations of spike synchrony (raster plots) and waveform synchrony are shown for the model neurons, demonstrating that both measures reflect the loss of LC synchrony as a result of TEA. (B) Measurements of both output variables (# of spikes and spike synchrony) were made under three

model conditions: control, TEA, and TEA + either a 2x increase (G") or 2x decrease (G#) in a given conductance. N = 27 distinct model networks. All output measurements are normalized to their initial (control) conditions. Red lines represent the mean for a given group. Dashed line represents the 1.0 value (baseline) for a given measure. Compensatory responses that restore excitability and synchrony will tend to move the mean towards baseline

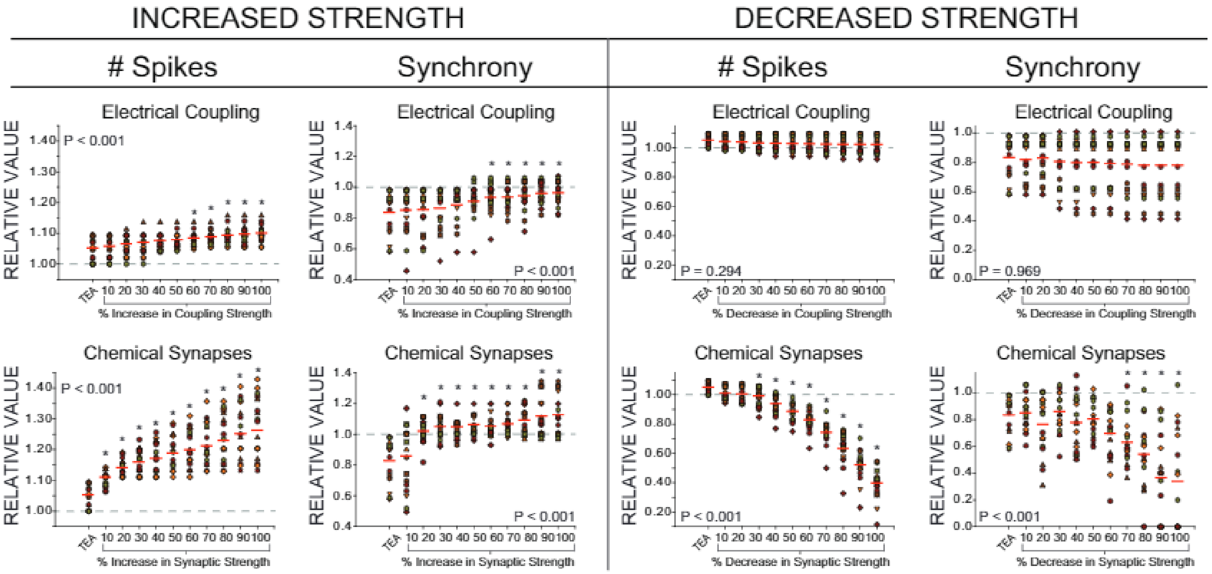

Figure 2. Effects of increased or decreased strength of chemical synapses and electrical coupling on excitability and synchrony in model CG networks. Measurements of two output variables (# of spikes and synchrony) were made under three model conditions: control, TEA (90% reduction in both GKdand GBKKCa), and TEA + an incremental increase or decrease (up to 100% by 10% increments) for both chemical (pacemaker to LC) or electrical (LC to LC) connections. N = 27 distinct model networks. All output measurements are normalized to their initial (control) conditions to visualize trends. Dashed line represents the 1.0 value (baseline) for a given measure. Red lines represent the mean for each group. Each different color and shape for points corresponds to one model network, and the same networks are shown across conductance levels. P-values in each plot refer to the results of a one-way ANOVA across all groups. Asterisks (*) denote groups in each plot that were significantly different from the TEA group via Holm-Sidak post-hoc tests.

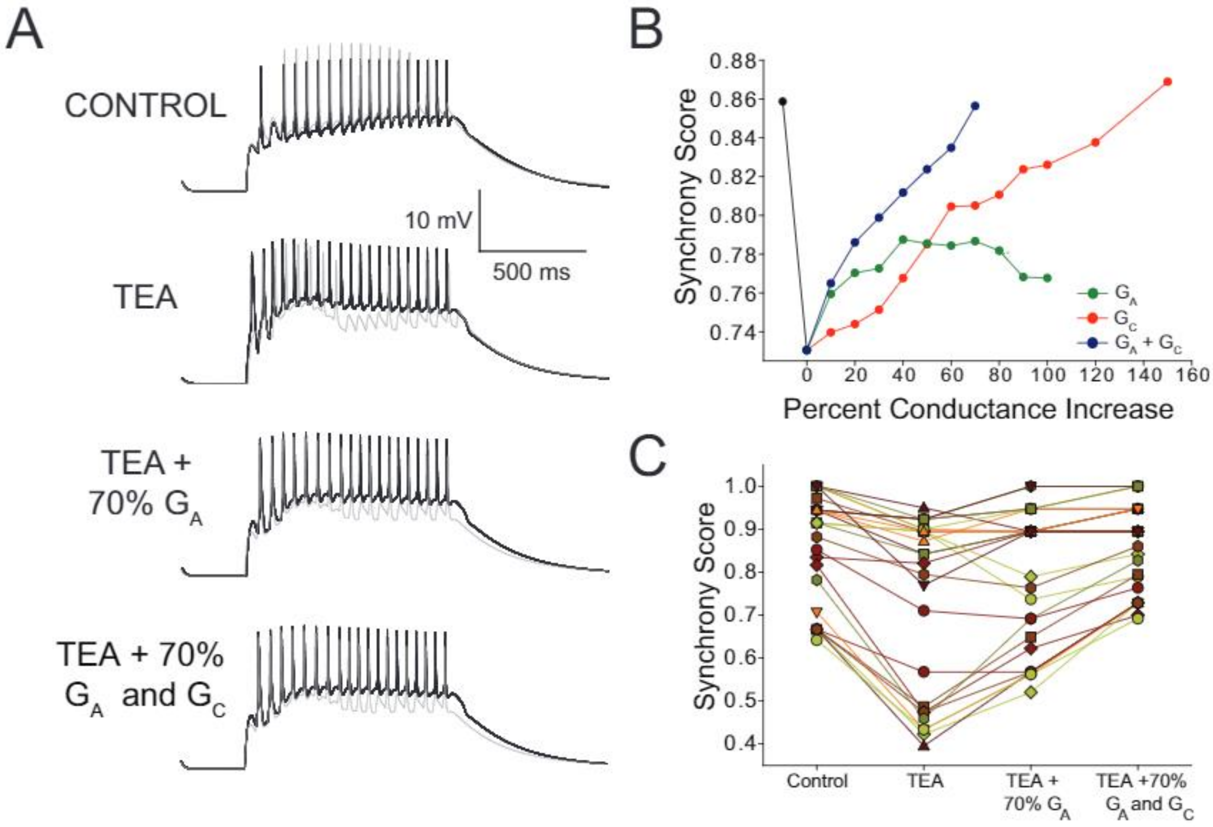

Figure 3. Increased GA and coupling conductance (GC) among LCs act in concert to help restore synchrony across LCs in model networks. (A) Voltage response of a typical network LC3 (gray) and LC4 (black) cells under three model conditions: control, TEA (90% reduction in both GKd and GBKKCa), TEA+ 70% increase in GA, and TEA + 70% increase in GA and GC. (B) Effects of increasing GA alone, GC alone, or both GA and GCon synchrony in model networks. Dashed lines represent simple linear regression fits to the points for each condition. Black line represents the change in synchrony from control to TEA. Points shown are the average values for N = 27 networks. (C) Summary of Synchrony Score shown for all 27 model networks. Stepwise changes are shown from Control, TEA, TEA + increasing GA by 70%, and TEA + increasing both GA and GC by 70% (the point at which maximal synchrony is restored as per the analysis in panel B). Individual points correspond to those used to generate averages in panel A at the 70% level to give an idea of the variability in the data set. Individual preparations are connected with lines to show trends across networks

3.9 REFERENCES

Ball JM, Franklin CC, Tobin AE, Schulz DJ, Nair SS (2010) Coregulation of ion channel conductances preserves output in a computational model of a crustacean cardiac motor neuron. J Neurosci 30:8637– 8649.

Bergquist S, Dickman DK, Davis GW (2010) A hierarchy of cell intrinsic and target-derived homeostatic signaling. Neuron 66:220 –234.

Berlind JA (1989) Feedback from motor neurones to pacemaker neurons in lobster cardiac ganglion contributes to regulation of burst frequency. J Exp Biol 141:277–294.

Cooke IM (2002) Reliable, responsive pacemaking and pattern generation with minimal cell numbers: the crustacean cardiac ganglion. Biol Bull 202:108 –136.

Franklin CC, Ball JM, Schulz DJ, Nair SS (2010) Generation and preservation of the slow underlying membrane potential oscillation in model bursting neurons. J Neurophysiol 104:1589 –1602.

Goaillard JM, Taylor AL, Schulz DJ, Marder E (2009) Functional consequences of animal-to-animal variation in circuit parameters. Nat Neurosci 12:1424 –1430.

Golowasch J, Goldman MS, Abbott LF, Marder E (2002) Failure of averaging in theconstruction of a conductance-based neuron model. J Neurophysiol 87:1129–1131.

Golowasch J, Marder E (1992) Ionic currents of the lateral pyloric neuron of the stomatogastric ganglion of the crab. J Neurophysiol 67:318 –331.

Golowasch J, Abbott LF, Marder E (1999) Activity-dependent regulation of potassium currents in an identified neuron of the stomatogastric ganglion of the crab Cancer borealis. J Neurosci 19:RC33.

Golowasch J, Goldman MS, Abbott LF, Marder E (2002) Failure of averaging in the construction of a conductance-based neuron model. J Neurophysiol 87:1129–1131.

Goldman MS, Golowasch J, Marder E, Abbott LF (2001) Global structure, robustness, and modulation of neuronal models. J Neurosci 21:5229–5238.

Günay C, Edgerton JR, Jaeger D (2008) Channel density distributions explain spiking variability in the globus pallidus: A combined physiology and computer simulation database approach. J Neurosci 28:7476–7491.

Haedo RJ, Golowasch J (2006) Ionic mechanism underlying recovery of rhythmic activity in adult isolated neurons. J Neurophysiol 96:1860–1876.

Harris-WarrickRM (2011) Neuromodulation and flexibility in Central Pattern Generator networks. Curr Opin Neurobiol 21:685– 692.

Khorkova O, Golowasch J (2007) Neuromodulators, not activity, control coordinated expression of ionic currents. J Neurosci 27:8709–8718.

Kim M, Baro DJ, Lanning CC, Doshi M, Moskowitz HS, Farnham J, Harris-Warrick RM (1998) Expression of Panulirus shaker potassium channel splice variants. Receptors Channels 5:291–304.

MacLean JN, Zhang Y, Johnson BR, Harris-WarrickRM (2003) Activity-independent homeostasis in rhythmically active neurons. Neuron 37:109 –120.

MacLean JN, Zhang Y, Goeritz ML, Casey R, Oliva R, Guckenheimer J, Harris-Warrick RM (2005) Activity-independent coregulation of IA and Ih in rhythmically active neurons. J Neurophysiol 94:3601–3617.

Marder E (2011) Variability, compensation, and modulation in neurons and circuits. Proc Natl Acad Sci U S A 108:15542–15548.

Nerbonne JM, Gerber BR, Norris A, Burkhalter A (2008) Electrical remodeling maintains firing properties in cortical pyramidal neurons lacking KCND2-encoded A-type K_ currents. J Physiol 586:1565–1579.

Olypher AV, Calabrese RL (2007) Using constraints on neuronal activity to reveal compensatory changes in neuronal parameters. J Neurophysiol 98:3749–3758.

Olypher AV, Prinz AA (2010) Geometry and dynamics of activity-dependent homeostatic regulation in neurons. J. Comput. Neurosci. 28:361–374.

O'Leary T, Williams AH, Caplan JS, Marder E (2013) Correlations in ion channel expression emerge from homeostatic tuning rules. PNAS 110(28) 2645-2654.

O'Leary T, van Rossum MC, Wyllie DJ (2010) Homeostasis of intrinsic excitability in hippocampal neurones: dynamics and mechanism of the response to chronic depolarization. J Physiol 588:157–170.

Schulz DJ, Goaillard JM, Marder E (2006a) Variable channel expression in identified single and electrically coupled neurons in different animals. Nat Neurosci 9:356 –362.

Schulz DJ, Baines RA, Hempel CM, Li L, Liss B, MisonouH (2006b) Cellular excitability and the regulation of functional neuronal identity: from gene expression to neuromodulation. J Neurosci 26:10362–10367.

Schulz DJ, Goaillard JM, Marder EE (2007) Quantitative expression profiling of identified neurons reveals cell-specific constraints on highly variable levels of gene expression. Proc Natl Acad SciU S A 104:13187–13191.

Swensen AM, Bean BP (2005) Robustness of burst firing in dissociated purkinje neurons with acute or long-term reductions in sodium conductance. J Neurosci 25:3509–3520.

Taylor AL, Goaillard JM, Marder E (2009) How multiple conductances determine electrophysiological properties in a multicompartment model. J Neurosci 29(17):5573–5586.

Taylor AL, Marder E (2011) Multiple models to capture the variability in biological neurons and networks. Nat Neurosci 14, 133–138.

Tazaki K, Cooke IM (1979) Isolation and characterization of slow, depolarizing responses of cardiac ganglion neurons in the crab, Portunus sanguinolentus. J Neurophysiol 42:1000 –1021.

Tazaki K, Cooke IM (1983a) Separation of neuronal sites of driver potential and impulse generation by ligaturing in the cardiac ganglion of the lobster, Homarus americanus. J Comp Physiol A Neuroethol Sens Neural Behav Physiol 151:329 –346.

Tazaki K, Cooke IM (1983b) Neuronal mechanisms underlying rhythmic bursts in crustacean cardiac ganglia. Symp Soc Exp Biol 37:129 –157.

Tazaki K, Cooke IM (1983c) Topographical localization of function in the cardiac ganglion of the crab, Portunus sanguinolentus. J Comp Physiol A Neuroethol Sens Neural Behav Physiol 151:311–328.

Tobin AE, Cruz-Bermudez ND, Marder E, Schulz DJ (2009) Correlations in ion channel mRNA in rhythmically active neurons. PLoS One 4:e6742.

Turrigiano G (2011) Too many cooks? Intrinsic and synaptic homeostatic mechanisms in cortical circuit refinement. Annu Rev Neurosci 34:89 –103.

Turrigiano G (2012) Homeostatic synaptic plasticity: local and global mechanisms for stabilizing neuronal function. Cold Spring Harb Perspect Biol 4:a005736.

Turrigiano G, Abbott LF, Marder E (1994) Activity-dependent changes in the intrinsic properties of cultured neurons. Science 264:974 –977.

Turrigiano G, LeMasson G, Marder E (1995) Selective regulation of current densities underlies spontaneous changes in the activity of cultured neurons. J Neurosci 15:3640 –3652.

Wang X, Buzsaki G (1996) Gamma Oscillation by Synaptic Inhibition in a Hippocampal Interneuronal Network Model. J Neurosci 20:6402–6413.

CHAPTER 4

MORPHOLOGICAL CRUSTACEAN CARDIAC GANGLION CELL MODEL REVEALS DIFFERENTIAL ROLES OF CONDUCTANCES IN COMPARTMENTS

4.1 INTRODUCTION

Neurons are endowed with a rich and complex set of intrinsic and synaptic conductances that control their electrical activity [1; 2]. Although the role of such a varied set of conductances is not fully understood, it is natural to expect that neurons of the same cell type would possess similar membrane properties, especially within the same animal. However, experimental findings suggest that maximal conductance levels of individual currents can vary two- to six-fold among same cell types, even within the same animal [3-7] and that different combinations of conductances preserve activity at the single cell level [8; 9]. Computational modeling continues to shed light on the role of such conductance variations in conserving cellular output such as spike and burst characteristics [2; 12-20]. For instance, Prinz et al. [2] explored the maximal conductance space of a single-compartment model neuron to quantify the numerous types of spiking and bursting models and showed that similar patterns of activity could be produced by many different parameters sets, both for single neurons [2] and within small networks [21]. Beyond the broad range of conductance combinations that are associated with convergent outputs among neurons of the same type, there is also substantial reports that among populations of neurons different sets of ionic conductances [5] and ion channel mRNA levels [7; 10] can be correlated with one another in different classes of identified neurons. This suggests that an on-going, rather than developmentally fixed, regulation of specific sets of conductances may be necessary to provide stable output of neurons and networks over the lifetime of an animal. These correlated mRNA and conductance levels can arise from a relatively simple set of feedback control algorithms in computational models. However, there have been few studies that directly demonstrate that these conductance or mRNA relationships are *necessary* to generate appropriate, ongoing neuronal activity in biological neurons. Indeed, compelling computational work has demonstrated that – at least theoretically – such relationships are not necessary to generate robust output in a population of model neurons. For example, previous studies have demonstrated that using a model selection methodology focused on single-cell output in a multi-compartment model results in a population of cells with only weak or no correlations among conductances. However, most studies to date have focused on selecting models based on isolated neuron activity. Therefore, to further extend these analyses, we performed multiple levels of selection that included generating model networks with multiple neurons of a given type, and only selecting cells that perform within biological parameters of the full network output for inclusion in our population. We then looked for conductance correlation relationships among the populations of neurons in our simulated model networks.

For this work, we use a computational model of the crustacean cardiac ganglion (CG) network, based on the crab, *Cancer borealis.* These simple networks consist of 4 pacemaker neurons and 5 Large Cell (LC) motor neurons that innervate the heart muscle. The present study extends previous computational investigations that focused on single compartment cardiac ganglion LCs by considering the potential role of conductances in multiple compartments of an LC on its output. Specifically, we investigate how the distribution as well as potential covariations of conductances affect soma membrane potential response (output), using a morphologically realistic three-compartment LC model of *Cancer borealis* that incorporates first-hand biological data. Using a rejection sampling approach with a 9-D parameter space of maximal conductances, we report, as in previous studies, an unbiased approach to determine the role of various conductances in shaping cellular and network function. We extend previous studies by performing model neuron selection in complete CG networks, with constraints drawn from intact network activity as well as single cell input-output functions. A population of model LCs generated by such an approach then provided predictions of the differential roles of conductances in the soma vs. neurite in shaping neuronal output. Further, this population of neurons allowed us to look for emergent conductance relationships both within and across these compartments. Finally, we compare conductance relationships uncovered through the model selection process with a comprehensive set of single-cell mRNA relationships for channels underlying these membrane conductance relationships.

4.2 METHODS

Experimental data to constrain single cell and network models.

The biological data used to constrain both the model parameters (e.g., membrane currents) and outputs (both isolated and intact) were ultimately collected under the auspices of previously published work as follows.

Membrane currents were made in two-electrode voltage clamp while the network activity was silenced either with tetrodotoxin (TTX) or by severing the CG nerve trunk to remove the small cell (SC) inputs. The inward currents ICaS, ICaT, INaP, and ICAN were based on recordings and data as described in Ransdell at el. 2013. The outward currents IA, IKd, IBKKCa were based on recordings made in Ransdell et al. 2012. No biological characterization of SKKCa has been performed in crabs, and this work carries over SKKCa model currents as described in our previous CG modeling efforts (Lane et al. 2016). Intracellular voltage follower recordings of ongoing network activity were made in all the above studies, and from these we generated the biological parameters to constrain model network output.

Synaptic inputs (chemical) and connections (electrical) were characterized from these recordings as well. EPSPs were characterized by measuring the amplitude and time constant characteristics from intracellular LC recordings in intact networks. Single SC action potentials that yielded clear (non-summating) EPSPs were used to generate a population of post-synaptic potential measurements that constrained the chemical synapse inputs. Electrical coupling was measured directly in two-electrode current clamp as described in Lane et al. 2016.

To characterize isolated LC soma responses with and without TEA, we used a current clamp protocol designed to emulate SC synaptic inputs. These chemical synapse stimulus protocols are described in detail in Ransdell et al. 2013.

Finally, mRNA levels for ion channels were taken from previously published work by Northcutt et al. 2019 and analyzed and formatted for use towards the experimental goals in this study.

Development of biophysical single cell models

The single cell model had three compartments: soma, neurite (neu) and spike-initiation-zone (SIZ). The soma compartment had a length of 120 µm and a diameter of 90 µm and contained 9 currents. The neurite had a length of 1380 µm, and a diameter of 12 µm, and contained 5 currents. The SIZ had a length of 108 µm, and a diameter of 20 µm, and contained 3 currents. The Na and K channels in the SIZ were given fixed conductances of 0.2 and 0.4 S/cm^2, respectively, and we assumed a specific capacitance of 1.5 µF/cm^2 for all three structures. The model for currents for each compartment followed the Hodgkin-Huxley equation formulation (Eqn. 1)

$$C_{soma}\frac{dV}{dt} = -I_A - I_{Kd} - I_{Nap} - I_{CaS} - I_{CaT} - I_{CAN} - I_{SKKCa} - I_{BKKCa} - I_{leak} - I_{soma-to-neu}$$

(Soma)

$$C_{neu}\frac{dV}{dt} = -I_{CaT} - I_{CaS} - I_{BKKCa} - I_{NaP} - I_{leak} - I_{neu-to-soma} \qquad \text{(Neurite)}$$

$$C_{siz}\frac{dV}{dt} = -I_{Na} - I_{Kdr} - I_{leak} - I_{siz-to-neu} \qquad \text{(SIZ)} \qquad (1)$$

where the currents on the right-hand side of the first equation are: A-type potassium (I_A), delayed rectifier (I_{Kd}), persistent sodium (I_{Nap}), slow persistent calcium (I_{CaS}), transient calcium (I_{CaT}), calcium-dependent non-selective cation (I_{CAN}), two calcium-dependent potassium currents (I_{SKKCa} and I_{BKKCa}), leak (I_{Leak}) and the injected current (I_{inj}). The individual currents were modeled as $I_c = g_{max,c} m^p h^q (V - E_c)$, where $g_{max,c}$ is its maximal conductance, *m* its activation variable (with exponent *p*), *h* its inactivation variable (with exponent *q*), and E_c its reversal potential (a similar equation is used for the synaptic current but without *m* and *h*). The kinetic equation for each of the gating functions *x* (*m* or *h*) takes the form

$$\frac{dx}{dt} = \frac{x_\infty\left(V,[Ca^{2+}]_i\right) - x}{\tau_x(V,[Ca^{2+}]_i)}$$

where x_∞ is the steady state gating voltage- and/or Ca^{2+}- dependent gating variable and τ_x is the voltage- and/or Ca^{2+}- dependent time constant. The equations for the active channels in the soma compartment were fit using biological recordings for these currents from our Lab from the cardiac ganglion of *Cancer borealis*. These currents were fit as follows: Voltage clamp data obtained with Clampfit were imported into MATLAB and fit using the MATLAB curve-fitting toolbox. Current data were converted to conductance data by dividing by (V_m – E_{Rev}), where E_{Rev} was as follows: $E_{Na\,=}$ +55 mV, E_K = -80 mV, E_{Ca} = +45 mV, E_{Leak} = -50 mV, and E_{CAN} = -30 mV. The time axis was adjusted to start from 0 for the beginning of the clamp. The following parametrization was used:

$$g(t) = \sum_{i=1}^{n} A_i \left(1 - \exp\left({}^{-t}/_{\tau_{m,i}}\right)\right)\left(h_i - (h_i - 1)\exp\left({}^{-t}/_{\tau_{h,i}}\right)\right)$$

In this equation, $A_i = G_{i,max} \times m_i$ was the maximal conductance of the current i multiplied by its voltage-dependent steady-state activation (m_i), h_i was the steady-state inactivation value, and $\tau_{m,i}$ and $\tau_{h,i}$ were the time constants with which activation and inactivation reached steady-state, respectively. This fitting procedure assumed that ionic currents were completely deactivated m=0 and deinactivated (h=1) prior to the onset of the voltage clamp. This was fit to each trace in voltage clamp experiment, giving values of each of the four parameters for each test clamp voltage (V_c). These values were then fit for each current as functions of V_c using the general forms as stated below. This procedure yielded equations for the currents recorded in voltage clamp that could be used in simulations according to the Hodgkin-Huxley formalism.

$$A(V_c) = G_{max} \times m(V_c) = G_{max} \times \left(1 + \exp\left((V_c - V_{m,1/2})/k_m\right)\right)^{-1}$$
$$h(V_c) = \left(1 + \exp\left((V_c - V_{h,1/2})\ /k_h\right)\right)^{-1}$$
$$\tau_m(V_c) = \tau_{base,m} + \tau_{amp,m}\left(\exp\left((V_c - V_{\tau1,m})\ /k_{\tau1,m}\right) + \exp\left((V_c - V_{\tau2,m})\ /k_{\tau2,m}\right)\right)^{-1}$$
$$\tau_h(V_c) = \tau_{base,h} + \tau_{amp,h}\left(\exp\left((V_c - V_{\tau1,h})\ /k_{\tau1,h}\right) + \exp\left((V_c - V_{\tau2,h})\ /k_{\tau2,h}\right)\right)^{-1}$$

All the maximal conductances ($G_{i,max}$) were in µS, time constants in ms and voltages in mV.

Calcium dynamics. Intracellular calcium modulates the conductance of the calcium-activated potassium currents (BKKCa and SKKCa), calcium-activated nonselective cation current (CAN) and influences the magnitude of the inward calcium current in the LC [1]. A calcium pool was modeled in the LC with its concentration governed by the first-order dynamics [2; 3] below:

$$\tau_{Ca}\frac{d[Ca^{2+}]}{dt} = -F \times I_{Ca} - \left([Ca^{2+}] - [Ca^{2+}]_{rest}\right)$$

where F = 0.256 μM/nA is the constant specifying the amount of calcium influx that results per unit (nanoampere) inward calcium current; τ_{Ca} represents the calcium removal rate from the pool; and $[Ca^{2+}]_{rest}$ = 0.5 μM. Voltage-clamp experiments of the calcium current in the our lab showed the calcium buffering time constant to be around 690 ms (τ_{Ca}).

Searching for LC neurons within the model parameter space

We used a three-stage rejection protocol to select viable networks with five distinct LC cells, with each LC satisfying biological single cell and current injection responses. For the single cell model search, we started with a set 100,000 three-compartment cell models with the 14 conductances and the small cell frequency selected randomly from uniform distributions of values between their respective minimum and maximums given in **Table 3**. The SC frequency range of 16-32 Hz was determined from SC recordings from our lab (**Table 1**). The recordings showed that the combined small and medium spike frequency averages had minimum and maximum frequency of 16 Hz and 32 Hz, respectively.

In stage 1 of the rejection protocol, ligated soma (soma + neurite) models were tested for passive properties of resting membrane potential, time constant and input resistance. Cells for which these values were within ranges in **Table 4** were retained. In stage 2, SIZ was added to the passing cells and a synaptic input (spike train mimicking SC input) was provided. Based on biological recordings from our Lab, on average, the average values for an SC burst were as follows: period was 1000 ms, and the synaptic input consisted of two added waveforms, a higher frequency for the entire duration of 1000 ms, and a lower frequency for 600 ms. The initial SC burst was for 300 ms, and this was followed with a higher frequency for 600 ms, i.e., till 900 ms, after which it fell back to the original frequency and terminated at 1000 ms. The synapse had a fixed gain of 0.07017μS. The frequency of SC input is randomly picked as two numbers whose sum is in the biological range of 16-32 Hz. For example, the two could be 22 and 7, and this would be implemented as follows: the first spike train would be at 22 Hz for the entire 1000 ms duration, and the second one will be added to it from 300 ms to 900 ms, to provide 29 Hz during the 300-900 ms duration. Then run all the networks with this SC input. Then select two other number and repeat the process.

Both control and post-TEA case are considered and intact cells whose resulting membrane potential waveform characteristics were within the ranges shown in **Table 5** were retained. In a third stage, we assemble networks and select viable ones as described next.

Development of conductance-based model networks

First, we randomly selected five distinct LCs for the network from the pool of intact LCs that pass Stage 2. Then we connected the SIZ with synapse to the distal end of the neurite for each LC, and connected LC4-5 and LC1-2 somas with separate gap junction values that were determined experimentally in our lab (**Table 3**). The SC pacemaker drive was delivered as a spike train to the five excitatory synapses. It was observed biologically that frequency of SC firing increases within the slow wave oscillation cycle of LCs.

Experimental TEA block was simulated by reducing the conductances G_{BKKCa}, G_{Kd} and G_A by 97% in the LCs and neurite (Ransdell et al., 2013a). Synchrony scores were computed by using the R^2 between all the large cells. To determine the range for synchrony scores, we examined five experimental recordings for LC3 and LC5. Taking the first two minutes of TEA exposure (acute), we measured the R^2 between LC3 and LC5 recordings. We chose the maximum of TEA synchrony to be the lowest control synchrony score minus 1.5 times the control interquartile range. The lowest control synchrony score was 0.9425, and the control interquartile range was 0.0318, therefore the maximum of TEA synchrony was taken to be 0.8948. The cells were considered desynchronized if the synchrony score was below 0.9425. For the synchrony score between LC3 and LC5, we considered anything below 0.89 to be asynchronous, and anything above 0.9425 to be demonstrating synchrony. The average synchrony score (not used for rejection, but for other calculations in Results) is compared with the maximal conductance averages and SC frequency. The average synchrony score is the mean synchrony score between all LC's (10 combinations per network) in the pre- and post-TEA case.

After performing control and TEA runs using these networks, in the third stage, we rejected networks that had waveform characteristics outside the ranges shown in **Table 6**. We rejected networks that showed increased TEA synchrony between LC3 and LC5, or decreased spikes per burst since neither behavior was observed in biological traces. This left 27 networks that reproduced the biological trends, and these were used in subsequent analyses to explore potential conductance changes that could restore network synchrony.

4.3 RESULTS

Morphologically realistic LC model and SC stimulus design reproduces experimental profiles

Building on our previous two-compartment LC model [17; 18; 22] we added morphological realism to the LC by adding a third compartment, the neurite (**Fig 1**). We first matched passive properties (see methods) and waveform data from intact cells LC3 and LC4 (**Fig. 1A**; [22]). We note that among the five LCs, only LC3-5 are easily accessible, and LC4 is gap-junction coupled strongly to LC5 [11]. Accordingly, our biological data are from LCs 3-5, while our model predicts network performance for all five LCs, assuming LCs1-2 have similar gap junction coupling as LC4-5 (**Fig. 1A**).

Developing rejection protocol criteria from experimental data: We briefly describe the key characteristics of a modified version of our previous rejection protocol to select model LCs that match experimental data [22]. In the first stage, we sampled a 9-D parameter space of maximal conductance to generate a pool of ligated LCs (soma + neurite with passive conductances) for which the passive properties of resting potential and input resistance were within biological ranges measured in our Lab [11]; this relaxed some of the constraints in our previous protocol (see methods) and permitted more cells to pass this stage. To the cells that passed, we then added a neurite (with conductances picked randomly – see below) and an SIZ (with fixed conductances) in stage 2, and then provided synaptic input from the SC between the experimentally observed range of 16-32 Hz and retained only cells that had at least one spike with a small cell spike train input. This ensured that stage 2 did not pass cells that only had membrane depolarizations but no spikes, reducing the load on the computationally intensive stage 3. In a third stage, we combine five viable randomly selected single cells into a network. The network itself is deemed viable if it satisfied the two experimental data for LC3 and LC5: (i) a synchrony value between LC3 and LC5 >0.95 in control (Pearson's R-squared); and (ii) synchrony between LC3 and LC5 <0.89 in TEA. Results from each of these stages are discussed next.

Membrane potential responses of ligated cells: The ligated cell (soma + neurite) model was tested for passive properties based on experimental data from our Lab [11]. From among 150,000 ligated model cells with random conductances selected from the 9-D parameter space (see methods), 100,000 passed stage 1 of the rejection protocol. **Figure 1B** shows a representative experimental (left) and model (right) membrane potential responses of a ligated cell to an experimentally determined input (termed 'stimulus protocol'; [11]; see methods) in control and post-TEA conditions. After finding viable ligated cells (soma and passive neurite), we attached an SIZ to each cell in the pool for testing in stages 2 and 3. For this, we designed an SC input to represent experimentally determined SC input characteristics as described next.

Designing the SC input to the LC network: The five-cell LC network receives input from a cluster of four small cells, and we assumed that all five LCs receive a common synchronized input from this SC cell cluster. We designed the SC input as a spike train to a synapse on the SIZ, the properties of which are tuned to mimic experimental voltage responses [23]. Experimental recordings from the Schulz Lab (see Suppl Matls.) showed that SC input frequency varied between 16 and 32 Hz. Also, it appeared to have two components over a typical period of 1000 ms, a steady one that continued over the entire duration, and a second one that lasted for 600 ms, starting from 300 ms and ending at 900 ms. As described in methods, we designed SC inputs with the two components, after randomly picking a frequency within the rage of 16-32 Hz.

Network Responses - matching responses of intact single cells: The SC input we designed was then used in the next stage to provide input to intact cells formed by adding an SIZ and synapse to the ligated cell model. **Figure 1C** shows the experimental recording for an intact LC4 cell (left panel leftmost is control). A typical response from the model intact cell is shown in the right panel. To make the analysis tractable, we considered the case where the intact cells in a network did not receive input from the other four LCs, i.e., all gap junction coupling between the LCs were disconnected. We will consider the SIZ gap-junction coupled case in a later section.

For such intact single LCs, we initially assumed passive neurites, i.e., only leak conductance in the neurite. So, to the model cells that passed stage 1, we connected an SIZ and synapse, and used the SC spike train input described in the previous section. Interestingly, none of the 100,000 cells passing stage 1 were able to pass stage 2. This was because the cells had a spiking frequency above 8 Hz in control and did not exhibit a TEA response. However, the SIZ responses did match biological reports. Specifically, the biological membrane potential responses at the soma had a depolarization of 10 mV for 1000 ms, and with spikes on top of the depolarization that reached 20 mV in height. This response matched the soma membrane potential response characteristics from our lab that had a depolarization bump of 10 mV for 1000 ms, and spike height of 15 mV (**Fig. 1C1**). Additionally, the model SIZ spike height attenuated by a factor of 3.5 (70 to 20 mV) at the soma, matching the corresponding biological recordings from our Lab which had an attenuation factor of 3.66 (55 to 15 mV) (unpublished data; also matched experimental SIZ recording in [23]).

The functional reason for the cells failing in stage 2 was determined to be the excessive leak through the neurite, i.e., although sufficient current entered the neurite from the SIZ, leakage diminished the amount that reached the soma for raising the response in TEA. Reducing the diameter, and therefore surface area, was found to decrease leakage, but the neurite diameter had to be 5 μm, which was unrealistic compared to biological data that had a minimum of 10 μm. As a next step we considered active conductances.

Active conductances necessary in neurite to reproduce experimental network responses

The presence or role of active conductances in the neurite of the CG LC is unknown. For instance, although our mRNA studies suggest the presence of Nap in the LC, the morphological specificity of location is unknown. Similarly, although Ca2+ currents are thought to be present in the neurite, their localization is not fully understood.

Role of individual conductances: We adopted a systematic procedure to determine a parsimonious set of active conductances in the neurite. For this, we first we inserted only Nap in the neurite, and this helped counter the excessive leakage cited in the previous section, enabling the soma to elicit a TEA response with spiking in SIZ (**Fig. 2A, B**). With Nap in the neurite, for every 1000 cells that passed stage 1, about 35 passed stage 2. Fewer cells passed because the spike height and LC spike frequency were both found to exceed the upper bounds in the control case. For instance, for a case with SC frequency of 22 Hz (low in experimental traces of SC spikes), the soma spike height was above the upper bound of 30 mV (**Table 5**) as was the spike frequency, in many of the control cases. The reason for this was that the cell was already close to excitable in the control case with the passive neurite. The key attribute that Nap provided was a TEA response that met the requirements of increased spike frequency and amplitude (**Fig 2B**) in nearly all cells. So, we considered current channels to reduce the depolarization caused by Nap in the control case while retaining the TEA response. This led to the addition of I_BKKCa but that worked only for some models (**Fig 2C**), even with maximal conductance of I_BKKCa exceeding the upper bound (**Table 2**). Furthermore, this manipulation did not provide the variability in TEA responses seen in experimental traces (**Fig.1D**). Since I_Nap by itself was not sufficient, we then explored whether I_CaT and I_CaS channels could substitute for I_Nap. Even with values of conductances beyond the upper bounds for CaS and CAT channels, the TEA response was inadequate (**Fig 2D**), and the peak spike height in the control case was also too high. So, we added I_BKKCa to this set of I_CaT and I_CaS, without Nap. Although this reduced the peak spike height to within permissible ranges, the TEA response was still inadequate (**Fig 2E**).

To gain insights into the process, we investigated the mechanism by which I_BKKCa improved the TEA response together with I_Nap (**Fig 2C**), and produced variable TEA responses seen in experiments, without disturbing the control responses. First, we found that

I_BKKCa helped reduce the spike amplitude (**compare Fig. 2F and 2G**). However, there was little variability in TEA response waveforms of different cells. To explore why, we investigated the underlying current waveforms (**Fig 2H**). For this cell, I_CaT and I_CaS in the neurite less than 50% of what I_Nap does to the TEA response. The waveform of I_BKKCa corresponds closely in time with those of leak and Nap currents, all of which also closely follow the voltage waveform. This suggests that I_BKKCa has a greater impact on the voltage waveform than did I_CaT and I_CaS. However, the slow wave amplitude could, in general, be modified by I_CaT and I_CaS, allowing the model to exhibit varied TEA waveforms. With all 5 channels present, the waveform criteria for control and TEA case are met by larger numbers of cells (**Fig 2G**), and there is greater variability in the range of TEA responses. A typical set of TEA responses for five intact cells with all channels present is shown in **Fig 2I**. In summary, I_BKKCa (with I_CaT and I_CaS) reduced peak spike height and frequency in the control case. Although I_BKKCa did reduce the increased control response caused by I_Nap, it did not affect I_Nap's facilitation of the TEA response. Furthermore, CaS and CaT channels were found to be important for the generation of varied TEA responses.

Random sampling of neurite conductances: Based on the systematic hand-tuned analysis of the role of conductances in the neurite discussed in the previous section, we decided to add the following current channels to the neurite: CaS, CaT, NaP, BKKCa. The reader is reminded that maximal conductances of the soma currents were finalized in stage 1, and so stage 2 considers only the random selection of maximal conductances for the channels added to the neurite, i.e., stage 2 rejection protocol focused only on conductances in the neurite. Of the100,000 intact cells that passed stage 1, the total number passing stage 2 increased to 18,000, with an active neurite in the model.

Validation check: In our prior experiments with the ligated soma, Ransdell et al.[24] recorded from intact networks and developed a current trace termed 'stimulus protocol' that, when injected into a ligated soma, resulted in a membrane potential profile that matched those from intact network recordings. As a validation experiment, we found that the model current entering the soma from the neurite mimicked the 'stimulus protocol' waveform with active, but not a passive dendrite (**Fig.2J2 vs 2J3**).

Network responses with gap-junction coupling among SIZs

The cells from a sample network that passed this final rejection criteria involving networks (Stage 3) are shown in **Figure 3** (right panel, top right). Of the18,000 model cells that passed stage two, a total of 515 passed stage 3 (103 networks). The dissimilar individual responses of LCs to the SC frequency of 25 Hz became highly synchronized when placed in a network with gap-junction connectivity (**Fig. 3A1,2**). The reader is reminded that a pronounced TEA response is one of the rejection criteria used in Stages 2 and 3 (see methods). We explored the mechanism by which the gap-junction couplings between soma compartments of LCs1-2 and LCs4-5, and between the SIZ compartments (**Fig. 1A**) ensured synchrony among the LCs in the network. For this we considered the cells in the example network in **Figure 3** that passed stage 3 of the rejection protocol, with the same SC input of 25 Hz used for each cell in **Fig. 3A**. In this network, we found that the gap junction current between soma compartments of LCs1-2 or between LCs4-5 was seven- to ten-fold smaller in magnitude than the synaptic current due to the SC drive. Focusing on one cell, LC1, **Fig. 3B1** provides a comparison of the sum of the gap junction current from soma of LC2 to soma of LC1 and from the various SIZ compartments to the SIZ of LC1, labeled as 'gap junction current', to the synaptic current into the SIZ of LC1 due to SC input spikes. As can be seen from the traces, the magnitude of the total gap junction current into LC1 was found to be more than seven-fold smaller than that of the synaptic current into LC1. Also, a comparison of traces in **Fig. 3A** and **B** shows that the soma membrane potential response of LC1 is primarily due to the input from SC rather than from input via gap junctions. The total gap junction current is also phase shifted compared to the synaptic current. This sheds light on the role of the synaptic current which is to raise the SIZ membrane potential to spike threshold in ~900 ms (**Fig. 3B**). Once the threshold is reached in the SIZ and spiking is initiated, the gap junction currents ensure that the spikes are synchronized among the cells, and so the phase shift of ~500 ms between the peak of the depolarization due to the synaptic current and the first peak in gap junction current profiles. Since LCs1-2 and LCs 4-5 have gap junction coupling at the soma, in addition to at the SIZs, the gap junction currents between them at the SIZs is expected to be smaller than the others, for example between LC1 and LC3, as seen in **Fig. 3B2**. As the figures illustrate, the soma voltages can be different, but the gap junction currents between SIZs ensure that their membrane potentials are very close. In summary, the analysis also delineates the primary functions of the two current types: synaptic (to increase SIZ and soma membrane potential to threshold) and gap junction (to synchronize spikes).

These two observations, i.e., the total gap junction current being considerably smaller than the synaptic current, and the soma waveform almost entirely resembling the synaptic current waveform, also justify the use of intact single cells in stage 2 of the rejection protocol, without considering the gap-junction interaction effects from other cells.

Conductance parameter space following three levels of selection on model neurons

Following each of the stages of selection, we examined the overall distribution of membrane conductances in the soma and neurite compartments in the remaining neurons to determine whether each selection criterion limited any conductance to a particular portion of the parameter space (**Figure 4**). We visualize this in two distinct ways. **Figure 4A** uses a density plot to describe the conductances that passed a given level of selection. As selection continued, some conductances were more and more limited to a portion of the parameter space, while others maintained a broader range of viable conductances. For example, selection stages 2 and 3 result in a restricted range of distribution of NaP_{SOMA}, $NaP_{NEURITE}$, $Leak_{SOMA}$, and $Leak_{NEURITE}$. Further, as Vrest was a free parameter in the selection process, we see the strongest selection pressure on this feature, where selection levels 2 and 3 result in a narrow distribution of acceptable values near the high end of the range (**Figure 4A**). The other active conductances maintained a broad range of acceptable values through all levels of selection. However, these are not normally distributed. Rather, multiple peaks around conductance ranges that enriched for successful models can be seen in most of the conductances (**Figure 4A**). Finally, because **Figure 4A** scales each level of selection independently to maximize the opportunity to see variations in the range of conductance values after each selection level, we have also plotted these data in a nested format using a stacked density plot (**Figure 4B**). This provides the opportunity to see the full parameter space (level 0, purple) and then each round of selection as a subset of the remaining parameter space.

Intrinsic conductance covariations in the network model

Biological studies have suggested that it is important and/or necessary for pairs of “modules” of conductance to work in concert to control appropriate physiological output. Therefore, we looked for relationships among all of the membrane conductances in our model – across two compartments (soma and neurite) – at all three levels of selection.

Figure 5 describes membrane conductance relationships in the soma. Correlograms (**Figure 5, top**) demonstrate that there is a general strengthening of conductance correlations [as evidenced by increasing absolute value of rho(ρ)-value] across the levels of selection. To better visualize individual relationships, we have plotted each pairwise correlation coefficient at each level of selection as a barplot matrix (**Figure 5, bottom**). We see several correlations that become apparent as network level selection of model neurons progresses. However, overall, the rho-values for any correlation remain relatively low, with the highest correlation coefficient approaching 0.2. Nevertheless, 5 conductance relationships emerge across the selection levels. The most substantial relationship is seen for Leak versus NaP in the soma (**Figure 5**), and this emerges as a fairly notable positive correlation. Two other positive correlations of some note are detected in the soma (**Figure 5**): SKKCa versus Kd2, and SKKCa versus Leak. Furthemore, three negative correlations become apparent in the soma as well: CaT versus A, CaT versus BKKCa, and Leak versus A.

Figure 6 describes the same conductance relationship analyses for the neurite compartment. Again, we can see relationships emerging and strengthening across the levels of selection (**Figure 6, top**). Two relationships appear more prominently in the neurite: a positive correlation between Leak and NaP, and a negative correlation between the two calcium conductances – CaS and CaT (**Figure 6, bottom**). Of note, Leak and NaP emerges as the strongest relationship in both the neurite and the soma compartments.

Finally, we comprehensively compare conductance relationships across compartments, to determine whether there may be co-regulation of membrane conductances between the soma and neurite. **Figure 7** shows a comprehensive view of the conductance data in both compartments at selection level 3. In this visualization, we can see the distribution of each conductance along the diagonal, as well as the raw scatterplots of the 515 neurons at this level of selection. In addition to visualizing the raw data for the relationships in **Figures 5 and 6**, we see two strong relationships emerge across compartments: NaPSOMA versus NaPNEURITE, and LeakSOMA versus LeakNEURITE.

Ion Channel mRNA correlations relative to model relationships

To determine whether the relationships seen among model neuron conductances may have independently arisen as necessary for appropriate output, we wanted to compare these results with a biological data set. Because it is difficult or impossible to comprehensively measure membrane conductances in biological neurons, we performed an analysis on levels of the mRNAs that encode the channels most directly responsible for membrane conductances that are represented in our model neurons. Using single-cell qPCR, we quantified 12 different channel mRNAs from 40 individual crab LC motor neurons (**Figure 8**).

While we are unable to disentangle mRNAs for channels that will be localized to the soma versus those that will be in the neurite, we feel the mRNA data are best compared with the somatic conductances in the model. The channel mRNAs reveal some very intriguing relationships. First, there is widespread correlation among mRNAs, and of considerably high correlation coefficients (**Figure 8**). Further, every correlation is a positive correlation. However, some of the most profound relationships bear striking similarity to those seen in the model. For example, NALCN and IRK are putatively related to the model conductances NaP and Leak respectively. NaP and Leak was the strongest correlation seen in the soma compartment and is a very tight correlation in biological cell mRNA as well (**Figure 8**). Furthermore, the four other strongest correlations found in the soma compartment of the model (CaT/A, Leak/A, SKKCa/Kd2, and SKKCa/Leak) reflect some of the strongest mRNA correlations in their biological channel counter parts as well (see **Figure 8**; CaV2/Shaker, IRK/Shaker, SKKCa/Shab-Shaw1-Shaw2, and SKKCa/IRK respectively). Thus, while the overall quantitative level of correlation differs, it is striking that the most tightly correlated mRNA relationships correspond well to the strongest model conductance correlations in the soma.

4.4 DISCUSSION

We report a morphologically enhanced biophysical model of the LC of *Cancer Borealis* that is, for the first time, informed completely by measured properties of the same cell. Consistent with available biological data from our Lab and the literature, we propose a three-compartment model of the LC that, for the first time, includes an SIZ compartment. The study also provides hitherto unknown structure-function insights related to the functioning of the crustacean cardiac ganglion, including the differential roles of active conductances in the three compartments.

An intact model network generated from consistent experimental data

Computational models of the crustacean cardiac ganglion rely on experimental data from multiple organs (e.g., stomatogastric ganglion) and species (e.g., lobster) for passive properties and conductance ranges. For the present model, the experimental data were obtained from the LCs of intact networks recorded from the Schulz lab, as well as SIZ recordings to first match our model with the known data, and then to explore the functional characteristics in search of an explanation for the preservation of output across a wide variation range. We started with a prediction of the intact single cell morphology that integrates information about structure and proposed a methodology to validate it. Specifically, although an SIZ has been conjectured as the source of SC input into the cardiac ganglion reported single cell models have not explicitly considered such morphology. For instance, models of single LCs have typically considered only the soma compartment and possible a neurite attached to it. To validate our expanded three-compartmental that includes an SIZ, we estimated the SC frequency ranges from intact recordings and then found that a model that accounted for the biological data was able to successfully reproduced intact single cell responses (**Fig.2G**).

Model predicts active conductances in neurite and their specific functions

The proposed intact LC single cell model structure with a neurite and SIZ that received the SC input provided a framework to integrate experimental data related to LC input and output and explore underlying mechanisms. Specifically, the input to the LC arrived at the SIZ and were ranges of frequency and temporal profiles of SC spike trains delivered at the SIZ via synapses (**Fig. 1**), and the output was the membrane potential fluctuation of the LC soma that in turn controlled the synchronization of spikes at the SIZ. Using a three-stage rejection protocol to select the conductances in an unbiased manner, the procedure predicted that active conductances were necessary in the neurite to reproduce experimental input-output data for an LC.

The observation that excessive leak in the neurite was the cause of a passive neurite causing reduction in depolarization of the soma membrane potential, led to the consideration of Nap and/or CaS and CaT channels to counter the leakage. As shown in results, I_Nap and not I_CaS or I_CaT helped offset the effects of leak current in the neurite (**Fig. 2B, D**). An analysis of the time constants of the currents revealed that I_Nap had a time constant that was at least four-fold lower than that of I_CaT and at least 14-fold lower than that of I_CaS in the -50 to -20 mV range (**Fig. 6**). Since the membrane voltage of the soma never exceeded 0 mV, the time constant (during all model runs) of the I_CaT was always at least twice as large as that of I_Nap, and that of I_CaS was always larger than of I_CaT. However, I_CaT and I_CaS were continuously active and strengthened I_BKKCa as seen by comparing the traces in **Fig. 2D, E**.

Emergent conductance correlations in the multicompartmental network model

One of the key hypotheses that this work tests is whether network level selection criteria will result in a population of models in which conductance correlations emerge. The collective literature in two similar crustacean networks (stomatogastric and cardiac ganglia) are somewhat inconsistent in this result. Previous work of the Nair Lab in the cardiac ganglion LCs (Ball, Franklin) with a similar rejection sampling approach yielded strong correlations in the LC soma among two pairs of conductances: CaS-A and CaT-Kd. These data reveal that such relationships can emerge naturally from a selection process focused on output characteristics informed by biological data. However, those results were limited to models of the soma only and based on a different species and different mode of activity (driver potentials) than the cells modeled in our study. Further, there was relatively little biological data available at the time for those experiments, and so ultimately our interpretation of these first models is that such relationships are theoretically possible to detect and quantify – but further study was needed, including more thorough grounding in biological data as well as model neurons that better reflect the morphological complexity (i.e., multiple compartments) of biological neurons.

Conversely, a thorough and extensive analysis of a multicompartment model employing a large population of LP neurons from the crustacean stomatogastric ganglion yielded a different outcome. Taylor et al. (2009) utilized a large population selection approach, in a multicompartment model, and selected based on output characteristics that focused both on the single cell excitability as well as some features reminiscent of network level function (i.e., output as a result of synaptic input currents). In this study, they found only weak correlations among conductances – both within and across the compartments (Taylor et al. 2009). Thus, our current work employs a much more similar approach to Taylor et al., but in the system originally modeled by previous Nair Lab members – the cardiac motor neurons – in which we had seen such correlations. When we combined a multicompartmental model, far more extensive firsthand biological data, and a more developed network level selection process, our results in this study were largely consistent with those of Taylor et al. (2019). That is, while we could detect some emergent correlations within and across model neuron compartments, these were overall weaker correlations (rho-values between -0.2 and +0.2).

There are (at least) two overall interpretations of these results. First, that the intrinsic conductance correlations found in biological neurons across a wide range of nervous systems are not fundamentally necessary to generate baseline functional output of neurons. In other words, while these relationships may confer some adaptive advantage to neuron and network stability, and implicate compensatory relationships involved in homeostatic regulation they are not in and of themselves fundamental to the solutions capable of producing a given output of a neuron in a network. However, we also interpret these results from a cautionary perspective. Taken together, the work of the Nair Lab shows that conductance correlations emerge in more narrowly constrained models with clear input-output relationships (Ball, Franklin). However, as we add more free parameters to the system for which we have less knowledge of biological constraints – in this case multiple compartments and conductances therein, as well as synaptic inputs and network connectivity – we may lose the ability to detect fundamental relationships in biological neurons. If this is the case, then we predict that as more complex models become better informed by biological data, the possibility to recapitulate and interrogate these relationships may be more robust.

A more generous interpretation of the correlations found in the model would be that it is significant that such relationships can be detected at all given the conditions of the model experiment. Given that we had no biological data from which to inform the neurite compartment modeling, that the input-output relationships of LCs across individuals can be highly variable in biology, and that the network connectivity and synaptic drive from the pacemaker neurons had to be entirely inferred from the literature, we might predict that such levels of uncertainty would make it nearly impossible to expect biological relationships to emerge. Yet even though the correlation coefficients are somewhat weak, there is a clear constraint on conductances that emerge towards their correlated levels and several relationships are detectable as "signal above the noise." Most provocative is the fact that the model conductance relationships we detect most clearly are reflected as some of the most strongly correlated biological relationships at the level of channel mRNAs. While it would be inappropriate to overinterpret such disparate modalities of data (biological channel mRNAs are a long way removed from model membrane conductances), this provides some encouragement that better biological constraints to inform models going forward may recapitulate more strongly the relationships seen in biology. This will further allow computational modeling to be a critical test bed for the nature of these relationships and how they influence output and stability in neural networks.

4.5 CONCLUSION

We utilized a novel three-compartmental biophysical model of an LC that is morphologically realistic and includes provision of inputs from the SCs. The proposed single cell model facilitated incorporation of additional experimental observations related to both the SIZ compartment responses and to the presence of active conductances in the neurite compartment.

Furthermore, the overall network model provided a framework to integrate this single cell information into a network and explore how it impacted and reproduced experimental observations at the network level. The model provided novel predictions of the differential roles of conductances in the neurite and the soma, and insights into the role of specific current channels in the neurite. The model also reproduced the varied responses seen experimentally and predicted the calcium currents in the neurite to be the underlying cause. Finally, we investigated whether conductance relationships would emerge from the selection process that would give insight into the biological function of these interactions, as well as allow us to make inferences about the fundamental nature of such relationships in biological neurons. While we did detect some correlations among conductances within and across compartments, these were overall weaker relative to our previous work and that reported in the biological literature. We suggest that either such conductance relationships are not fundamentally necessary to generate a given output, or that much greater constraints on the free model parameters are needed to recapitulate these biological relationships. Overall, these predictions and the reasons why the LCs exhibit varied TEA responses are topics for future research.

4.6 TABLES

Table 1. Ranges of properties for selecting valid LCs

Parameter	Min	Max
Vrest	-53 mV	-39 mV
Rin	0.852 MΩ	13.3 MΩ
Tau	7.3 ms	24.5 ms
VPeak_PreTEA	7.95 mV	33.76 mV
Area_PreTEA	2867 mV.ms	18373 mV.ms
Area_PostTEA	5178 mV.ms	36853 mV.ms

Table 2. Maximal conductance ranges

Current	G_min (S/cm2)	G_max (S/cm2)
CaT	0.00016	0.00031
CaS	6.50E-05	0.00013
CAN	7.00E-05	1.50E-04
NaP	3.50E-05	2.30E-04
Leak (All Segments)	6.20E-05	9.70E-04
KA	0.000172	0.0019
Kd (Kd1)	0.000165	0.00127
KCa	0.00079	0.0061
SKKCa	0.00088	0.002
Kd2	0.000091	0.0005

Table 3. Ranges of connective and input parameters used in Stage 2&3 rejection

Parameter	Min	Max
Exp2Syn Tau1	10 ms	
Exp2Syn Tau2	60 ms	
Exp2Syn reversal potential	-15 mV	
NetCon weight	0.01	0.1
NetStim spiking frequency	16Hz	32Hz
NetStime noise level	0.8	

LocalGap R	1 MΩ	
InterGap R	1MΩ	15 MΩ

Table 4. Model Current Parameters

I_{ion}	x^p	x_∞	τ_x (msec)
I_A	m^3	$\frac{0.3463}{1+0.008685e^{-\frac{V}{5.033248}}}+\frac{0.75187}{1+1.11022e^{-\frac{V}{9.610637}}}+0.162947$	$3.002+\frac{4.073}{1+\exp((V+24.18)/2.592)}$
	h	$\frac{0.93854475}{1+144209.656e^{\frac{V}{5.08660603}}}+0.02804584$	$9.434+\frac{11.7}{1+\exp((V+1)/5.317)}$
I_{CaS}	m^2	$\frac{1}{1+\exp((V+24.75)/-5)}$	$20+\frac{50.2}{\exp((V+20.25)/1)}$
	h	$\frac{45}{40+[Ca^{2+}]}$	$\frac{1}{0.02}$
I_{CaT}	m	$\frac{1}{1+\exp((V+20)/-1.898)}$	$18.51-\frac{3.388}{\exp((V-6.53)/9.736)+\exp((V+12.39/-2.525)}$
	h	$\frac{1}{1+\exp((V+55.27)/6.11)}$	$20.23+\frac{40}{\exp((V+23.48)/-9.976)+\exp((V+5.196)/10.84)}$
I_{Kd}	m_1^4	$\frac{1}{1+\exp((V+24.19)/-10.77)}$	$25.049+\frac{25}{1+\exp((V+25.84)/6.252)}$
	h_1	$0.3+\frac{1-0.3}{1+\exp((V+15.87)/5.916)}$	$550+\frac{954.9}{\exp((V+10.8)/-15)}$
	m_2^4	$\frac{1}{1+\exp((V+23.32)/-10)}$	$100+\frac{550}{\exp((V+15)/12.46)}$
I_{NaP}	m^3	$\frac{1}{1+\exp((V+32.7)/-18.81)}$	$3.15+\frac{0.8464}{\exp((V+0.8703)/-6.106)}$
I_{CAN}	w	$(0.0002*[Ca^{2+}]\verb|^|2/(0.0002*[Ca^{2+}]\verb|^|2+0.05))$	$(40\ /\ (0.0002*[Ca^{2+}]\verb|^|2+0.05))$
$I_{\mathrm{SK(Ca)}}$	w	$(0.0001*[Ca^{2+}]\verb|^|2/(0.0001*[Ca^{2+}]\verb|^|2+0.1))$	$(4\ /\ (0.0001*[Ca^{2+}]\verb|^|2+0.1))$
$I_{\mathrm{BK(Ca)}}$	a	$\frac{[Ca^{2+}]}{(1+\exp((V-15+0.08*[Ca^{2+}])/-15)*(1+\exp((V+5+0.08*[Ca^{2+}])/-9)*(2+[Ca^{2+}])}$	$\frac{1}{0.4}$
	b	$\frac{7}{5+[Ca^{2+}]}$	$\frac{1}{0.2}$

Table 5. Ranges of waveform properties for selecting valid intact cells

Parameter	Min	Max
Spike number per burst	4	8
Avg LC spiking frequency	4 Hz	8 Hz
VPeak_PreTEA	7 mV	30 mV
Area_PreTEA	2867 mV.ms	18373 mV.ms
Spike number per burst Post TEA	>1.13 x PreTEA SPB	none
AVG LC spiking frequency	>1.21x PreTEA frequency	none
VPeak Post TEA	>1.3x PreTEA Vpeak	none
R^2 synchrony LC3 to LC5 control	0.95	1.0
R^2 synchrony LC3 to LC5 in TEA	0	0.89

Table 6. Ranges of waveform and synchrony properties for selecting valid networks

Parameter	**Min**	**Max**
Spike number per burst	4	8
Avg LC spiking frequency	4 Hz	8 Hz
VPeak_PreTEA	7 mV	30 mV
Spike number per burst Post TEA	>1.13 x PreTEA SPB	none
AVG LC spiking frequency	>1.21x PreTEA frequency	none
VPeak Post TEA	>1.3x PreTEA Vpeak	none
R^2 synchrony LC3 to LC5 control	0.95	1.0
R^2 synchrony LC3 to LC5 in TEA	0	0.89

4.7 FIGURES

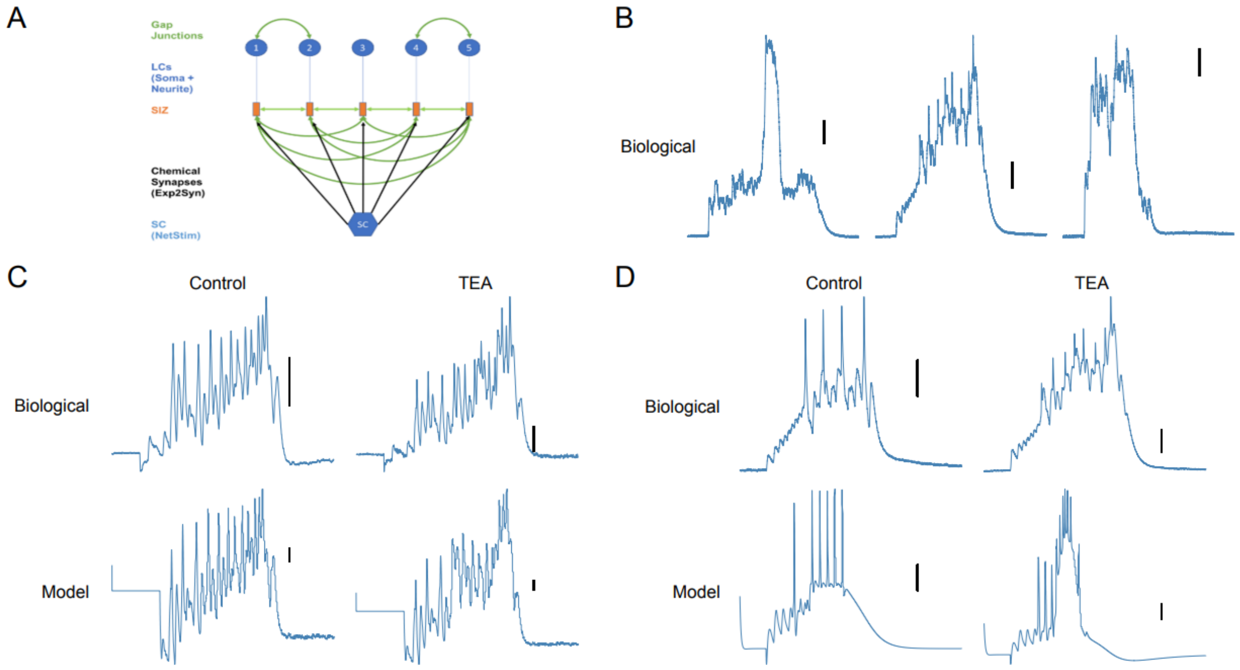

Figure 1. Morphologically realistic model of intact LC reproduces experimental data. (A) Model network. Gap Junctions are formed between LC1-2 and LC4-5. Gap Junctions modeled between SIZs using the same fixed conductance value with SC input to each SIZ. (B) Variability in experimental TEA responses from our lab. (C) Experimental stimulus protocol response of ligated cell in control and TEA conditions. Corresponding model responses are shown below the plots. (D) Same plots as in panel C, but for intact cells.

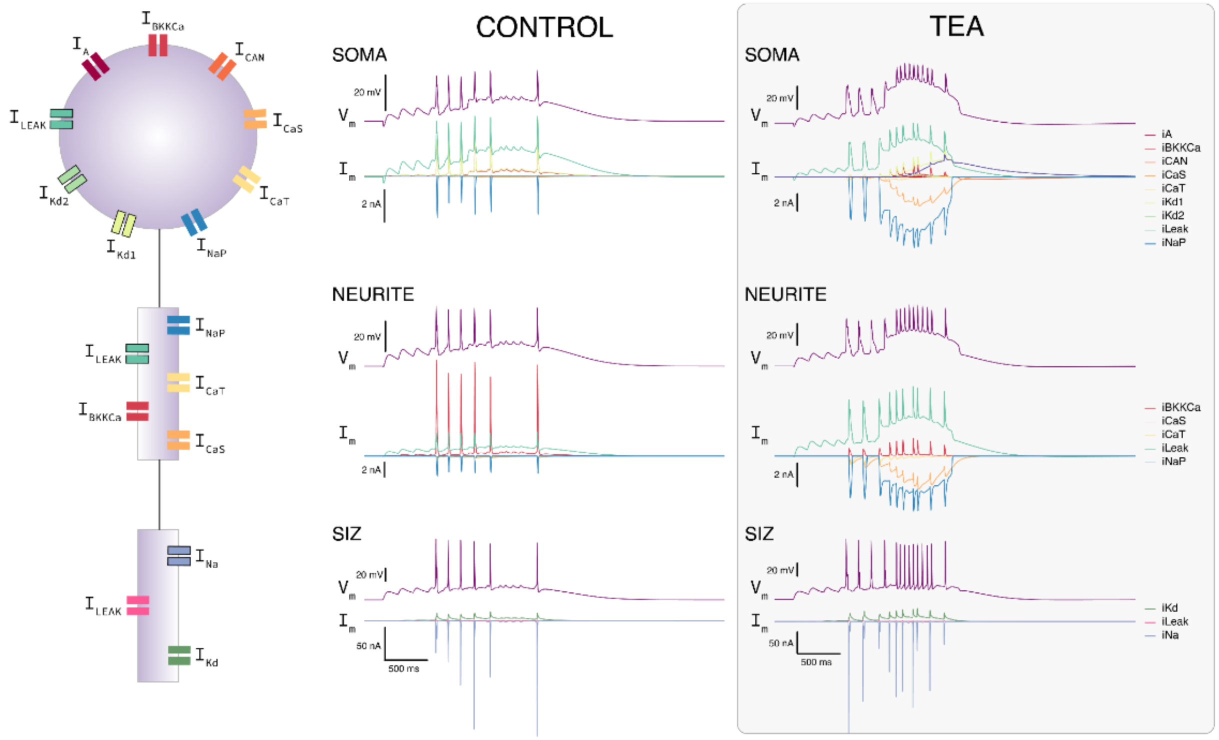

Figure 2. Model predicts presence and roles of active conductances in neurite.

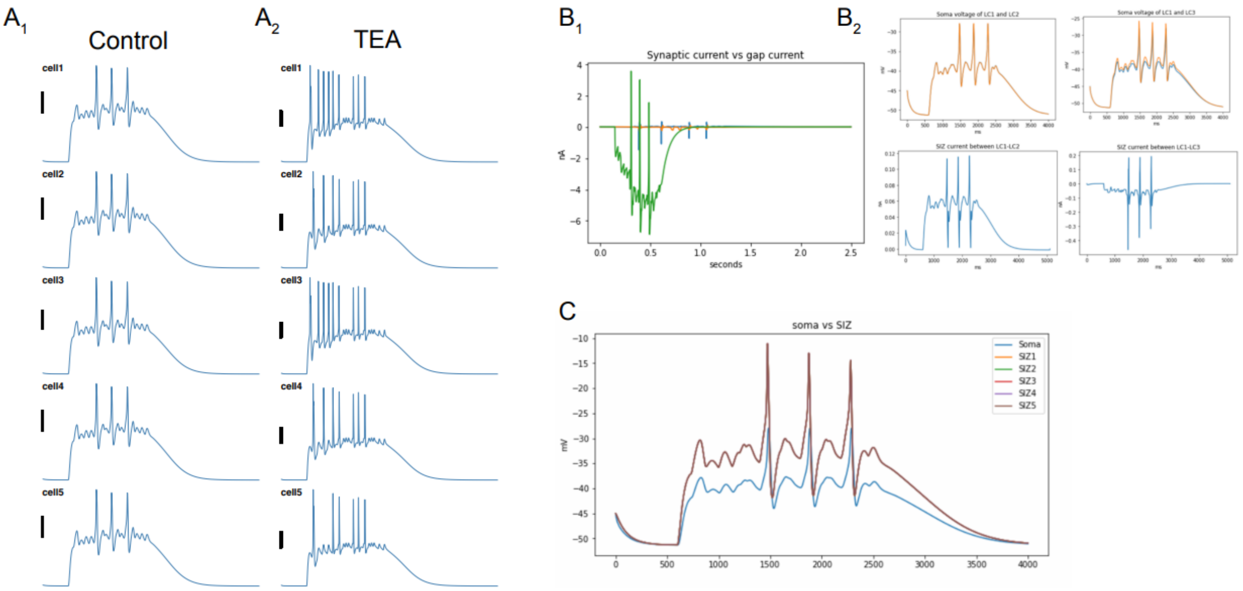

Figure 3. Voltage traces from the somas of each cell before and after being placed in the network. (B1) Current traces of the total synaptic current and the total Gap junction current. (B2) Soma voltage(top) and SIZ currents (bottom) between LC1-LC2 (left panel), and LC1-LC3 (right panel). These voltage and current traces show that the soma voltages can be different while the SIZ voltages can be the same, because the gap junctions in the SIZ are not the only gap junctions in the network; the soma gap junctions also allow compartment equilibrium to be

established between two somas. (C) Voltage traces showing the attenuation in spike amplitude for the control case. This is from LC6, from the network in 5A, and the SIZ membrane potentials for all the cells in the network, which are identical.

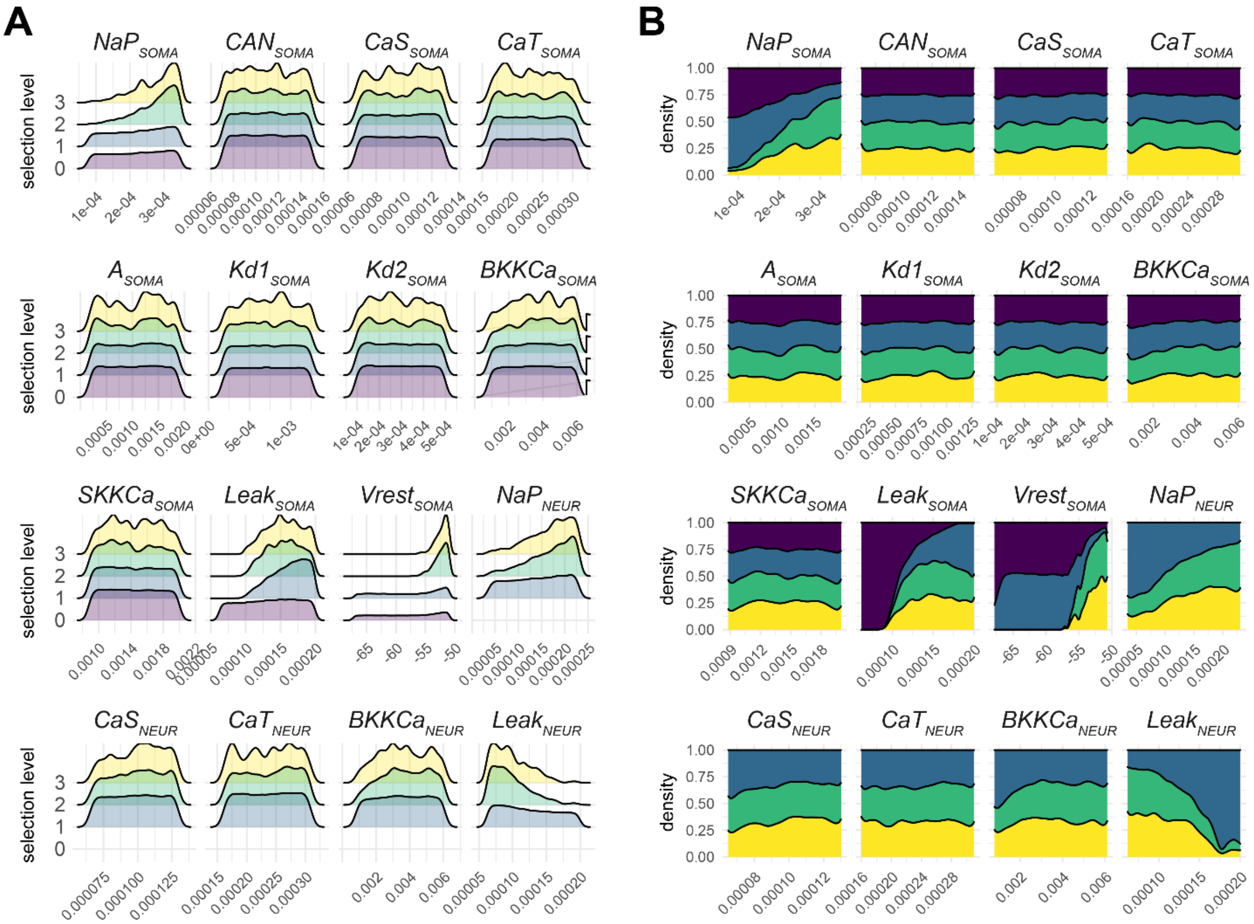

Figure 4. Conductance distributions after selection of soma and neurite model conductances. A.) Distribution of the conductances of models spared each level of selection; those selected on by the next level's criteria. Each selection level (0, 1, 2, 3) represents the conductances that passed that level with the level 0 being those that were initially generated and level 3 being those which satisfied all criteria. Each level's density plot is scaled independently. Because selection level 0 is performed on isolated somata, there are no conductances represented at this level for the neurite compartment. B.) Stacked density plots showing the subset of filtered at each level of selection. Four different levels of selection are shown (purple = 0, blue = 1, green = 2, yellow = 3). Each selection level (0, 1, 2, 3) represents the conductances of models that passed that level of selection, but not the subsequent – with the exception of level 3, which shows those that were preserved through all levels of selection. This indicates for a given conductance value which level of selection is most frequent.

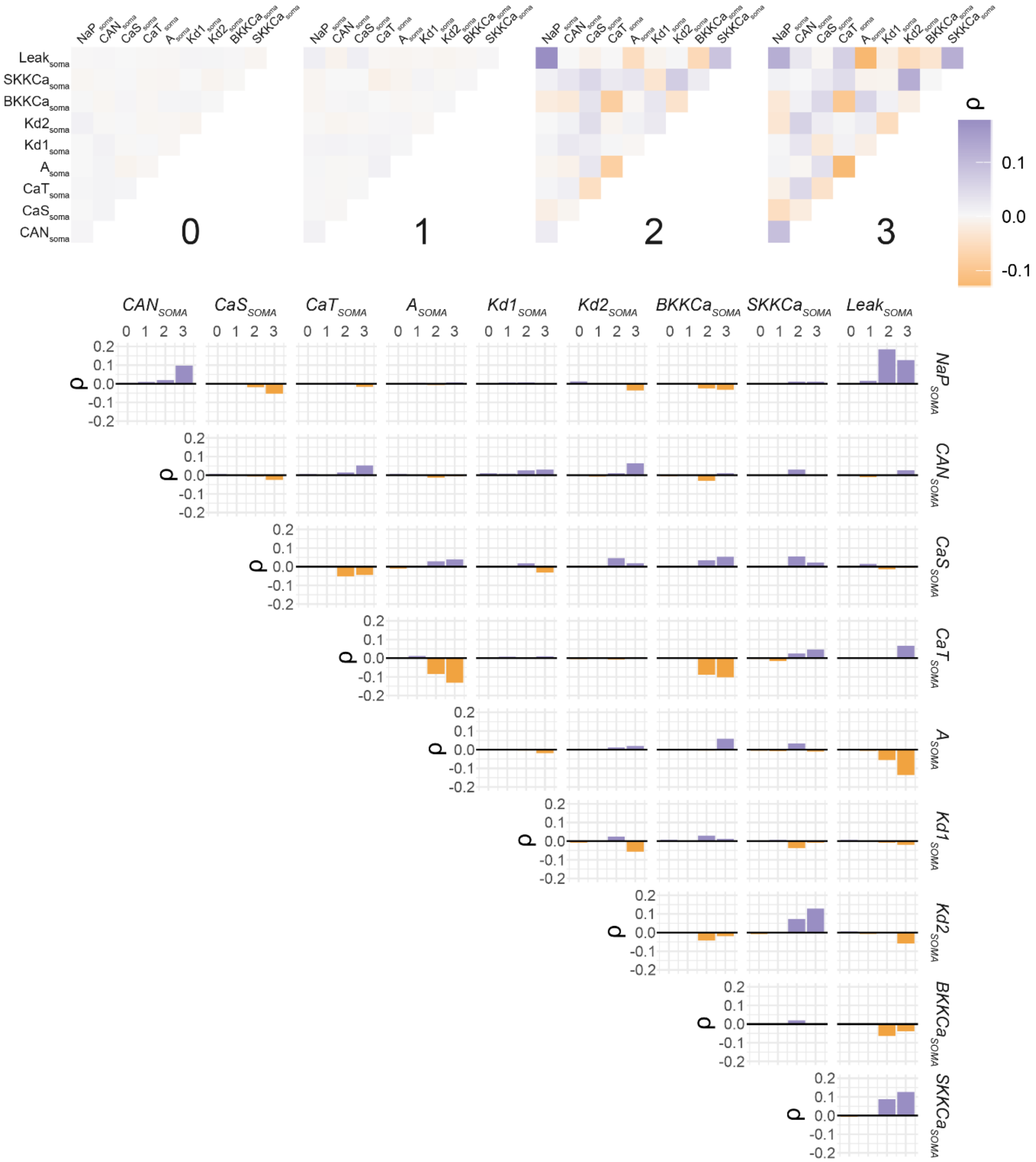

Figure 5. Conductance correlations in the soma compartment of model neurons across selection levels. TOP) Correlograms for four levels of selection (0-3) conductances in the somatic compartment of selected model neurons. Each pairwise correlation was calculated using Spearman's correlation and reported as rho values. These plots demonstrate that correlations become more pronounced across subsequent levels of selection. BOTTOM) Bar plot showing the rho-value of each pairwise correlation across levels of selection. These are the same data plotted in the top row but allow for more precise determination of the more pronounced correlations.

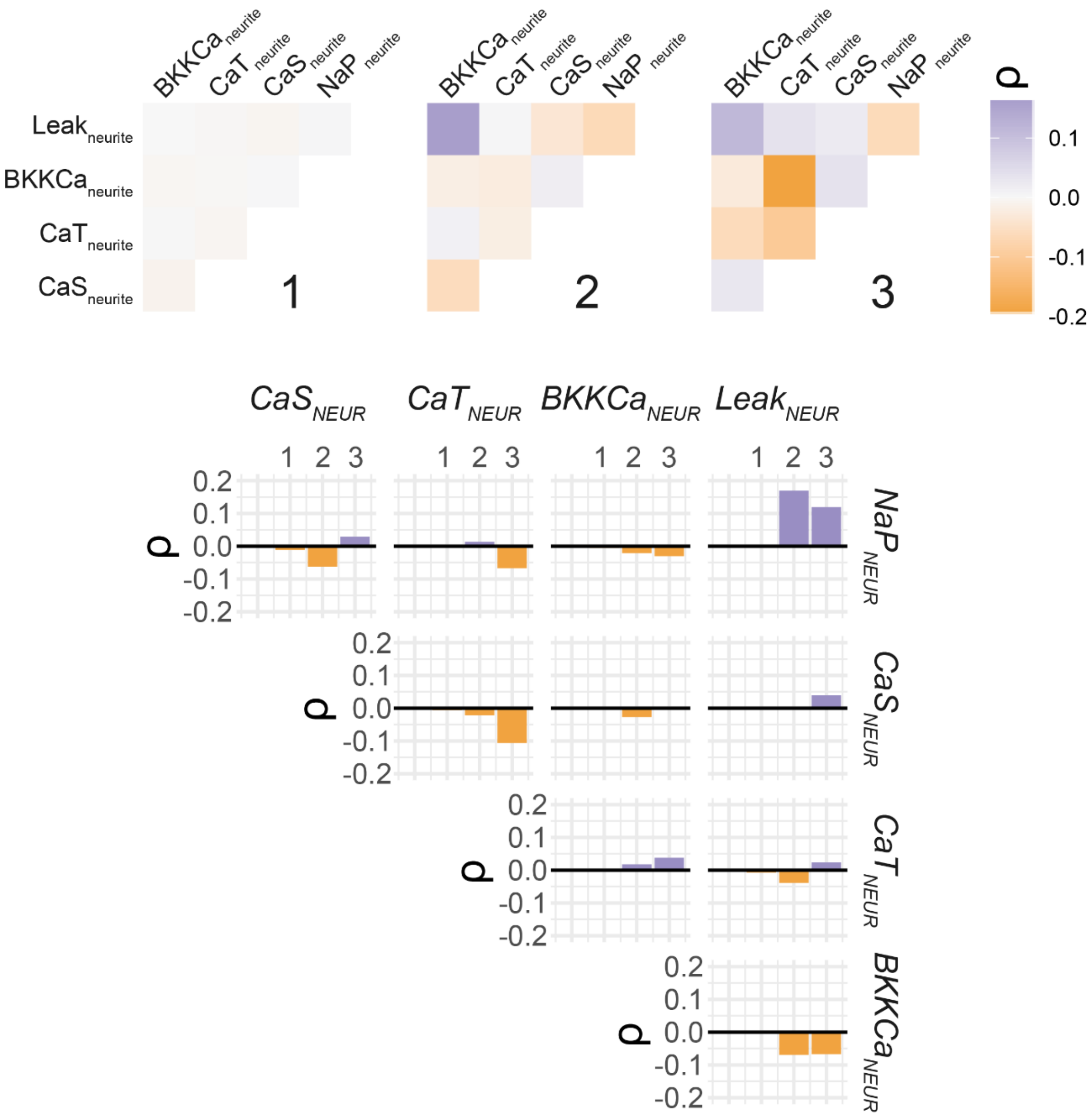

Figure 6. Conductance correlations in the neurite compartment of model neurons across selection levels. (TOP) Correlograms for three levels of selection (1-3) conductances in the neurite compartment of selected model neurons as described in the previous figure. (BOTTOM) Bar plot showing the rho-value of each pairwise correlation across levels of selection. These are the same data plotted in the top row but allow for more precise determination of the more pronounced correlations.

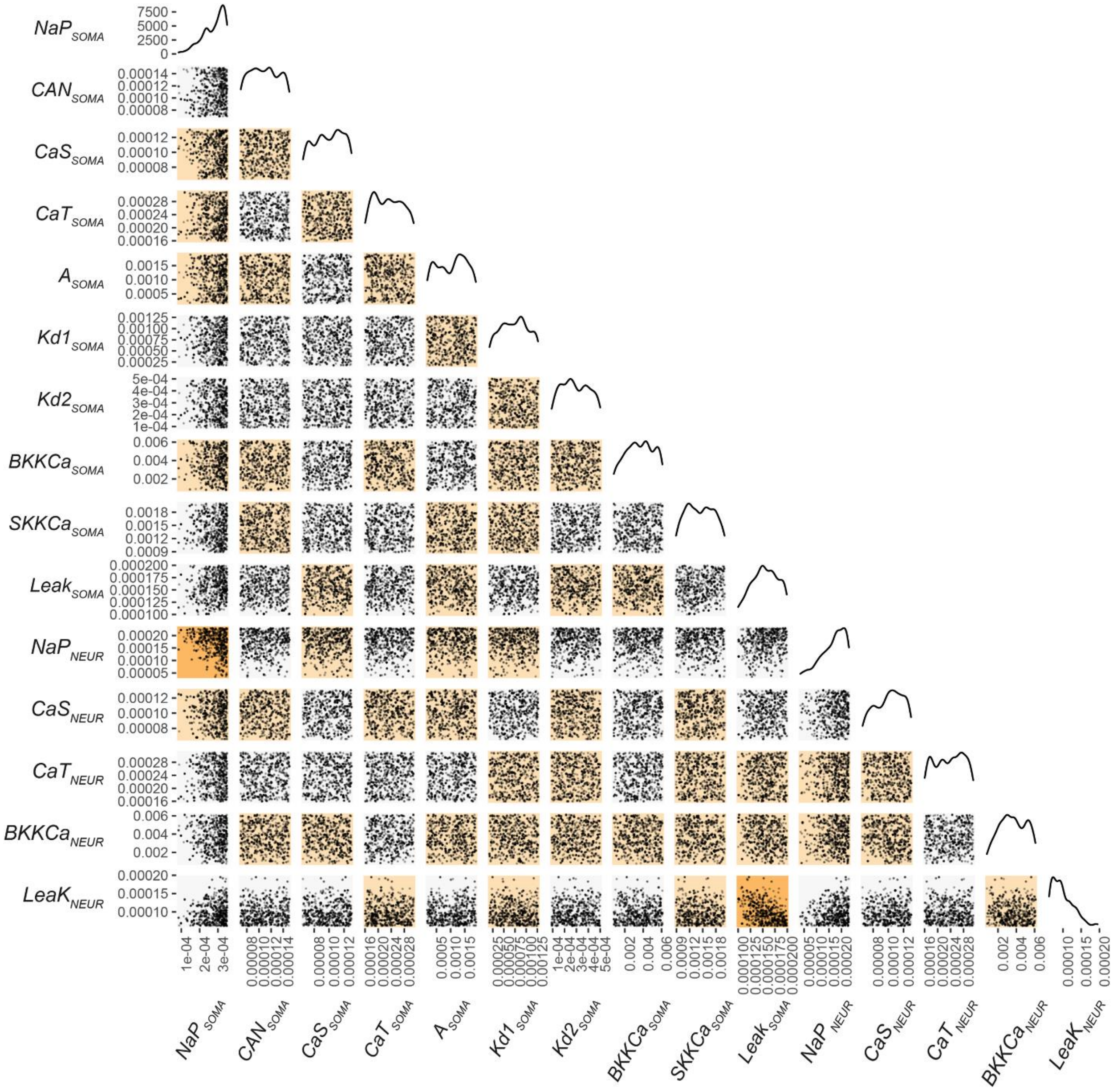

Figure 7. Scatterplots for pairwise relationships among soma, neurite, and across compartment conductances in models of selection level 3. Each dot represents a single model and its values for a given pair of conductances. Along the diagonal are curves that represent the distribution of values for a given conductance as keyed along the bottom axis. Stronger correlations are noted by the increasing intensity of background color for each pairwise relationship.

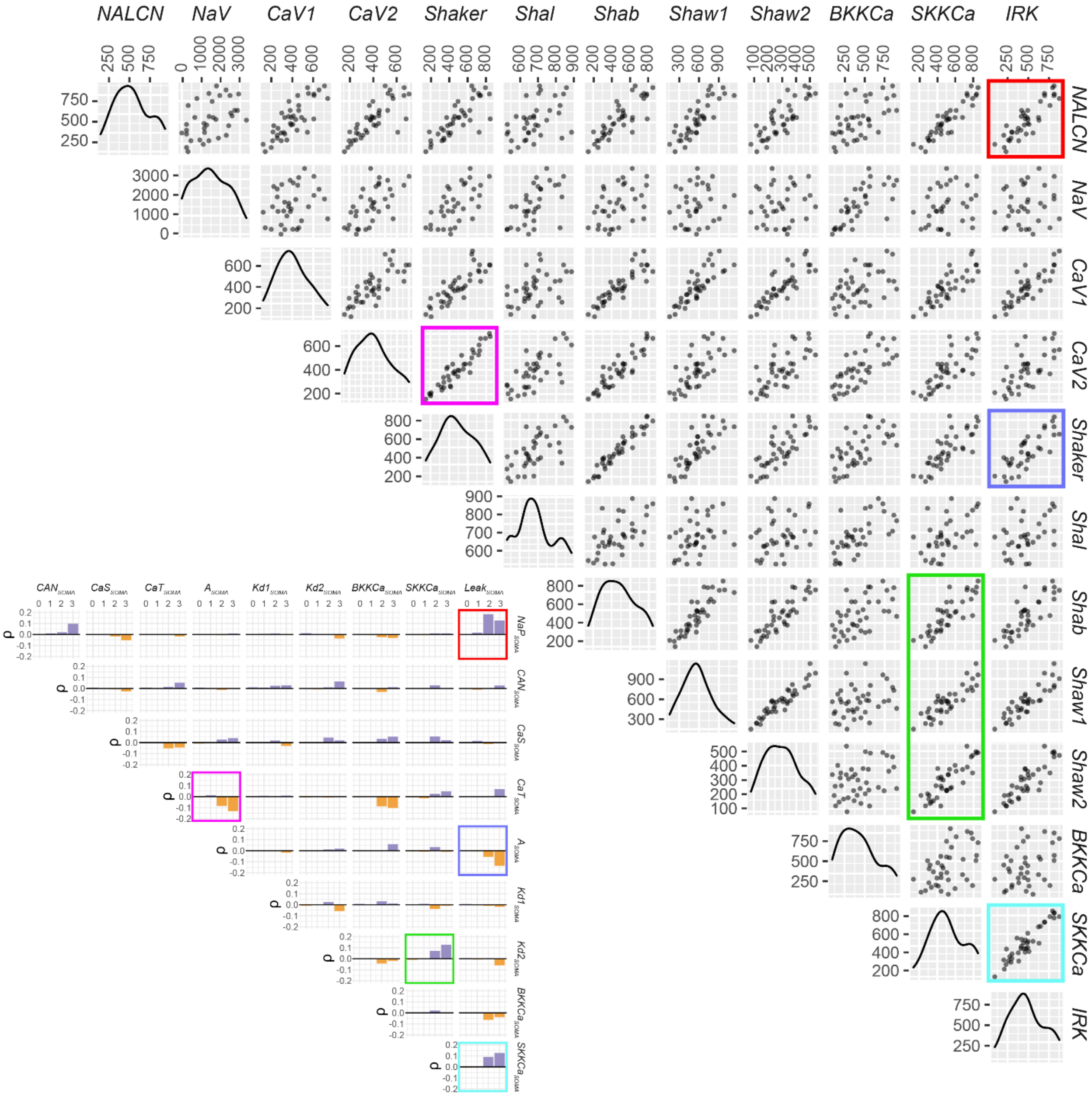

Figure 8. Scatterplots for pairwise relationships among channel mRNAs in biological LC motor neurons. Each dot represents a single model and its values for a given pair of channel mRNAs. Along the diagonal are curves that represent the distribution of values for a given conductance as keyed along the top axis. Stronger correlations that were identified in selection levels 2 and 3 in the soma of model neurons are noted by the colored box corresponding to the channel mRNAs most likely to encode those conductances.

4.8 REFERENCES

1. Marder E (2011) Variability, compensation, and modulation in neurons and circuits, Proc Natl Acad Sci U S A 108 Suppl 3, 15542-15548. PMC3176600.
2. Prinz AA, Billimoria CP, Marder E (2003) Alternative to hand-tuning conductance-based models: Construction and analysis of databases of model neurons, J Neurophysiol 90, 3998-4015.
3. Goaillard JM, Taylor AL, Schulz DJ, Marder E (2009) Functional consequences of animal-to-animal variation in circuit parameters, Nat Neurosci 12, 1424-1430. PMC2826985.
4. MacLean JN, Zhang Y, Goeritz ML, Casey R, Oliva R, Guckenheimer J, Harris-Warrick RM (2005) Activity-independent coregulation of ia and ih in rhythmically active neurons, J Neurophysiol 94, 3601-3617.
5. Khorkova O, Golowasch J (2007) Neuromodulators, not activity, control coordinated expression of ionic currents, The Journal of neuroscience : the official journal of the Society for Neuroscience 27, 8709-8718.
6. Schulz DJ, Goaillard J-M, Marder E (2006) Variable channel expression in identified single and electrically coupled neurons in different animals, Nat Neurosci 9, 356-362.
7. Schulz DJ, Goaillard J-M, Marder EE (2007) Quantitative expression profiling of identified neurons reveals cell-specific constraints on highly variable levels of gene expression, Proceedings of the National Academy of Sciences 104, 13187-13191.
8. Swensen AM, Bean BP (2005) Robustness of burst firing in dissociated purkinje neurons with acute or long-term reductions in sodium conductance, J Neurosci 25, 3509-3520. PMC6725377.

9. Marder E, Goaillard J-M (2006) Variability, compensation and homeostasis in neuron and network function, Nat Rev Neurosci 7, 563-574.
10. Tobin A-E, Cruz-Bermúdez ND, Marder E, Schulz DJ (2009) Correlations in ion channel mrna in rhythmically active neurons, PLoS One 4, e6742.
11. Ransdell JL, Nair SS, Schulz DJ (2012) Rapid homeostatic plasticity of intrinsic excitability in a central pattern generator network stabilizes functional neural network output, J Neurosci 32, 9649-9658.
12. Goldman MS, Golowasch J, Marder E, Abbott LF (2001) Global structure, robustness, and modulation of neuronal models, J Neurosci 21, 5229-5238.
13. Tobin AE, Van Hooser SD, Calabrese RL (2006) Creation and reduction of a morphologically detailed model of a leech heart interneuron, J Neurophysiol 96, 2107-2120.
14. Olypher AV, Calabrese RL (2007) Using constraints on neuronal activity to reveal compensatory changes in neuronal parameters, J Neurophysiol 98, 3749-3758.
15. Gunay C, Edgerton JR, Jaeger D (2008) Channel density distributions explain spiking variability in the globus pallidus: A combined physiology and computer simulation database approach, J Neurosci 28, 7476-7491.
16. Taylor AL, Goaillard J-M, Marder E (2009) How multiple conductances determine electrophysiological properties in a multicompartment model, The Journal of Neuroscience 29, 5573-5586.
17. Ball JM, Franklin CC, Tobin A-E, Schulz DJ, Nair SS (2010) Coregulation of ion channel conductances preserves output in a computational model of a crustacean cardiac motor neuron, J Neurosci 30, 8637-8649. PMC4473856.

18. Franklin CC, Ball JM, Schulz DJ, Nair SS (2010) Generation and preservation of the slow underlying membrane potential oscillation in model bursting neurons, J Neurophysiol 104, 1589-1602.
19. Olypher AV, Prinz AA (2010) Geometry and dynamics of activity-dependent homeostatic regulation in neurons, J Comput Neurosci 28, 361-374.
20. Marder E, Taylor AL (2011) Multiple models to capture the variability in biological neurons and networks, Nat Neurosci 14, 133-138.
21. Prinz AA, Bucher D, Marder E (2004) Similar network activity from disparate circuit parameters, Nat Neurosci 7, 1345-1352.
22. Lane BJ, Samarth P, Ransdell JL, Nair SS, Schulz DJ (2016) Synergistic plasticity of intrinsic conductance and electrical coupling restores synchrony in an intact motor network, eLife 5, e16879. PMC5026470.
23. Cruz-Bermúdez ND, Marder E (2007) Multiple modulators act on the cardiac ganglion of the crab cancer borealis, J Exp Biol 210, 2873-2884.
24. Ransdell JL, Nair SS, Schulz DJ (2013) Neurons within the same network independently achieve conserved output by differentially balancing variable conductance magnitudes, J Neurosci 33, 9950-9956.

APPENDIX

A.1 Computational model of a rodent Central Amygdala network

Amygdala is a key site of plasticity in auditory fear conditioning and plays an important role in both the acquisition and storage of fear and extinction memories (LeDoux 2000; Maren 2001; Pape and Pare 2010). The role of the amygdala in fear has been studied using a Pavlovian fear conditioning paradigm for rodents where a neutral stimulus (conditioning stimulus, CS), such as a tone, is paired with an aversive one (unconditioned stimulus, US), such as a foot shock. After only a few pairings, the previously neutral stimulus becomes aversive and can itself evoke an emotional reaction typically resulting in a freezing behavior. Even though there is consensus that the amygdaloid complex is a critical component of the mammalian fear circuit, the relevant interconnections among the amygdalar nuclei and their contributions to the acquisition and storage of fear and extinction memories are not well understood.

Our previous computational models investigated how different types of experimentally observed ‘fear’ cells emerge in the lateral amygdala (LA, the input station of the amygdala) after fear conditioning (Li et al., 2009; Kim et al., 2013). The present study investigates how experimentally reported fear responsive cells emerge in the output station of the amygdala, the Central amygdaloid nucleus (Ce), after fear conditioning. Specifically, we developed a biologically realistic computational model of the Ce region to reverse engineer its functioning, including how it integrates various inputs from other amygdalar nuclei and generates fear responses during a Pavlovian fear conditioning paradigm.

Single cell models

Biological information related to single cell models were obtained from the following sources: Currents – from our past models; Passive properties – Amano et al. (2012); Current injection plots - Amano et al. (2012)

Network Structure

The Ce network had 500 model cells distributed between CeL and CeM regions, as follows: CeL: 240 cells [54% (RF), 34% (LTB) and 12% (LF)] and CeM: 260 cells [27% (RS), 71% (LTB) and 2% (LF)] (Duvarci et al., 2011) CeL cells were further divided into two populations: PKCδ- (96 cells) and PKCδ+ (144 cells) (Haubensak et al., 2010).

Inputs

LA inputs to CeL: Modeled based on tone response data obtained from models and biology (Li et al., 2011). Spontaneous frequency of LA pyramidal cells (Fig. 2): 0.5 Hz (Habituation), 1 Hz (Post-FC), and 0.5 Hz (Ext). Six different LA cell responses each, for Fear, extinction-resistant and unresponsive cell types were modeled and used as inputs to the Ce network. BA inputs were created using experimental tone response data (Herry et al., 2008). Six different BA cell responses each for Fear, extinction resistant and no-response cell type were modeled and used as inputs to the Ce network. Inputs from ITC clusters: ITCv and ITCd inputs were modeled using data from Li et al. (Li et al., 2011). Six different ITCv and ITCd cells were modeled to provide input to the Ce network.

Connectivity

Lacking information about extrinsic and intrinsic connectivity for the model, for extrinsic connectivity, we started with 5% for connections from LA, ITC and BL inputs to CeL. This means, for instance, that an LA input had a 5% probability of connecting to a selected post-synaptic cell. For intrinsic connectivity, we started with 20% connectivity reported for ITC-ITC connections (Li et al., 2011). Both extrinsic and intrinsic connectivity numbers were then tuned to match the experimental responses and percentages of CeL-Off and CeL-On cells (Duvarci et al., 2011). For intrinsic probabilities, 85% of CeM projecting neurons in CeL were reported to be SOM- (PKCδ+) (Li et al., 2013). So, we assumed the connection probability from PKCδ+ to CeM to be 80% and from PKCδ- to CeM to be 1%. Since intrinsic connectivity within CeM is unknown, for simplicity, we have assumed no connectivity in the present version. Li et al. (2013) reported that EPSC amplitudes evoked by stimulation of LA were larger in SOM- (PKCδ+) cells compared to those in SOM+ (PKCδ-) cells. Thus, the weights for LA, BA inputs to PKCδ+ were higher than PKCδ-. All the connection probabilities and weights are summarized in **Table 1**.

Neuromodulation

Neuromodulation receptors (NM, presently only dopamine) were placed randomly on PKCδ+, PKCδ- and CeM cells, respectively, in the following percentages: 50%, 25% and 25%. Neuromodulators were present only during conditioning and extinction trials, at the following levels: none for 1st, 'low' for 2nd, and 'moderate' for conditioning trials 3-5; and 'moderate' for trials 1-2 of extinction.

Activity dependent synaptic plasticity

Long term synaptic plasticity was modeled using a Hebbian learning rule that used NMDA-based post-synaptic calcium concentration levels to implement LTP and LTD (Li et al., 2009). LA-CeL synapse has been reported to potentiate after fear conditioning (Li et al., 2013). Also, intrinsic plasticity has been hypothesized in connections from CeL-On to CeL-Off cells. Accordingly, the model presently has plasticity only in LA-CeL connections, and in connections from PKCδ- to both PKCδ+ and to PKCδ- cells, but not in the reverse direction. Short-term facilitation and depression were modeled in all extrinsic excitatory and inhibitory connections, respectively, based on information from other brain regions. Intrinsic connections did not possess any short-term plasticity. We used the synaptic thresholds from our previous models (e.g., Li et al., 2011) and adjusted them appropriately.

The iterative process

The connection probabilities, initial synaptic weights and thresholds for plasticity were tuned to reproduce the experimental observations related to (i) the number of CeL-On, CeL-Off cells and the increased firing seen in CeM cells after fear conditioning (Duvarci et al., 2011), (ii) the tone responses of CeL and CeM cells during the various phases (Duvarci et al., 2011), and (iii) potentiation of LA afferents to CeL-On cells (Li et al., 2013).

First, we varied connectivity, synaptic weights and plasticity thresholds, starting with the values indicated to match the number of CeL-On and CeL-Off cells. For tuning the number of CeL-Off cells during habituation, we focused on the fact that the number of CeL-Off cells do not change between habituation and conditioning. We tried to match the proportions of CeL-Off cells during habituation but doing so caused the number of CeL-On cells to increase during habituation and stay the same at the end of conditioning.

Key Findings

Baseline model

The baseline model reproduced biologically observations, as expected; spontaneous frequency for model cells was 2.34 ± 1.48 Hz for CeL and 1.43 ± 0.86 Hz for CeM. The model also reproduced the biologically observed proportions of cell types after fear conditioning. During habituation model exhibited 5% (12/240) CeL-Off cells as compared to 11% in biology. All the cells were of the PKC δ+ type. For CeL-On cells, model exhibited 5% (12/240) as compared to 6% seen in biology. Here nine cells were of PKC δ- type and three were of PKC δ+ type. At the end of conditioning, model had 6.25% (15/240; all PKC δ+) CeL-Off cells as compared to 9% seen in biology and 12.5% (30/240; 24 PKC δ- and 6 PKC δ+) CeL-On cells compared to 15% seen in biology. The model also exhibited 46.5% (121/260) of active CeM cells ($z>1.96$) as compared to 47% seen in biology. The model was then used to explore other characteristics that it was not tuned to reproduce. Remaining cells classification is provided in **Table 2**.

Relative contributions of amygdalar inputs to CeL and CeM

We wanted to see the individual roles of extrinsic input on the responses of Ce neurons. For this, we disconnected each of the inputs inputs one at a time and analyzed the responses in Ce (**Table3**). We found that removing LA connections changed the number of CeL-On and CeL-Off cells and reduced the number of potentiated CeM cells. Removal of all connections from BA did not have much effect on the responses of either CeL or CeM. Removing ITC connections had the largest effect on CeL responses (**Table3**). Inhibition from ITCd was essential for the formation of CeL-Off cells, since removal of ITCd inputs eliminated all CeL-Off cells.

Role of intrinsic connections from CeLPKCδ+ cells to CeM cells.

Experimental findings have shown that, inactivation of CeL; induced freezing (Ciocchi et al., 010) and silencing PKCδ+ neurons increased CeM activity (Haubensak et al., 2010) . To test this, we selectively removed a random 25%, 50% and 100% of PKCδ+ cell connections onto the CeM cells and tested the effect on CeM responses. **Table 4** lists the firing rates of CeM cells during CS-Off and CS-On periods for Habituation and Conditioning phases for the four conditions cited. CeM responses increased as more and more connections were removed. This result was expected and CeL inhibits CeM.

Table 1. Probabilities and initial weights for different connections in the Ce network model.

Type	Connection Name	Connection Probability	Initial Weight
Intrinsic	CeLPKCδ- to CeLPKCδ-	20%	3
	CeLPKCδ+ to CeLPKCδ+	15%	2
	CeLPKCδ- to CeLPKCδ+	30%	2
	CeLPKCδ+ to CeLPKCδ-	10%	2
	CeLPKCδ+ to CeM	80%	2
	CeLPKCδ- to CeM	1%	2
	CeM-CeM	No connections	--
	CeM to CeLPKCδ+	No connections	--
	CeM to CeLPKCδ-	No connections	--
Extrinsic	LA to CeLPKCδ-	5%	2.3
	BA to CeLPKCδ-	5%	2.7
	LA to CeLPKCδ+	1%	2.7
	BA to CeLPKCδ+	1%	2.7
	ITCd to CeLPKCδ-	25%	1
	ITCd to CeLPKCδ+	55%	6
	Shock to CeLPKCδ-	55%	8
	BA to CeM	25%	2.5
	ITCv to CeM	15%	1
	LA to CeM	No connections	--
	Shock to CeM	No connections	--
	Shock to CeLPKCδ-	No connections	--

Table 2. Proportions of CeL cell types based on activity in the model network.

	Cell Types	# of cells / %
HAB	CeL-On	12 (9 PKCδ- , 3 PKCδ+) / 6%
	CeL-Off	12 (all PKCδ+) / 5%
	CeL-Unresponsive	216 / 89%
	Potentiated CeM	4 / 1.5%
	Depressed CeM	0 / 0%
	CeM-Unresponsive	255 / 98.5%
COND	CeL-On	30 (24 PKCδ- , 6 PKCδ+) / 12.5%
	CeL-Off	15 (all PKCδ+) / 6.2%

	CeL-Unresponsive	195 / 81.3%
	Potentiated CeM	121 / 46.5%
	Depressed CeM	0 / 0%
	CeM-Unresponsive	139 / 43.5%

Table 3. Effect of disconnection of LA, BA and ITCd inputs on activity in Ce.

Input Blocked		Cell Types	# of cells / %
LA	HAB	CeL-On	10 (7 PKCδ- , 3 PKCδ+) / 4%
		CeL-Off	10 (all PKCδ+) / 4%
	COND	CeL-On	29 (23 PKCδ- , 6 PKCδ+) / 12%
		CeL-Off	15 (all PKCδ+) / 6.25%
		Potentiated CeM	53 / 20%
BA	HAB	CeL-On	6 (4 PKCδ- ,2 PKCδ+) / 2.5%
		CeL-Off	14 (1 PKCδ- , 13 PKCδ+) / 6%
	COND	CeL-On	29 (24 PKCδ- , 5 PKCδ+) / 12%
		CeL-Off	10 (all PKCδ+) / 4%
		Potentiated CeM	86 / 33%
ITC	HAB	CeL-On	4 (3 PKCδ- , 1 PKCδ+) / 2%
		CeL-Off	0 / 0%
	COND	CeL-On	7 (all PKCδ-) / 3%
		CeL-Off	0 / 0%
		Potentiated CeM	67 / 26%

Table 4. Average frequency of CeM cells**.**

% connections removed			Average firing frequency (Hz)
0% (Control)	HAB	CS-On	1.64
		CS-Off	1.43
	COND	CS-On	2.27
		CS-Off	1.48
25%	HAB	CS-On	2.64
		CS-Off	2.31
	COND	CS-On	3.34
		CS-Off	2.48
50%	HAB	CS-On	3.66
		CS-Off	3.40
	COND	CS-On	4.35
		CS-Off	3.60

100%	HAB	CS-On	6.06
		CS-Off	6.01
	COND	CS-On	6.60
		CS-Off	6.20

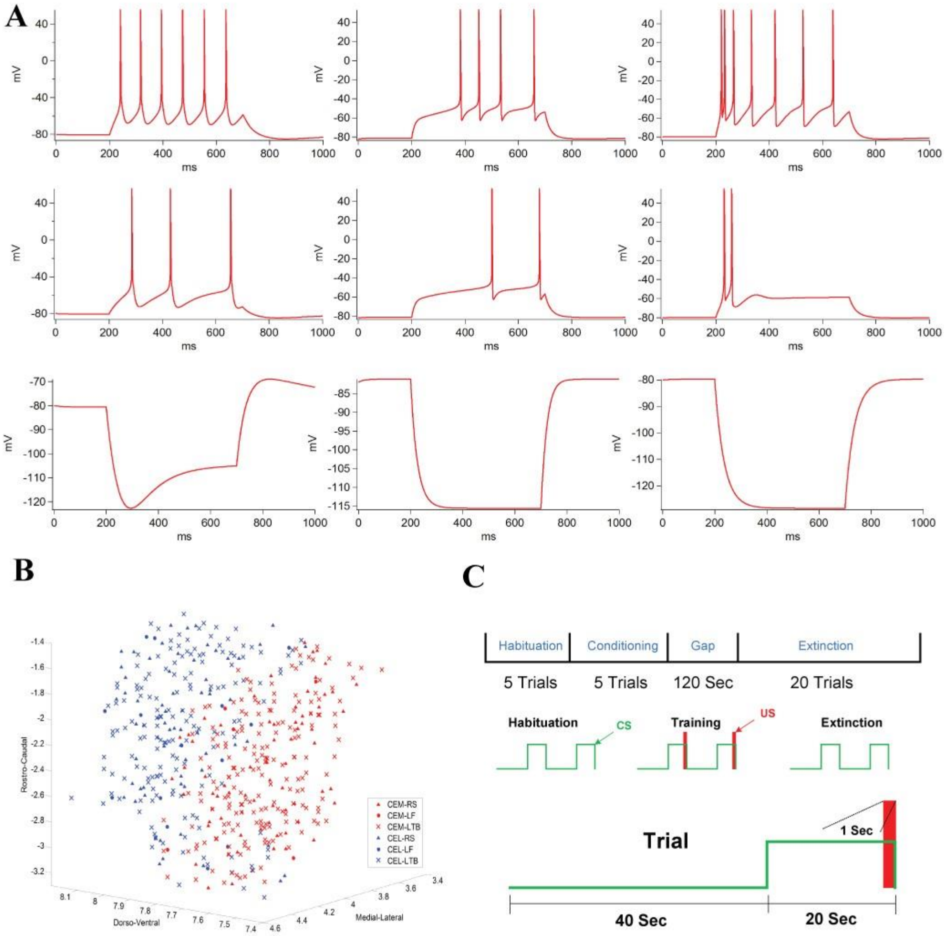

Figure 1. Details of the Ce network model: (A) Response of model Regular Spiking (RS, Left), Late Firing (LF, Middle) & Low Threshold Bursting (LTS, Right) cells to different current injection magnitudes (0.08, 0.045 and -0.1 nA for RS; 0.11, 0.1 and -0.1 nA for LF & 0.1, 0.06 and -0.1 nA for LTB). (B) Schematic of the 500-cell Ce model with 260 CeM cells (Red) &

240 CeL cells (Blue). Cells were randomly populated in specific regions identified as CeM and CeL/CeC in stereotactic coordinates. The three types of cells are randomly distributed in each region based on biological proportions. (C) Fear training protocol used in the model.

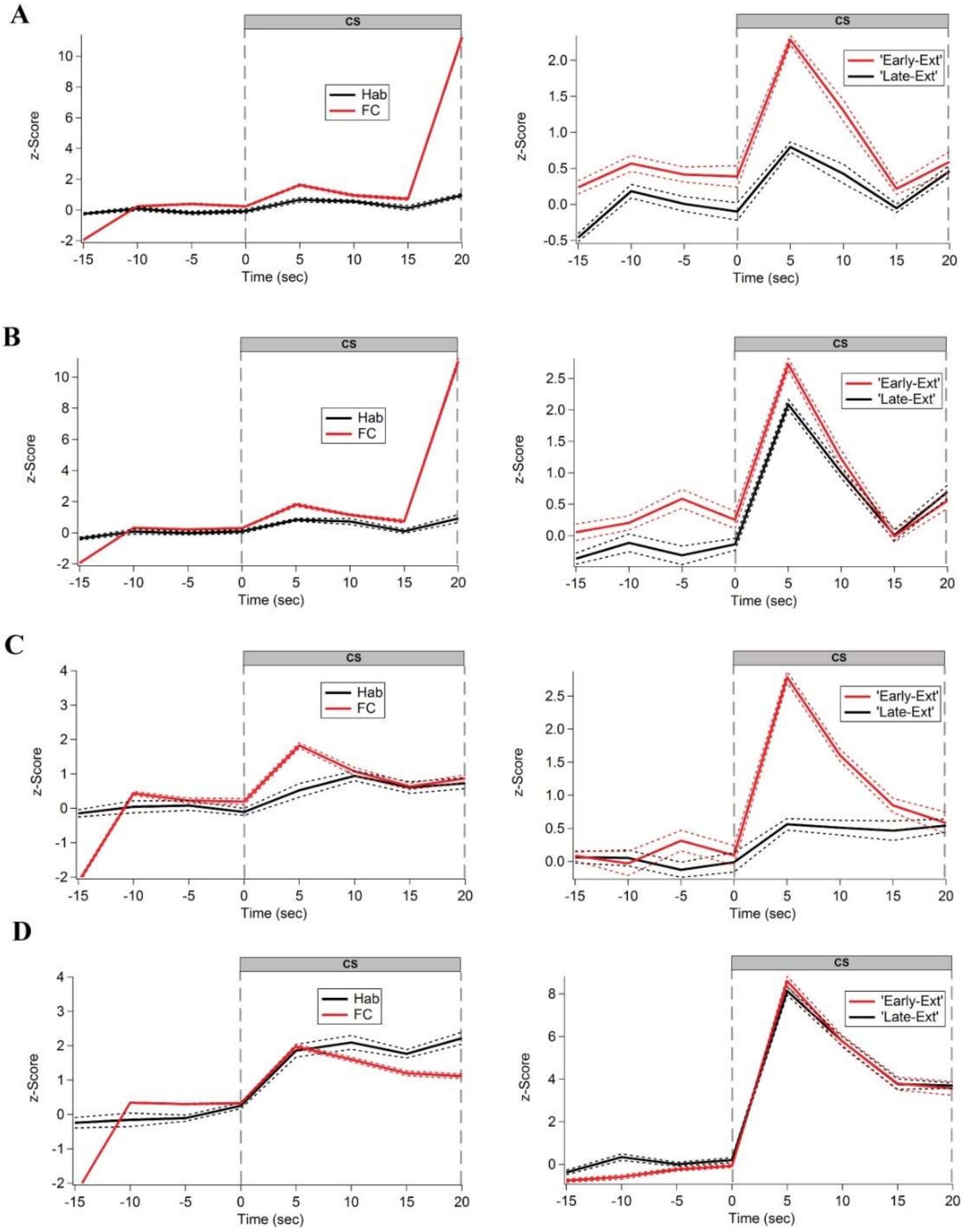

Figure 2. Tone responses of Ce afferents: (A) LAf; (B) LAer; (C) BAf, and (D) BAer cells during Habituation (1st-5th trials), Conditioning (4th & 5th trials) and Extinction (1st-5th & 16th-20th trials) phases. Responses shown as average of 5 sec bins, with -5 to 0 s bin response shown at 0, and so on.

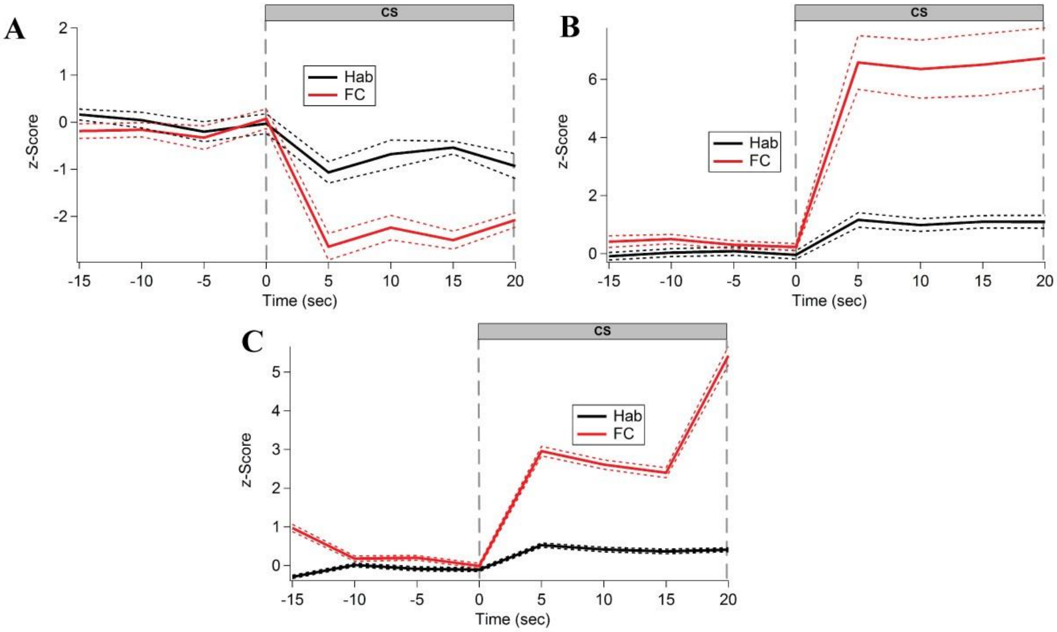

Figure 3. Model tone responses: Post-conditioning tone responses for CeL-Off (A) and (B) CeL-On cells, and of (C) potentiated CeM cells.

A.2 Amygdala Models, Chapter in Computational Models of Brain and Behavior

This chapter in John Wiley and Sons book, talks about the different computational models related to amygdala focusing on acquisition and expression of fear. Here, we suggest a way for creating biologically realistic models which can be used to complement experimental investigations and help in reverse engineering the mammalian fear circuit. We also provided a step-by-step guide to develop biologically based computational model using three different model types; a) Integrate and Fire, b) Izhikevich based and c) Hodgkin-Huxley based. My contribution to this chapter was in coming up with the step-by-step guide and also developing the LA modes using Izekevich equations. You can refer this chapter in the published version of the book *Amygdala Models (pg. 285-301).*

PUBLICATIONS

Refereed Journal and Conference Articles

- **Samarth P**, Dopp D, Kick D, Schulz D, Nair SS Morphological crustacean cardiac ganglion model reveals differential roles of conductances in compartments.
- Guntu V, Feng F, Alturki A, Nair A, **Samarth P**, Nair SS (2018) Amygdala Models, Chapter in Computational Models of Brain and Behavior, John Wiley and Sons.
- Lane BJ, **Samarth P**, Ransdell JL, Nair SS, Schulz DJ (2016) Synergistic plasticity of intrinsic conductance and electrical coupling restores synchrony in an intact motor network, eLife 5:e16879
- **Samarth P**, Ball JM, Unal G, Pare D, Nair SS (2016) Mechanisms of memory storage in a model perirhinal network, Brain Structure & Function, DOI 10.1007/s00429-016-1210-4.
- Feng F, **Samarth P**, Pare D, Nair SS (2016) Mechanisms underlying the formation of the amygdalar fear memory trace: a computational perspective, Neuroscience 322:370-376
- Kim D, **Samarth P**, Feng F, Pare D, Nair SS (2016) Synaptic competition in the lateral amygdala and the stimulus specificity of conditioned fear: a biophysical modeling study. Brain Structure & Function, 221:2163–2182
- Kim D; **Samarth P**, Chen Y, Nair SS (2012). Computational study of the impact of neuromodulation and dendritic morphology on synaptic plasticity. Proceedings of the Dynamic Systems and Control Conference.

Posters and Presentations

- **Samarth P**, Ball J, Ransdell J, Schulz D, Nair SS (2011) Role of conductance co-variations in preserving output of a class of cells. 41st *Society of Neuroscience (SfN) Annual Meeting*, Washington, DC, November, 12–16.
- **Samarth P**, Ransdell J, Schulz D, Nair SS (2012) Preservation of single cell and network features in a crab cardiac ganglion. 42nd *Society of Neuroscience (SfN) Annual Meeting*, New Orleans, LA, October, 13–17.
- Kim D**, Samarth P**, Chen Y, Nair SS (2012) Development of reduced order biologically realistic cell models. 42nd *Society of Neuroscience (SfN) Annual Meeting*, New Orleans, LA, October, 13–17.
- **Samarth P**, Pare D, Nair SS (2013) Computational model of a rodent central amygdala network. 43rd *Society of Neuroscience (SfN) Annual Meeting*, San Diego, LA, November, 9–13.
- **Samarth P**, Ransdell J, Schulz D, Nair SS (2013) Correlation and Synchrony: A computational model study of LC of crab. 43rd *Society of Neuroscience (SfN) Annual* Meeting, San Diego, LA, November, 9–13.
- Lane BJ, Ransdell J, **Samarth P**, Nair SS, Schulz D (2013) The effects of neuromodulation on output and synchrony in electrically coupled motor neurons with

variable intrinsic conductances in the crab cardiac ganglion. 43rd *Society of Neuroscience (SfN) Annual Meeting*, San Diego, LA, November, 9–13.

- Kim D, **Samarth P**, Nair SS (2013) Single cell models for network simulations. . 43rd *Society of Neuroscience (SfN) Annual Meeting*, San Diego, LA, November, 9–13.
- **Samarth P**, Pare D, Nair SS (2014) Computational model of a rodent central amygdala network. 44th *Society of Neuroscience (SfN) Annual Meeting*, Washington, DC, November, 15–19.
- **Samarth P**, Lane BJ, Schulz D, Nair SS (2014) Correlation and Synchrony: A computational model study of LC of crab. 44th *Society of Neuroscience (SfN) Annual Meeting*, Washington, DC, November, 15–19.
- **Samarth P**, Lane BJ, Schulz D, Nair SS (2014) Synchronization of membrane potential dynamics in cardiac ganglion network. *2014 Life Sciences Week*. University of Missouri Columbia.
- **Samarth P**, Nair SS (2014) Insights for computational network model of cardiac ganglion. *2014 Data-Blitz.* University of Missouri Columbia.

K-12 Publications

- Nair S, **Samarth P**, Nair SS (2014) Design Challenges, Curricular Unit #5 with 2 Lessons and 5 Activities, *TEACHEngineering Digital Library* (peer-reviewed resources for K-12)
- Sinha N, Chaudhary T, Nair S, **Samarth P**, Nair SS (2014) How do Sensors Work?, Curricular Unit #4 with 6 Lessons and 6 Activities, *TEACHEngineering Digital Library* (peer-reviewed resources for K-12).
- Helfer R, **Samarth P**, Nair SS (2014) What is a Computer Program?, Curricular Unit #3 with 4 Lessons and 4 Activities, *TEACHEngineering Digital Library* (peer-reviewed resources for K-12).

Work Experience

Software Engineer in Test, The MathWorks, Inc. February 2016 – May 2020

- Supported MATLAB Language Runtime Libraries Team for various projects.
- Used MATLAB Unit Testing Framework to implement testing for MATLAB Language features
- Wrote unit-tests using google mock framework in C++.
- Developed test suites using JUnit testing infrastructure.

Senior Software Engineer in Test, The MathWorks, Inc. May 2020 – Present

- Provide support for up-and-coming major MATLAB language features.
- Lead and strategize testing for cross functional impact features.

Leadership and Teaching experience

Program Manager, MU Neuro-LEGO Robotics **October 2011 – July 2015**

University of Missouri, Columbia MO

Organizing and conducting monthly LEGO camps for 3-8th grade youth emphasizing simple Math and Engineering concepts. (10-15 kids per month)

Organizing Annual LEGO robotics challenge for K-12 kids (More than 150 youth/event)

Coordinating after-school LEGO sessions at Columbia Public Schools. (30 youth per year) – This involves training the mentors (who conduct the 1.5 hrs/week session in the schools), interfacing with the teacher in schools, getting them paid, etc.

Program Coordinator, NSF Research Experiences for Undergraduate (REU) Program
May 2011 - December 2013

University of Missouri, Columbia MO

Coordinated selection of REU students from approximately 100+ applications each year from around the country; helped PI with assigning them to different research MU Lab across campus. (12 students per year).

Coordinated travel and housing for REU students.

Helped teach 1 credit computational neuroscience course for the students.

Graduate Teaching Assistant **August 2012 - December 2012**
August 2013 - December 2013

Teaching assistant for Computational Neuroscience - 7000 level undergraduate course.

Was responsible for five biological (electrophysiology) and six programming (computational modeling using NEURON) labs, for approximately 30 students per class.

VITA

Pranit Samarth was born and raised in Thane, Maharashtra, India, and graduated from Datta Meghe College of Engineering (DMCOE) Airoli, Navi Mumbai in May 2008 with a BS in Electronic Engineering. During his undergraduate studies, Pranit was also part of inter college departmental cricket team. In August of 2009, he was accepted for a Master's degree in Electrical and Computer engineering department at University of Missouri. During his first year at MU, he studied non-linear systems and computational neuroscience.

Pranit then entered a Ph.D. program under Satish Nair at University of Missouri-Columbia in the fall of 2010 to study computational neuroscience. He then completed his Master of Engineering degree in spring 2014. He has presented nine posters at the annual Society for Neuroscience Meetings. He also has three peer-reviewed K-12 publications. He also mentored three undergraduate honors research students (Morgan Spratt, Paige Loelkes, Neil Thawani) as well as undergraduate research fellows (Justin Moore, Bronson Haynes).

Pranit started working for the software company The MathWorks INC. in early 2016 in the role of software engineer and continues to work full-time at their headquarters location in Natick, MA.